OCULAR INJURY FOLLOWING PRIMARY BLAST EXPOSURE

by

Daniel François Shedd

A dissertation submitted to the faculty of
The University of Utah
in partial fulfillment of the requirements for the degree of

Doctor of Philosophy

Department of Mechanical Engineering

The University of Utah

December 2017

The University of Utah Graduate School

STATEMENT OF DISSERTATION APPROVAL

The dissertation of **Daniel François Shedd**

has been approved by the following supervisory committee members:

Brittany Coats	, Chair	**July 27, 2017** Date Approved
Kenneth L. Monson	, Member	**July 27, 2017** Date Approved
Andrew S. Merryweather	, Member	**July 27, 2017** Date Approved
Barbara M. Wirostko	, Member	**July 27, 2017** Date Approved
Bradley J. Katz	, Member	**July 27, 2017** Date Approved

and by **Timothy A. Ameel**, Chair/Dean of

the Department of **Mechanical Engineering**

and by David B. Kieda, Dean of The Graduate School.

ABSTRACT

Blast exposure is a growing cause of injury for military personnel, and is the leading cause of ocular injuries in service members. In three recent military conflicts, Operation Enduring Freedom (Afghanistan), Operation Iraqi Freedom (Iraq), and Operation New Dawn (Iraq), 13% of all casualties had visual system injury. In some cases, ocular damage does not present immediately after blast, but is diagnosed weeks or months after the exposure(s). The mechanisms and outcomes of ocular blast exposure have not been well investigated, with only a few studies performing computational, in vivo, or in vitro experiments in the field. This project aimed to fill a gap in literature by studying the closed globe injury progression from primary blast exposure. Specifically, the goal of this research was to understand long-term closed globe ocular sequelae subsequent to primary blast exposure, and to identify potential physical injury mechanisms involved in blast exposure.

To achieve this goal, a shock tube capable of reproducing ocular blast trauma in a rat was created. Computational and experimental studies characterized the shock tube to replicate an open-field Friedlander waveform. The shock tube was used to expose rats to a realistic primary blast insult with peak overpressure 228.49 $\pm$ 28.49 kPa and duration 7.06 $\pm$ 0.64 ms. Contrast sensitivity testing revealed deficits in visual function that began one day after blast and did not resolve over eight subsequent weeks. Optical coherence tomography imaging of the cornea and retina revealed corneal inflammation that presented as delayed swelling (between two to six weeks after blast) and eventual scarring. Retinal thickness changes were not detected. Intraocular pressure (IOP) was measured at high speed in a subset of the blast-exposed animals to translate external forces to intraocular load conditions, and was found to correlate strongly with the external tube pressure. A parametric finite element model of the rodent eye was developed to simulate the experimental ocular blast exposure and validated against experimentally measured IOP. The intraocular pressure was most significantly linked to the blast overpressure, globe size, and lens size. A scaling equation was developed to predict IOP as a function of these variables, and to allow equivalent comparison between the various experimental models and human blast exposure levels.

The benefits of this work are two-fold. Identification of the injuries and injury mechanisms from blast will improve the design and effectiveness of wartime ocular protective devices. The unique two-week time delay of corneal swelling suggests a possible treatment window to mitigate corneal swelling and scarring after blast exposure, and potentially improve long-term visual outcomes.

I dedicate this work to my parents, Jeff and Claudia. Thank you for always supporting me.

"But when it comes to human beings, the only type of cause that matters is final cause, the purpose. What a person had in mind. Once you understand what people really want, you can't hate them anymore. You can fear them, but you can't hate them, because you can always find the same desires in your own heart."

– Orson Scott Card

CONTENTS

LIST OF FIGURES

LIST OF TABLES

ACKNOWLEDGMENTS

I would like to acknowledge the help and advice from the members of my dissertation committee: Drs. Kenneth Monson, Andrew Merryweather, Bradley Katz, Barbara Wirostko, and my committee chair and mentor, Dr. Brittany Coats. Their feedback has been invaluable in shaping this research project. I would like to especially thank my advisor, Brittany Coats, for her advice, guidance, and support throughout my time in graduate school, and for being an excellent mentor for me as a researcher. I'm very glad we had that unscheduled meeting five (ish) years ago.

I would also like to thank my coworkers in the Laboratory of Developmental Head Injury Biomechanics. Our lab has an exceptionally fun, helpful, and collaborative environment, and I owe thanks to everyone in the group for their opinions and insight. I would be remiss if I did not specifically acknowledge Justin Jones and Nik Benko for their significant contributions to this project. I would also like to thank Stewart Yeoh from the Head Injury and Vessel Biomechanics Lab for advice and aid with animal procedures and high-speed video.

I would like to thank the veterinarians and animal technologists for their help with animal studies. Lauren Lentsch, in particular, has been a huge source of advice for animal handling techniques.

I would finally like to acknowledge the funding support for this project from the U.S. Army Medical Research and Materiel Command. I am glad that I had the opportunity to meet Robert Read, who managed the Vision Congressionally Directed Medical Research Programs. I offer my thanks to all servicemembers for their service, sacrifice, and patriotism, and hope that this research may contribute to the medical care of wounded veterans.

CHAPTER 1

BACKGROUND

Exposure to blast injury has become increasingly prevalent in military and civilian populations over the last two decades. Asymmetrical warfare in Iraq and Afghanistan has involved significant blast trauma casualties from improvised explosive devices (IEDs), mortar attacks, grenades, and aerial bombing. In the Israeli-Palestinian conflict, civilian populations were frequently subjected to mortar and rocket attacks. Even outside of war, militarized police forces (e.g., SWAT teams) experience a high volume of minor exposures during training in courses such as "Police Explosives Technicians: Forced Entry" [1]. Further, terrorist attacks across the globe, such as the Oklahoma City Bombing, Boston Marathon Bombing, and industrial accidents such as the 2013 West Fertilizer Plant explosion (Waco, Texas) expose civilians to blast in traditionally safe areas.

Before the advent of high explosive weapons, most military-related ocular trauma was caused by direct impact of high energy projectiles, such as bullets, shells, or shrapnel. The likelihood of these ocular impacts occurring is relatively low, as the surface area of the eye is small in comparison to the body [2]. In contrast, explosions expose the entire body to the blast wave, and the injured body tissue is typically at solid-gas interfaces due to rapid changes in blast pressure wave speed at these regions. The lung has been of particular interest because of its critical function and high mortality rate if damaged. For this reason, lung damage during blast exposure has been reported since the 1940s [3]–[5] and blast lung mechanics studied since the 1960s and 1970s [6]–[9]. The invention of protective clothing, coupled with advancements in medicine, have decreased blast lung injury and fatality.

The increased blast survival rates have brought several debilitating non-fatal wartime injuries to light, such as traumatic brain injury (TBI) and ocular trauma [2], [10]. These injuries are often difficult to detect because they can be outwardly invisible and worsen with time. Many research efforts are underway to understand blast TBI in hopes of developing better prevention, detection, and treatment strategies [11]–[14]. Research into ocular trauma, however, is more recent [15]–[23] and still has a long way to go before

military or clinical impact. The research presented in this dissertation focuses on the injury presentation, time course, and mechanics of primary, closed-globe ocular blast injury. This chapter will serve as a review of the history and types of ocular blast injury, discuss the limitations of the current studies investigating blast ocular trauma, and introduce the specific research aims of this project.

1.1 Blast Ocular Injury

Approximately 8-13% of all modern wartime injuries involve the ocular system [24]–[26]. While modern medical care means that many ocular injuries are not life-threatening, both the medical costs and long-term quality of life deficits are astounding. Degradation of any component of the visual pathway can lead to vision impairment or blindness. Vision loss is considered one of the most significant impairments as measured by reduced quality of life, self-rated health metrics, and financial burden [27], [28]. Hornblass et al. estimated that in the Vietnam War alone, the long-term medical expenses of vision loss in veterans neared $4 billion USD [29].

1.1.1 History of Wartime Ocular Injury

The surface of the eye comprises 0.1% of the human body [30]. Therefore, probabilities of injury are typically low. However, in wartime, there is a tendency to expose the face for better visual ability, allowing shrapnel that is innocuous to the rest of the body to cause severe visual impairment in the eye. This results in ocular injuries occurring 20-50 times more frequently than predicted [30]. In the 19th century, less than 1% of injuries were to the eye (see Figure 1.1). Since then, ocular injury rates have steadily climbed with each new war [31]. During World War I, trench and tank warfare increased ocular injury by 200-300% [32]–[35]. The advent of aerial bombing in World War II increased ocular trauma not only in military populations, but also increased incidence in civilians [36].

1.1.2 Types of Wartime Eye Injuries

Injuries to the eye can generally be classified into open globe injury or closed globe injury. Open globe injury is an open wound of the eyeball. [43]. Combat-related open globe injuries commonly involve shrapnel or other blast debris piercing ocular tissue, referred to as intraocular foreign bodies (IOFBs). Thach et al. reported 797 cases of severe ocular injury in the Iraq War from 2003-2005 [42]. Open globe injuries comprised 55% of the total reported cases (Table 1.1). Foreign bodies were present in nearly 75% of all severe injuries, with the majority presenting inside the eye or in the orbit. Eyelid injuries occurred in over

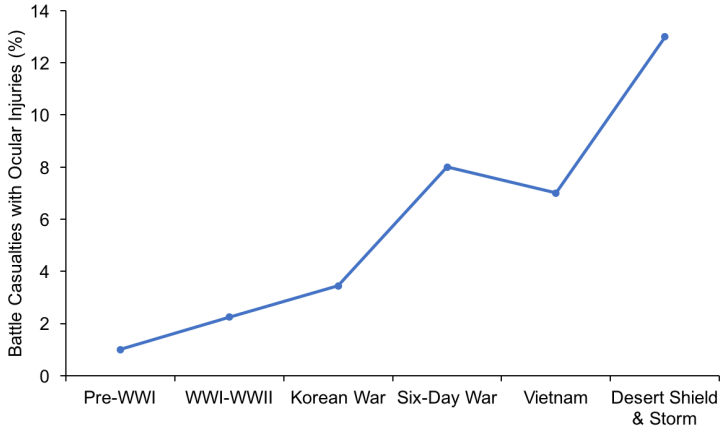

Figure 1.1: Ocular injury rates increasing over time. Created from summary by Wong et al. [31]. Original data from [25], [29], [30], [32]–[35], [37]–[41].

Table 1.1: Presentation of open globe injuries from 797 reported ocular trauma cases in the Iraq war. Recreated from [42].

	n	(%)
Open globe injury	**438**	**55.0**
Mean laceration size	11.2 mm	
Foreign body	**328**	**74.9**
Intraocular	116	26.5
Orbit	95	21.7
Corneal/conjunctival	86	19.6
Eyelid	31	7.1
Eyelid injury	**265**	**60.5**
Lid laceration	197	45.0
Eyelid foreign body	31	7.1
Tissue loss	12	2.7
Avulsion	11	2.5
Canalicular	9	2.1
Burn	5	1.1
Optic nerve injury	**267**	**6.2**
Avulsion	14	3.2
Optic neuropathy	13	3.0
Orbital injury	**195**	**44.5**
Fracture	100	22.8
Foreign body	95	21.7

60% of all reported cases. The vast majority of the victims (723/797) were not wearing eye protection at the time of injury, which likely explains the increased foreign body injury rates [44].

Closed globe injuries describe any injury to the eye or orbit that does not involve penetration. Examples of closed globe injuries include retinal hemorrhage, retinal detachment, vitreous detachment, hyphema, corneal edema, and optic nerve avulsion [20], [45]. A study of 46 veterans with blast exposure found that 43% experienced closed globe injuries [2]. Many of the closed globe injuries were not detected immediately, but presented at later timepoints after initial insult. In a study by Weichel et al. that included a broad range of severities, closed globe injury was the dominant type of ocular injury (54%) in soldiers [24]. These closed globe injuries were equally split between the anterior and posterior segments of the eye and are summarized in Tables 1.2.

1.1.3 Blast as an Ocular Injury Mechanism

The majority of eye injuries in modern military conflicts result from blast exposure. A study of 207 eye injuries in a combat support hospital found that 82% were caused by blast exposure [46]. This incidence is further supported by findings from Thach et al. and Weichel et al. studies which report 72-79% of ocular injuries were due to blast [24], [42]. Other military mechanisms of ocular trauma are summarized in Table 1.3. Many eye injuries caused by blast exposure present concurrently with other injuries, especially TBI. In several studies, approximately 75% of soldiers diagnosed with TBI display symptoms of visual impairment [47]–[49]. Because of the high co-occurrence, the U.S. Armed Forces requires a

Table 1.2: Presentation of closed globe injuries from 387 reported ocular trauma cases in Operations Iraqi and Enduring Freedom. Recreated from [24].

	n	(%)
Closed globe injury	**328**	**54.2**
Anterior	**103**	**23.8**
Conjunctival	59	13.6
Cornea abrasion	24	5.6
Hyphema	95	22.0
Lens dislocation	29	6.7
Cataract	123	28.5
Posterior	**131**	**30.3**
Vitreous hemorrhage	205	47.5
Retinal detachment	18	4.2
Macular hole	101	23.4
Retinal vascular injury	10	2.3

Table 1.3: Distribution of ocular injury mechanisms from 469 reported cases in the Iraq War. Recreated from [42].

Causes of eye injury	**n**	**(%)**
Explosion	344	73.3
Gunshot	51	10.9
Vehicle accident	25	5.3
Blunt trauma	17	3.6
Burn	8	1.7
Other	24	5.1

mandatory ocular examination in all TBI cases. This mandatory examination has brought to light many cases of closed globe injury that were not detected immediately, but diagnosed at much later time points after the initial insult [2].

Wartime explosion is a complex phenomenon involving many potentially injurious factors. For this reason, blast injuries are divided into four classifications known as primary, secondary, tertiary, and quaternary blast injury. Each classification describes specific injury mechanisms relating to high-speed pressure waves, shrapnel, blast wind, and heat, respectively.

1.1.3.1 Primary Blast Injury

Primary blast injury is caused by the supersonic expanding pressure wave resulting from the detonation of high explosives. The pressure wave features a pressure discontinuity at the shock front as the ambient pressure instantly increases to a peak overpressure. The shock wave can propagate through physical barriers including buildings and body organs. The speed of the shock wave through a structure is related to the density of the structure. Wave propagation speed changes rapidly at material (or tissue) interfaces, such as gas-filled cavities. The lungs are the most vulnerable to fatal blast injury, with tissue tending to rupture or collapse [50]. In the eye, the major vulnerable interfaces are between the environment and the cornea, cornea and aqueous humor, and vitreous humor and retina (see Figure 1.2). Blast may also cause successive compression and expansion of the eye due to rapid changes in intraocular pressure (IOP). Extreme rapid changes in IOP can damage many structures in the eye, particularly around the optic nerve head [51].

1.1.3.2 Secondary Blast Injury

Secondary blast injuries result from flying shrapnel and debris, and cause a large portion of blast-related injuries and fatalities. Many IEDs, in particular, are designed

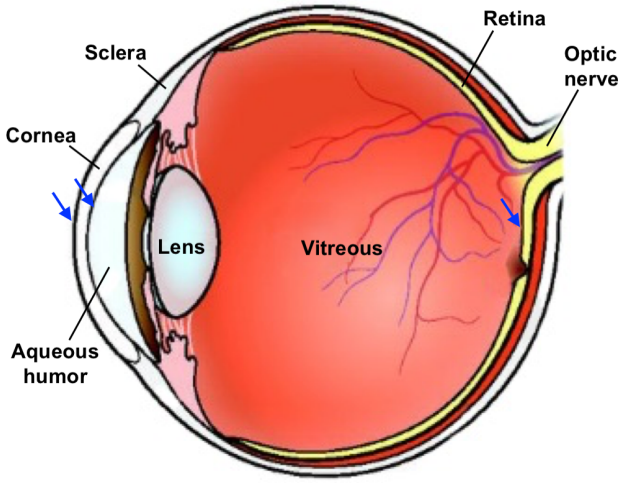

Figure 1.2: Schematic diagram of human ocular anatomy. Arrows indicate areas of high vulnerability. Adapted from Veleri et al. [52].

to maximize secondary injuries by including shrapnel inside or around the bomb itself. Secondary injuries to the eye can include orbital fracture or intraocular foreign bodies, and many result in complete loss of the eye. These injuries can be mitigated fairly effectively by the use of protective eyewear to deflect high-speed projectiles. Ocular injury occurred in 17% of soldiers wearing ocular protection compared to 26% of soldiers not using ocular protection [44]. In the ocular injuries that did occur, eye armor decreased the severity.

1.1.3.3 Tertiary Blast Injury

Tertiary blast injuries result from the blast wind throwing the victim, causing inertial or blunt trauma injuries. TBI can result from rapid head rotation or head impact, and roughly 68% of military personnel exposed to a blast have TBI [53]. As stated earlier, nearly 75% of blast-induced TBI patients present with concurrent visual dysfunction [47]–[49], but closed globe eye injuries, such as retinal and vitreous hemorrhages or detachments, are not related to the TBI and can result directly from tertiary mechanisms.

1.1.3.4 Quaternary Blast Injury

Quaternary injuries include any injury not listed in the previous three categories. Common sources of quaternary injuries include thermal injuries, smoke inhalation, and psychological disorders. Burns to the cornea or orbit are the most frequent quaternary injuries affecting the eye.

1.1.3.5 Ocular Injury Severity

The severity of blast ocular injury is related to the explosion magnitude and distance between the source of the explosion and the affected individual. The shock front expands spherically from the source (see Figure 1.3), reducing in strength as it travels. Incident waves behind the shock front move through compressed and denser air and therefore travel faster than the shock front. Incident and reflected waves from the ground surface recombine with the shock front to create a mach stem with increased pressure and destructive potential. Recent computer models have demonstrated that the shape of the facial structures, in particular the nose and brow, act to focus the blast into the eye and orbit, and therefore increase the effective blast pressure applied to the eye [16]. These computer models are discussed further in Chapter 4. Compounding the focusing effect of facial structures is the reflection of the blast wave off of the bony orbit, resulting in waves bouncing through the eye multiple times. Similarly, some eye armor designed to protect from secondary (shrapnel) injuries traps the blast pressure wave in front of the eye and increases injury severity [17].

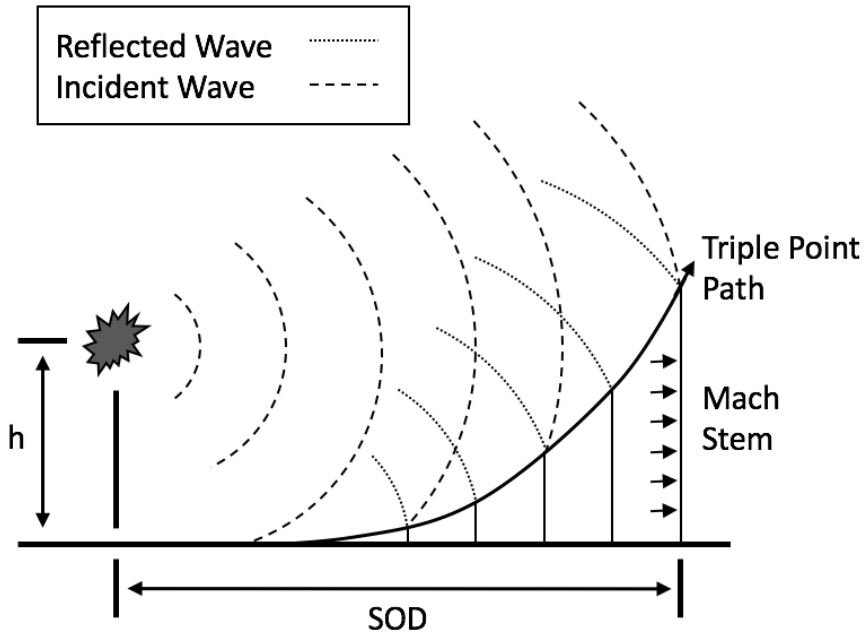

Figure 1.3: Propagation of shock wave from above ground explosion. Exposure levels depend on explosive magnitude, height (H), and standoff distance (SOD). Image adapted from [54].

1.2 Research Overview

This research focuses on the injury presentation, timecourse, and mechanics of primary, closed globe ocular blast injury. The mechanisms and outcomes of closed globe injury due to blast have not been well investigated, with only a few studies performing computational [16]–[18],[21], in vivo [20],[55],[56], or in vitro [15] experiments on the subject. These studies have focused primarily on immediate (24 h) or short-term (<4 weeks) ocular injury. However, it is known that some closed globe injuries do not present immediately after blast, and many are not diagnosed until months or even years after the exposure(s) [2]. Little is known about the progression of closed globe injury, and whether there are early identifiers for impending vision loss. The goal of this dissertation was to fill a gap in the literature by studying long-term closed globe injury sequelae subsequent to primary blast exposure, and evaluate the effect of anatomical features on ocular injury.

To achieve this goal, a shock tube capable of reproducing ocular blast trauma in a rat was utilized in Chapter 2. Computational and experimental studies were used to design and characterize the shock tube such that it best replicated an open field blast. The shock tube was then used in Chapter 3 to expose rats to a realistic blast insult. Intraocular pressure was measured at high-speed in a subset of the blast-exposed animals to translate external forces to intraocular load conditions. The visual system of the rat was evaluated with behavioral estimates of visual acuity, optical coherence tomography imaging of the cornea and retina, vitreous biomarkers, and histology at time points up to eight weeks after blast. In Chapter 4, a finite element model of the rodent eye was developed to simulate experimental studies from Chapter 3. The effect of ocular anatomical differences between rats and humans on pressure, stress and strain distribution were evaluated in the model.

The benefits of this work are two-fold. First, the identification of the injuries and injury mechanisms from blast will improve the design and effectiveness of wartime ocular protective devices. Second, a better understanding of the time-dependent response of the eye to blast exposure may elucidate diagnosis and treatment strategies for closed globe trauma, and improve overall visual outcomes for military service members.

CHAPTER 2

REPLICATING OPEN FIELD PRIMARY BLAST IN A LABORATORY

2.1 Introduction

When an explosive is detonated in an open area, the resulting blast is called an open field blast. The detonation of the explosive source generates a positive pressure wave that travels spherically outwards from the blast source at the speed of sound. This wave, called the incident wave, decays proportional to the cubed-distance, d^3, from the blast source. As the wave travels, the peak pressure will continue to decrease at this rate while the positive phase duration increases.

Open field blast pressure waves take the form of the Friedlander waveform. This waveform is characterized by a rapid rise to a peak overpressure in the positive phase, followed by a negative phase (see Figure 2.1). The variables to define the Friedlander pressure waveform in terms of time are the instantaneous pressure, P, the peak overpressure, P^+, and the duration of the positive phase, t_+ (Equation 2.1).

$$P = P^+ \frac{-t}{e^{t^+}}(1 - \frac{t}{t^+}) \tag{2.1}$$

A scaled distance, d', is calculated from the distance, d, and the TNT-equivalent explosive magnitude in kilograms, W (Eq. 2.2). This scaled distance represents the total strength of the explosion, combining the effects of explosive magnitude and the mitigating effects of distance. Blast parameters at a given scaled distance can be estimated by first calculating the peak overpressure (Eq. 2.3) and impulse (Eq. 2.4), and then calculating the positive phase duration (Eq. 2.5) [58]–[60].

$$d' = d/W^{1/3} \tag{2.2}$$

$$P^+ = \begin{cases} 1.13 * 10^6 d'^{-2.01}, & \text{if } 1 \leq d' < 10 \\ 1.83 * 10^5 d'^{-1.16}, & \text{if } 10 \leq d' < 200 \end{cases} \tag{2.3}$$

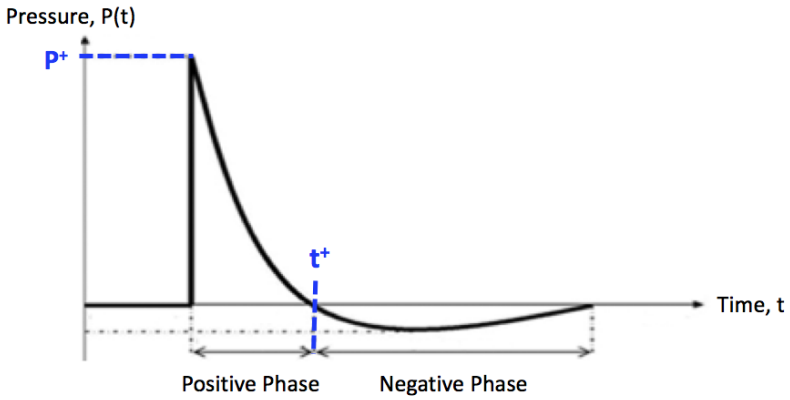

Figure 2.1: Diagram of the theoretical Friedlander waveform describing open field blast. Key parameters of the wave are peak overpressure (P^+), positive phase duration (t^+), and the impulse. Impulse is calculated by integrating under the each phase of the pressure-time curve. Image recreated from [57].

$$i^+ = \begin{cases} 203{d'}^{-.091}, & \text{if } 1 \leq d' < 10 \\ 335{d'}^{-1.06}, & \text{if } 10 \leq d' < 200 \end{cases} \tag{2.4}$$

$$t^+ = 2.717\frac{i^+}{P^+} \tag{2.5}$$

For explosives ignited off the ground, commonly known as air burst weaponry, the shock phenomenon becomes slightly more complex. Some portion of the incident wave reflects from the ground surface. This reflected wave initially travels behind the incident wave where the air is denser and has a higher temperature than the ambient air in front of the incident wave. This results in the reflected wave traveling at a higher speed than the incident wave and catching up to the incident wave. Both waves coalesce to form a stronger wave, called a Mach stem (see Figure 2.2). The Mach stem has higher overpressure and greater total energy than the original incident wave.

2.1.1 Methods for Recreating Open Field Blast in a Laboratory

2.1.1.1 Shock Tubes

The most common method to recreate open field blast waves in a laboratory setting is with a shock tube. Shock tubes generate Friedlander primary blast waveforms in a controlled and consistent manner. They are designed with an initially pressurized driver section and an initially unpressurized driven section. The two tube sections are separated by a thin membrane commonly made from thin sheets of biaxially-oriented polyethylene (BoPET, trade name Mylar), aluminum, or steel. The rupture of the membrane triggers

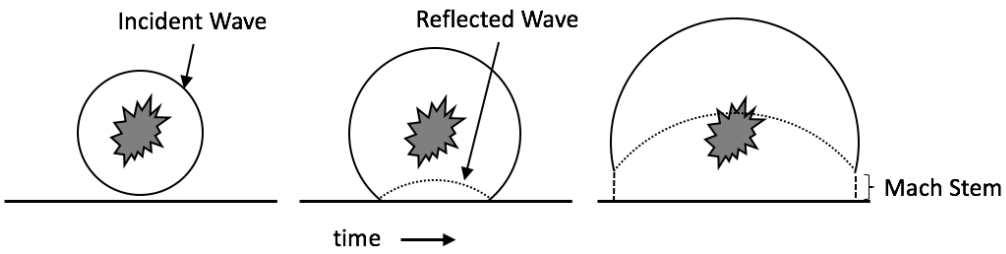

Figure 2.2: Propagation of shock wave from air burst explosive. Reflected wave coalesces with the incident wave to create a Mach stem that is more energetic and destructive than the initial wavefront.

the initiation of the blast wave. This is achieved either by physical detonation of an explosive (blast driven shock tubes) or by overpressurization of the driver section (compressed gas shock tubes). An arrowhead may also be used to puncture the membrane at lower compressed gas pressures.

When the membrane ruptures, a high pressure incident wave travels down the tube into the driven section. The density of air behind these waves is increased, which causes the speed of sound behind them to increase. Because the incident wave is moving slower relative to subsequent pressure waves, the trailing waves catch the initial wave to create a shock front. It should be noted that the membrane rupture also triggers an expansion wave that propagates back into the driver section. This wave travels through gases with the highest density and therefore becomes the fastest wave in the system. This wave reflects off of the back surface of the driver section, and follows the shock front through the driven section [61]. When it catches up and coalesces with the shock front a Friedlander wave is formed (see Figure 2.3).

2.1.1.2 Rifle

A few groups have used a rifle loaded with a primed cartridge case without projectile as a small shock tube [14], [64]. This design works under the same operating principles as a compressed gas driven shock tube by replacing the driver section with the explosive cartridge. The primary advantage of such a setup is the reduced cost of development of the device. The major tradeoffs are that the rifle will be limited to a very short positive phase duration (5 μs - 1 ms), and the small barrel of the device requires the test location to be outside the barrel. Placing the test subject outside of the barrel avoids the high-speed gas jet to isolate primary injury. However, the accuracy of the test location is critical due to the relation of distance from the muzzle to overpressure.

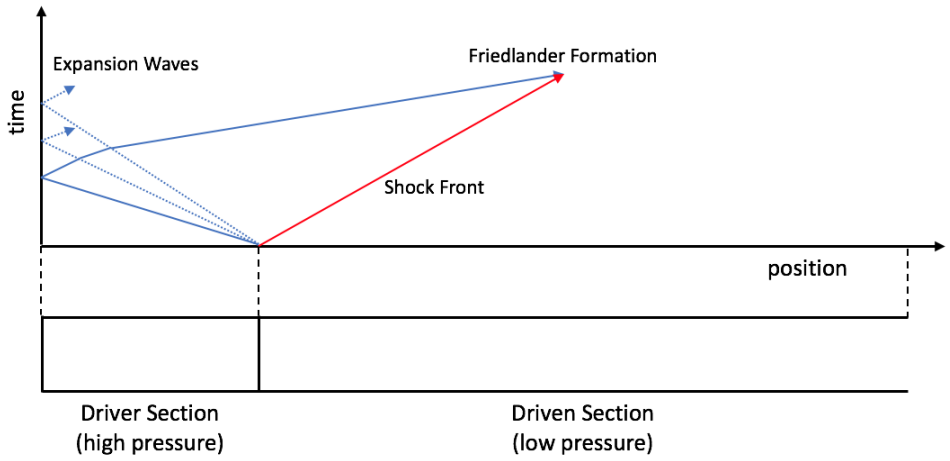

Figure 2.3: Formation of Friedlander shock wave after rupture of a burst membrane in a shock tube. Created based on [62], [63].

2.1.1.3 Air Gun

Some groups have reproduced blast injury using a modified paintball gun [11], [19], [20], [65]. Studies using a paintball gun as a surrogate for a shock tube have the advantage of being inexpensive and quick to develop, but it is likely that the injury produced is much more linked to the blast jet directed into the eye than a true pressure wave injury. Additionally, the pressure measurements reported in this methodology are not directly comparable to other blast studies due to the orientation of the pressure transducers. Pressure measurements must be recorded from a side-on pressure gauge to isolate the hydrostatic shock pressure [60]. Placement of the pressure gauge in the front-on orientation instead records the total pressure (stagnation pressure), which includes both initial pressure wave, reflected wave from the sensor, and the blast wind. Reporting the stagnation pressure results in overestimating the strength of the exposure when comparing to other sources in literature. In fact, pressure profiles from the paintball gun studies show that no shock front or Friedlander wave was applied to the animal subjects. Instead, the entire exhaust jet is directed into the eye and extraocular space [20].

2.1.1.4 Air Tank

Another method of reproducing pressure injuries in the lab is the use of large diameter air tanks [66]. The driver and driven section components of an air tank are similar to shock tube, with the main differentiator being the much larger width to length ratio of an air tank. The geometry of the air tank means that the pressure wave applied to

the experimental location is not as similar to the Friedlander waveform, and the positive phase duration is longer, 10-15 ms in the case of Mohan et al. [66]. Additionally, pressure waves generated by these systems often feature significant reflections due to the confined tank geometry.

2.1.1.5 Explosives

Another method of reproducing blast is the use of real explosives [13], [67]. These methods are most similar to real-world blast loading and are appropriate for investigating the combined mechanism of blast loading. However, the blasts used in most laboratory settings are small in magnitude compared to real-life, so the distance between the source and test location must be very small to ensure adequate peak overpressure to replicate real-world injury. As a result, these studies tend to have very short positive phase durations. In addition, the expense and regulatory challenges of acquiring approval and materials for explosive testing is higher than the use of shock tubes.

In the present research, a compressed gas driven shock tube was used to replicate the Friedlander waveform and simulate traumatic blast exposure. This chapter describes the design, characterization, and modification of the shock tube to accurately replicate the theoretical pressure profile with consistent pressure wave response. Peak overpressures of 180 - 240 kPa were targeted based on prior blast studies with low fatality rates [20].

2.2 Methods

2.2.1 Shock Tube Description and Modifications

The shock tube used in this research (see Figure 2.4) was purchased used from Agile Nano (San Diego, CA). The tube has a 64-cm driver section, 457-cm driven section, and constant internal diameter of 15 cm. The tube features electronic pressure control using a solenoid valve as well as pneumatically activated breech closure and membrane rupture. Firing can be aborted using the bleed valve located on the side of the driver section, allowing the driver section to be safely depressurized without firing the shock tube. The existing tube components had max pressures allowances of 1240 kPa. This limited the maximum driver pressure and maximum shock wave overpressure to 1240 and 250 kPa, respectively. Tubing, valves, and regulators on the control panel were replaced with components rated to maximum pressures of 2000 kPa. This raised the potential maximum shock wave overpressure to an estimated 345 kPa. Two additional modifications to the shock tube were a silencer/catch tank and improved membrane clamp. These modifications are described in further detail below.

Figure 2.4: Shock tube in place at Agile Nano facility. Assembled identically when set up in the University of Utah's Experimental Studies Building.

2.2.1.1 Pressure Wave Silencer and Catch Tank

A silencer and catch tank were added to the shock tube to reduce noise levels without inducing large reflective waves. Noise reduction can be achieved by slowing the expansion of the pressurized gases at the end of the driven section [23], [68]. The silencer and catch tank were designed to create a two stage expansion (see Figure 2.5). Specifically, the 15-cm diameter of the shock tube was expanded to 25 cm (silencer, see Figure 2.6A), and then to 51 cm (catch tank, see Figure 2.6B). Inner surfaces of the silencer and catch tank were lined with acoustic absorbent foam and rubber to absorb some of the shock energy. Additional shock wave energy was dissipated by allowing the catch tank to move backwards. This transferred some energy of the shock wave into kinetic energy of the tank.

The silencer and catch tank reduced the sound level generated by the shock tube by approximately 10 dB. The catch tank added a reflected wave that traveled from the back of the tank toward the driver section. The reflected wave had a peak overpressure of 15 kPa, which was <10% of the peak overpressure of the shock front. The arrival time of the wave was 33 ms after the shock front and was introduced into the signal after the negative phase of the blast had already passed by (see Figure 2.7).

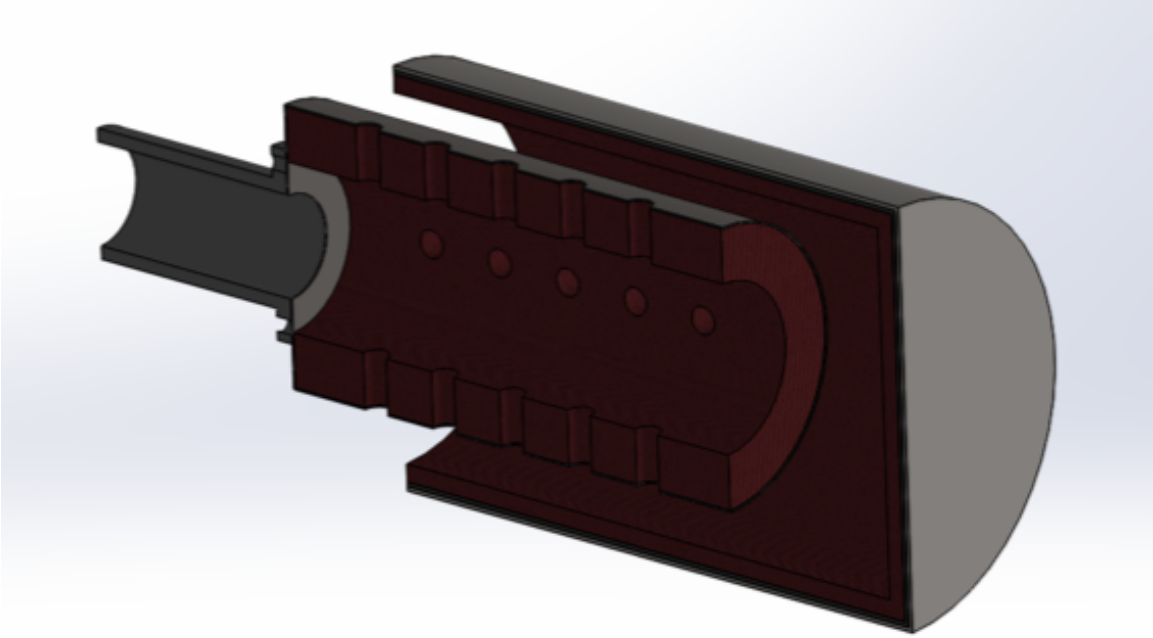

Figure 2.5: Silencer and catch tank increased the effective area of shock from 176.7 to 490.9 cm^2 (277%) in the first stage, and expanded the effective area from 490.9 to 2042.8 cm^2 (416%) in the second stage. Material indicated in red was absorbent acoustic foam to further dampen the acoustics of the blast.

(A) (B)

Figure 2.6: Full silencer apparatus assembled and installed at end of shock tube driven section. (A) Inner silencer lined with acoustic foam (3.8 cm). (B) Outer catch tank strapped to heavy duty cart allowing recoil motion. 55-gallon steel drum lined with rubber-backed acoustic foam (5.1 cm).

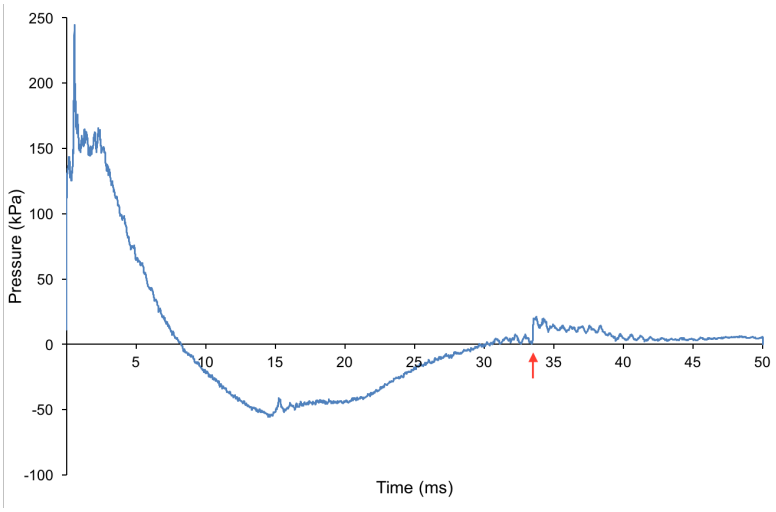

Figure 2.7: Pressure profile recorded at location of animal holder. Reflected wave (arrow) arrived at approximately 34 ms, after the negative phase of the shock wave had passed the experiment location.

2.2.1.2 Membrane Clamp

Early shock tube characterization identified compressed air leaking between the driver and driven section. The seal between driver and driven section consisted of two steel plates with rubber gaskets, compressing a Mylar membrane. This arrangement resulted in buckling and radial crimping of the membrane, which created a small passage for the pressurized air to escape (see Figures 2.8A and 2.8B). To fix the issue, a new clamping design (see Figure 2.8C) was created based on the prior work of Holmberg [62]. In this design, four grooves were created in both clamp faces, but rubber gaskets were only placed in every other groove, such that the membrane would be forced to crimp in a circumferential direction (Figure 2.8D). The forced crimping in the circumferential direction impeded the formation of buckles in the radial direction. The new clamp design prevented air leakage, but doubled the preparatory time required between shock tube uses.

2.2.2 Shock Tube Finite Element Analysis

In preparation for the experimental studies described in Chapter 3, a parametric finite element analysis was performed in ABAQUS ((Dassault Systemes, Vélizy-Villacoublay, France) to (1) confirm the formation of a shock wave within the shock tube, (2) select the gas for the driver chamber, and (3) identify the ideal placement of the animals. A coupled Eulerian-Lagrangian (CEL) approach was used to represent the physics of the shock tube (Lagrangian) and gas (Eulerian) in the same simulation.

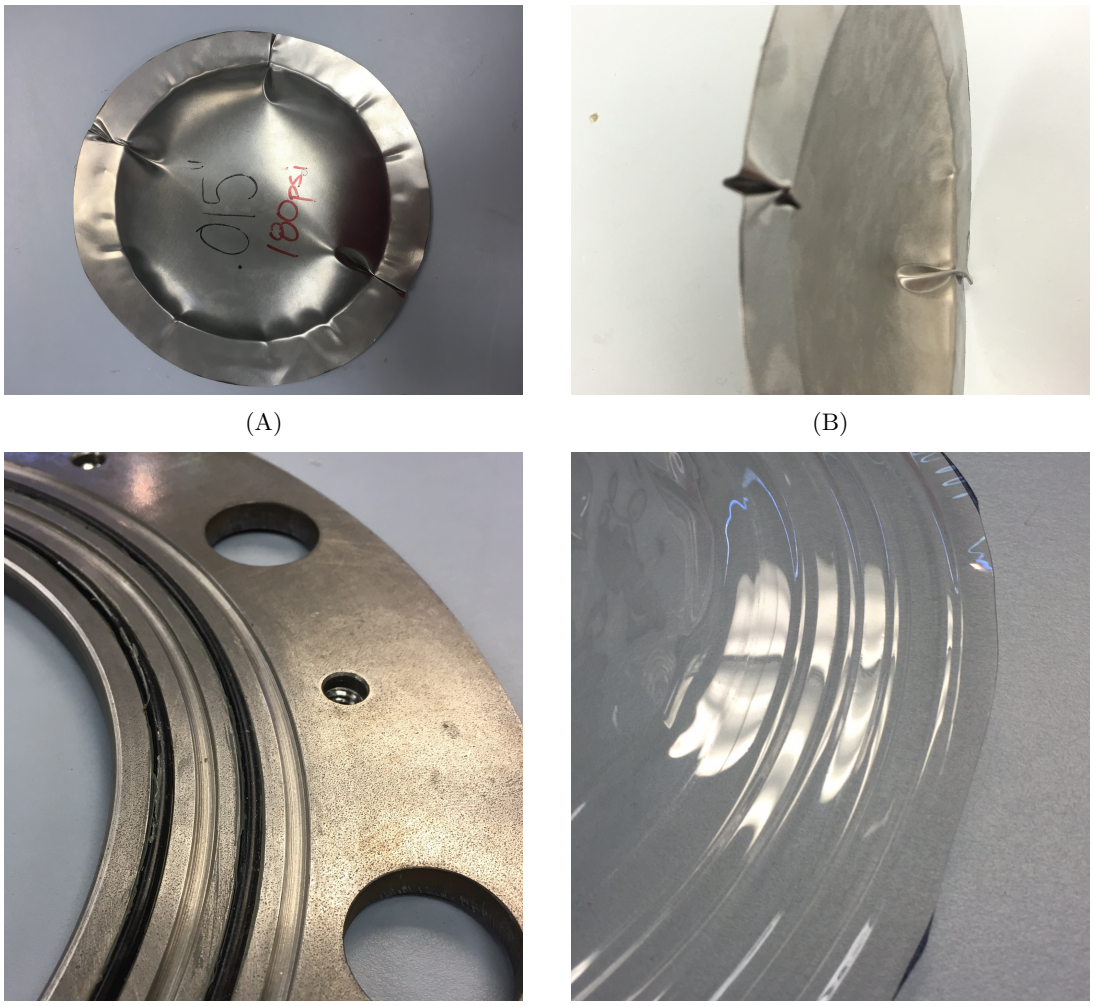

(A) (B)

(C) (D)

Figure 2.8: A new clamp design successfully eliminated leakage from driver section. (A) Radial crimp pattern before clamping upgrades, shown on .015" thick aluminum membrane. (B) Close up of radial crimp showing passage allowing air flow, with symmetrical crimp on opposite face of membrane. (C) Close up of interlocking groove and rubber gasket system. (D) Circumferentially crimped membrane due to interlocked groove and gasket system.

2.2.2.1 Geometry

The model geometry consisted of two hollow pipes to represent the driver and driven sections of the tube, and a rectangular Eulerian space that surrounded the tube. The driver and driven section geometries were created as cylindrical shells with diameters of 0.01524 m (6 in) and lengths of 1 and 3 m, respectively, as shown in Figure 2.9. These dimensions were based on the geometry of the physical shock tube. One end of the driver section was closed. The connection between driver and driven sections, and the end of the driven section, were left open. The membrane that initially separates the driver and driven sections of the tube was not included in the model because the simulation began immediately after membrane rupture (t=0 sec). The assumption implied for this simplification is that the membrane ruptured uniformly and completely, and did not impede gas flow. This simplification has been verified and reported by Carlucci et al. [69].

2.2.2.2 Boundary Conditions

The rigid pipe was fixed at the closed end of the tube to prevent any motion of the pipe. The driven section was set to room temperature (300 K) at ambient pressure and the driver section was set to a gage pressure of 256.1 kPa using an initial temperature of 1032 K. These boundary conditions created an immediate pressure front, which simulated membrane rupture at time zero. Simulations ran until the shock front approached the end of the tube. For simplicity, the environment outside the tube was not modeled. The effect of gravity was negligible to the shock wave evolution and was not included in the simulation.

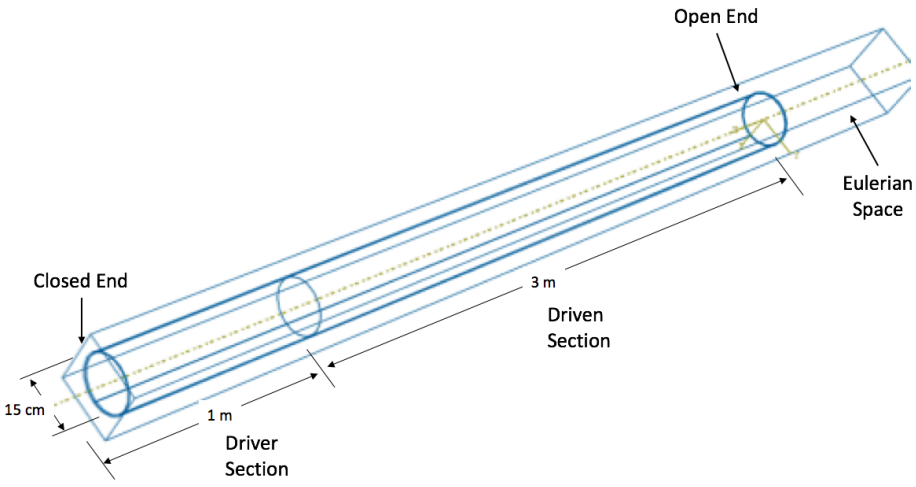

Figure 2.9: Coupled Eulerian Lagrangian shock tube geometry showing both rigid pipe and Eulerian space.

2.2.2.3 Material Models

Volume fractions for the initial gas in the shock tube were defined by the inner wall of the shock tube. Air was used to represent the gas in the driven section for all simulations. The gas in the driver section was varied between helium, hydrogen, and air to assess the effects of driver gas selection on peak overpressure, positive phase duration, and Friedlander wave evolution. All gases were modeled using the ideal gas equation of state (EOS) model. The ideal gas model, $P = pRT$, assumes inviscid compressible flow. This assumption is valid for blast modeling far away from the blast source, and was validated by Carlucci for shock tube simulations [69]. The parameters used to define each material are listed in Table 2.1. The pipes were modeled as rigid bodies because deformation of the pipe was negligible and irrelevant to the desired output of the simulation.

2.2.2.4 Mesh

Pipes were modeled with quadratic quadrilateral shell elements, with the exception of the closed end of the driver section which contained a hybrid mesh of quadratic quadrilateral and triangular shell elements. The pipe mesh was kept coarse to ensure the element size was large in comparison to the Eulerian mesh and avoid errors in pipe-gas contact (see Figure 2.10A). The Eulerian space was meshed using linear hexahedral elements with reduced integration and hourglass control (see Figure 2.10B). To assess convergence, mesh density was varied according to Table 2.2 and peak overpressure was extracted at 2.5 and 5 ms postrupture which correlated to geometrical locations 1/3 and 2/3 down the driven section, respectively. The convergence study used constant driver pressure so that the wave speed was the same for all mesh densities. All convergence analyses were performed along the central axis of the pipe to avoid boundary effects and used integration point values, where the maximum element value was taken to be the peak overpressure of the shock wave at that location. Results at 2.5 ms were verified using a shock tube solver developed by Ritzel [71]. The analytical solver uses gas properties and initial pressure and temperature conditions to calculate the overpressure of a shock wave at any given distance. The parameters used in this simulation resulted in an analytical overpressure of 167.9 kPa.

2.2.3 Shock Tube Membrane Characterization

Experimental studies were performed to verify the development of the Friedlander waveform and characterize changes in peak overpressure with membrane thickness. To visualize the development of the pressure waveform, the shock tube was instrumented with flush mounted piezoelectric PCB 113B26 (PCB Piezotronics, NY) pressure sensors at 61 cm

Table 2.1: Summary of gas material properties used in shock tube model [69], [70].

Gas	Density (kg/m^3)	Dynamic Viscosity (kg/m-s)	Ambient Pressure (Pa)	Gas Constant (J/kg-K)	Specific Heat (J/kg-K)
Air	1.177	1.85E-05	101325	287	716
Helium	0.1667	1.96E-5	101325	2077	3120
Hydrogen	0.0899	8.75E-6	101325	4126	10185

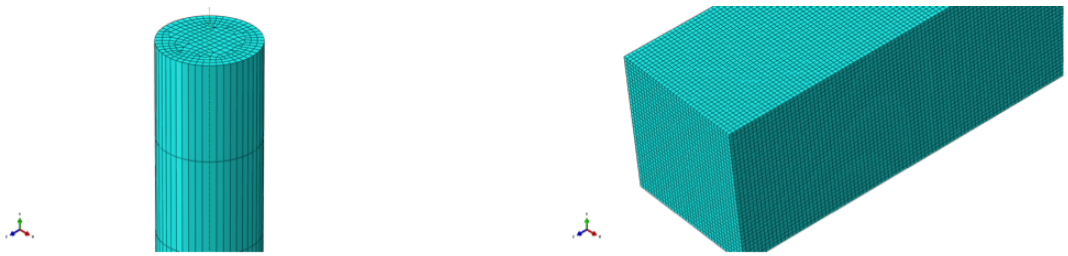

(A) (B)

Figure 2.10: Meshed part components for CEL Model. Lagrangian (A) and Eulerian (B) part meshes shown.

Table 2.2: Element sizes and quantities for the mesh convergence study.

Model Component	Coarsest	Coarser	Coarse	Fine	Finer	Finest
Rigid Pipe Elements	1548	1548	1548	1548	1548	1548
Eulerian Space Elements	2500	20000	42250	312500	600625	925344
Eulerian Edge Length (cm)	5	2.5	2	1	0.8	0.7

increments along the length of the driver section. The flush mount configuration ensured that the incident pressure was measured (rather than the reflected pressure, which would be measured by a sensor orientated face on to the blast). The sensor configuration in the side wall of the shock tube can be seen in Figure 2.11. The pressure sensors are capable of measuring pressures up to 3447 kPa at frequencies between .01 Hz and 1 MHz.

To characterize BoPET Mylar rupture in the shock tube, sheets of varying thickness (0.127, 0.178, and 0.254 mm) were cut into circular membranes and evaluated in the shock tube at driver pressure starting at 103 kPa (15 psi) and increasing in 69 kPa increments (10 psi) up to the natural rupture of the membrane. Preliminary evaluation of other membranes, such as .1 to .5 mm aluminum, were found to be challenging to rupture consistently, and were not investigated further. Peak overpressure was measured 4.45 m from the membrane and the efficiency with each thickness was calculated as the ratio between the driver pressure, p_{driver}, and the driven pressure, p_{driven} (Eq. 2.6).

$$Efficiency = p_{driven}/p_{driver} \tag{2.6}$$

2.2.4 High-Speed Video

The driven section of the shock tube was initially constructed from Schedule 80 gray 6 PVC pipe. The experimental segment of the tube was replaced with clear PVC pipe to allow visualization of animal studies using high-speed videography. Sensor ports were installed in the wall of the clear replacement pipe to allow the pressure measurements

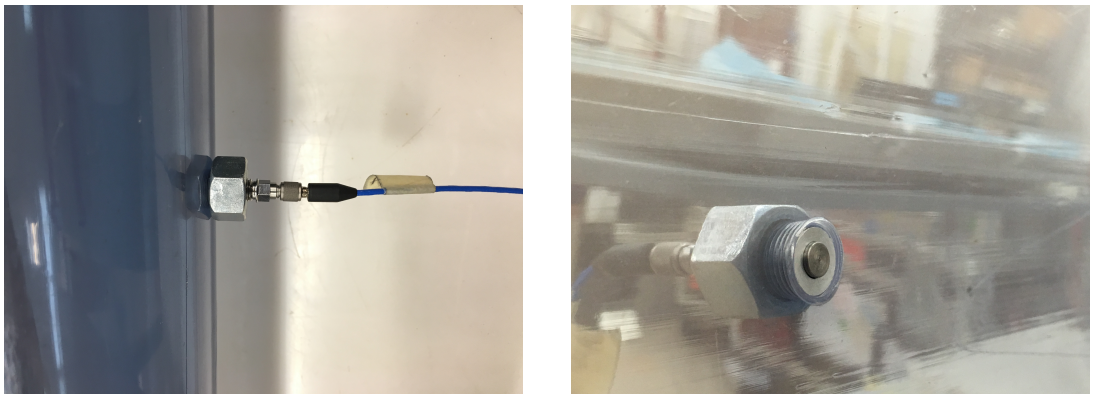

(A) (B)

Figure 2.11: Piezoelectric sensors installed in the shock tube. (A) Sensor fixture entering external surface of shock tube. (B) Flush mount configuration viewed from the inside of the tube. This configuration measured the side-on overpressure of the shock wave, without inclusion of the stagnation pressure of the blast wind.

to be recorded. The new pipe segment was affixed to the rest of the driven section using liquid gasket material to create an airtight seal and 8 bolts to solidly link the sections. A high-speed video camera (Phantom Miro eX4; Vision Research, Wayne, New Jersey) was then used to visualize head motion in response to the blast exposure. Halogen lamps provided additional lighting required for the high-speed video. This set up was sufficiently bright to record the blast at 15,000 frames per second. High-speed video was performed in sham blasts using surrogate clay rat models to visualize the shock wave formation and assess presence of debris within the tube.

2.2.5 Data Acquisition and Processing

Raw output from the pressure transducers was passed through a signal conditioner (PCB 482C Series Sensor Signal Conditioner) and 180 kHz analog anti-aliasing filter. Filtered data were acquired at 1 MS/s using a NI 9223 Analog Input Module (National Instruments, Austin, TX). Data recording was triggered by a 34.5 kPa threshold. Upon triggering, the previous 5 ms and subsequent 50 ms were saved to an output file. Additional post hoc low and high pass filtering using a fourth order Butterworth filter at cutoff frequencies of 50 kHz and 5 Hz, respectively, were performed in MATLAB (MathWorks, Natick, MA). This post hoc filter was performed to reduce noise and ringing of the sensor without cutting out significant portions of the peak overpressure (see Figure 2.12). The cutoff frequencies were determined from spectral analysis of the blast data. Low-frequency bias was removed by subtracting the mean of preblast data. Peak overpressure, peak negative overpressure, positive and negative phase durations, and positive, negative, and net impulse were extracted and stored for analysis.

2.3 Results

2.3.1 Finite Element Analysis

2.3.1.1 Convergence and Verification

Both of the sampled time points (2.5 and 5 ms) showed convergence towards a peak overpressure (Figure 2.13). The 2.5 ms time point converged to 169 kPa, which was 1.2% error from the analytical solution. Based on results from the convergence study and verification of the model against the analytical solution, a 312,500 element Eulerian mesh density was selected for all subsequent simulations. At this mesh density, the pressure at 5 ms had fully converged and the pressure at 2.5 ms was within 4% of the analytical solution.

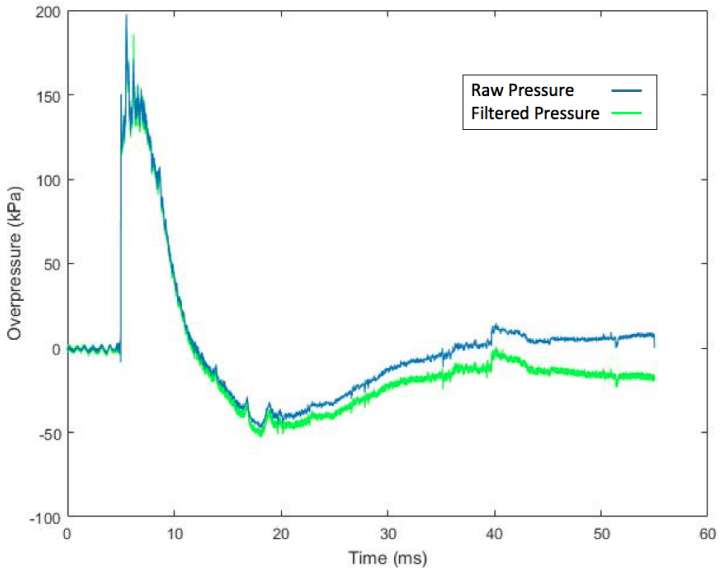

Figure 2.12: Typical blast profile with final filters applied to smooth the raw data.

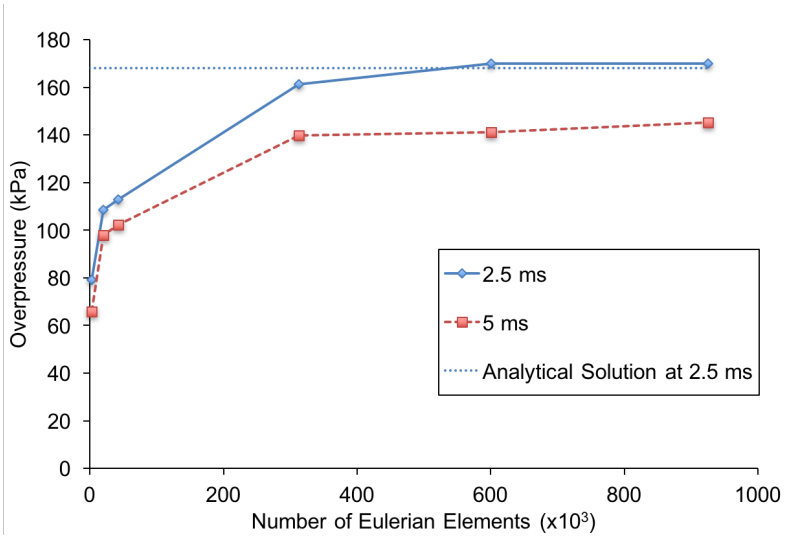

Figure 2.13: Convergence of predicted wave overpressure extracted at two timepoints after simulated membrane rupture. Both timepoints converged similarly. Predictions were only 1.2% off of the analytically calculated overpressure at 2.5 ms.

2.3.1.2 Friedlander Wave Development

The pressure wave traveled along the tube after time t=0 (see Figure 2.14A). The secondary pressure pulse behind the initial shock front at 2.5 ms suggested the trailing waves may not have fully caught the initial shock front at this time point. By 5.5 ms, the shock waves had coalesced into one shock front (see Figure 2.14B), which resulted in the characteristic peak and decay of the overpressure-distance curves. At the end of the tube, the trace had a R^2 of 0.755 when compared to the ideal Friedlander waveform (see Figure 2.15). The reduced accuracy of the curve to the Friedlander was due to poor representation of the negative phase of blast. The positive phase was well captured.

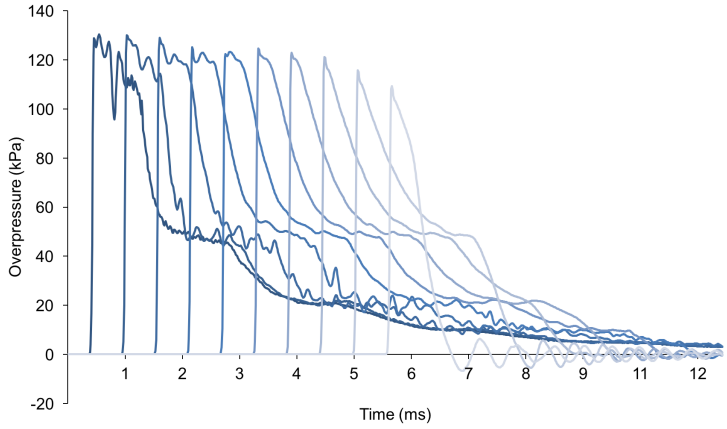

(A)

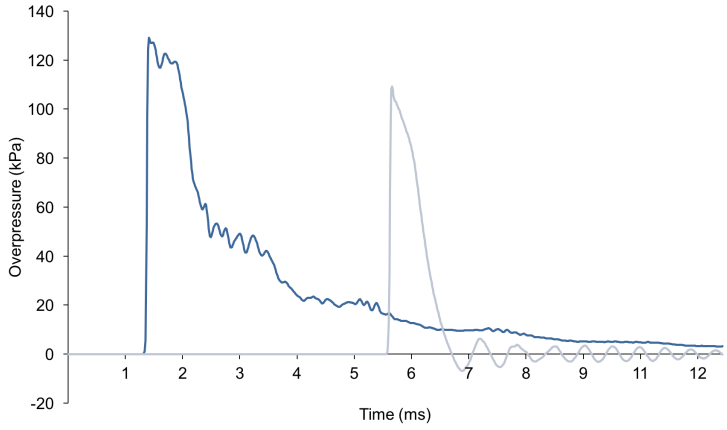

(B)

Figure 2.14: Development of shock wave shape during propagation though model shock tube driven section. (A) Curves from left to right are sequential along the driven section. (B) Comparison of non-Friedlander wave at 1.2 ms and Friedlander wave at 5.5 ms.

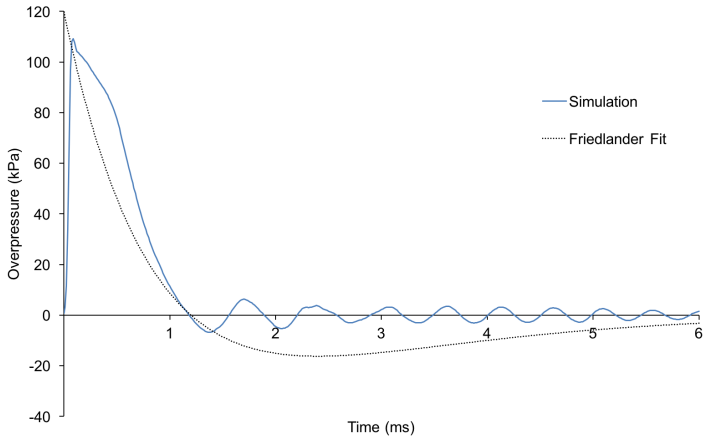

Figure 2.15: Comparison of simulated waveform developed at 6 ms with idealized Friedlander fit yielded a R^2 of 0.755.

2.3.1.3 Driver Gas Selection

Lighter driver gases resulted in smaller positive phase durations than air driver gas (see Figure 2.16). Specifically, the positive duration of helium was 1.87 ms, hydrogen was 1.49 ms, and air was 7.96 ms. This difference corresponded to the relationship between driver gas densities and inversely to the gas constants (see Figures 2.17). Additionally, lighter driver gases formed the Friedlander wave faster compared to air.

2.3.2 Shock Tube Experiments

2.3.2.1 Animal Placement

The results from each of the sensors along the length of the tube are shown in Figure 2.18. The peak overpressure did not vary substantially along the length of the tube, but the positive phase duration decreased as the wave traveled through the driven section. Similar to the finite element simulation, the Friedlander waveform did not develop until the final sensor located 443 cm along the driven section. The development of the Friedlander waveform, absence of membrane fragments traveling down the tube, and high-speed visualization of the light diffraction from the shock front discontinuity (Figure 2.19) provides confirmation an open field primary blast was being generated. The pressure wave at the sensor location was consistent for given driver pressure and membrane thickness, with less than 10% variability (standard deviation) in both peak overpressure and positive phase duration.

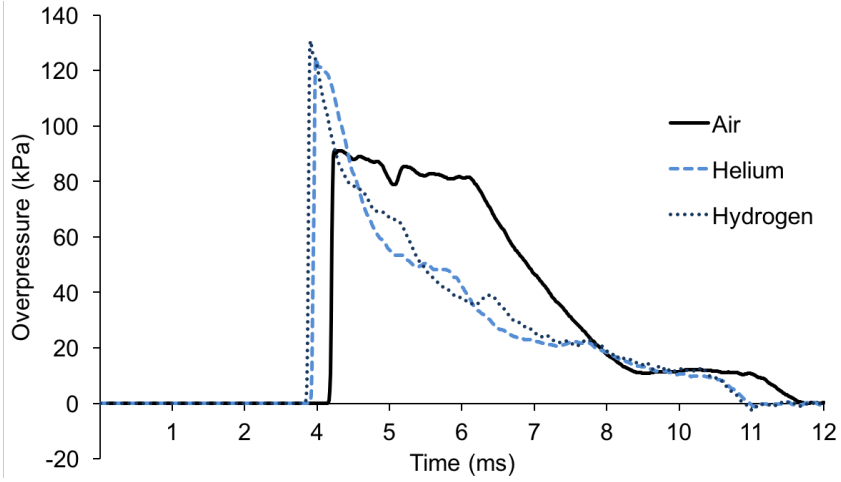

Figure 2.16: Pressure traces extracted at 2.5 ms after blast for the three driver gases. Helium and hydrogen pressure-time curves already converging towards Friedlander shape, while air required more time before converging.

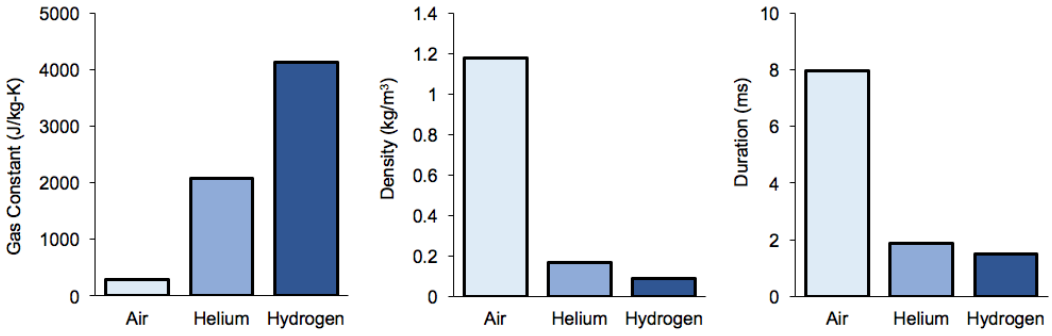

Figure 2.17: Gas constant, density, and positive phase duration for each driver gas. Duration correlated with driver gas density and was inversely related to driver gas constant.

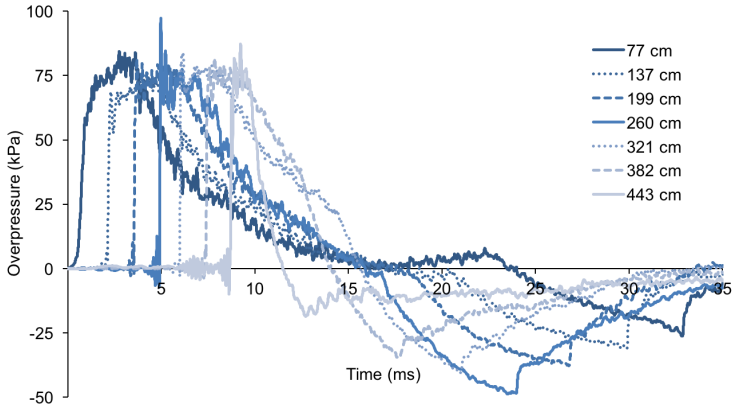

Figure 2.18: Development of shock wave shape during propagation through shock tube driven section. Curves from left to right were sequentially further along the driven section and are labeled by distance from the burst membrane. The shock front shape converged towards the Friedlander pressure profile. The location chosen for animal studies was 2 cm after the final sensor (at 443 cm) in the tube, 445 cm from the membrane.

Figure 2.19: Still image from high-speed video (recorded at 200,000 frames/second). Light diffraction at vertical shock front can be seen as indicated by red arrows. Clay rat surrogate was used for this video recording.

2.3.2.2 Membrane Characterization

Thicker BoPET membrane thicknesses ruptured at higher driver pressures were capable of producing correspondingly higher overpressures. For each membrane thickness, the efficiency of the blast increased with driver pressure (see Figure 2.20). Membrane ruptures at lower driver pressures resulted in poor quality membrane rupture and less efficient transfer of energy (<35%) into the shock front. At a given driver pressure, thinner membranes were more efficient than thicker membranes. Experiments with multiple, layered membranes resulted in poor energy transfer and were discontinued.

Rupturing the membrane using the pneumatic arrowhead resulted in large pressure variability due to variance in driver pressure at rupture. Firing the shock tube at the natural rupture pressure of a given membrane resulted in the lowest variability in blast overpressure and higher efficiency than manual rupture with the arrowhead. The 0.127 and 0.178 mm membranes were not strong enough to withstand sufficient driver pressures to generate peak overpressures over 220 kPa. The 0.254 mm thickness membranes created peak overpressures of 220-250 kPa, which better captured the target range.

2.4 Discussion

Development of the FE model of the shock tube allowed an investigation of varied driver gas and experimental location on the developed wave parameters. The FE model accurately predicted both the formation of the Friedlander waveform near the end of the shock tube and the peak overpressure in comparison to the analytical prediction. The model did not replicate the negative phase of the pressure profile, but the overall accuracy of the positive phase to the Friedlander was $R^2 = 0.941$. The peak overpressure of the model

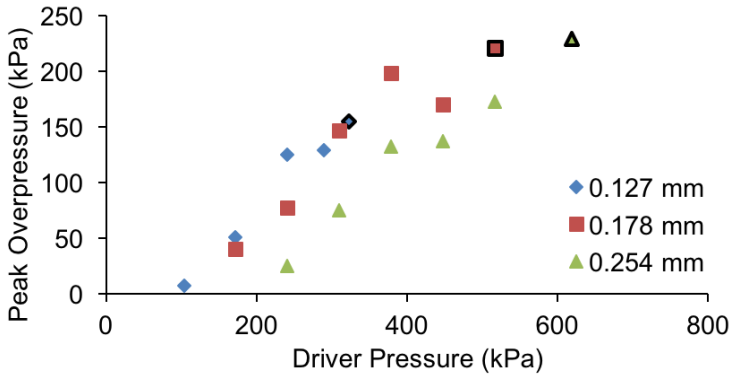

Figure 2.20: Efficiency of shock wave formation calculated at experimental location for a range of BoPET membrane thicknesses. Bordered data points indicate natural failure.

matched the analytical solution with low error (1.2%). Modeling a region of ambient air at the pipe exit may improve representation of the negative phase and likely reduce the ringing behavior seen in Figure 2.14. The model could potentially be used as a tool for evaluating modifications to the tube aimed at tuning blast pressure or duration. For example, many shock tubes feature expansion cones, or adjustable driver section lengths, and both features would be straightforward to implement in the FE model. Thus, the effect of a planned shock tube modification can be quickly evaluated.

The computer model indicated that the Friedlander wave could be developed using any of the driver gases modeled. The positive phase duration of blast was most sensitive to the selected gas, varying between 1.49 and 7.96 ms in the driver gases modeled. As the driver gas fills the driven section after tube firing, the use of driver gas other than air introduces a suffocation risk to the subject. This difficulty could be overcome by quickly removing the animal from the tube, or by flushing the tube with ambient air immediately after the blast insult. Compressed air is cheap to supply and easy to use as a driver gas and it still achieved a Friedlander waveform by the end of the simulation. For these reasons, air was selected as the gas for all experimental studies in Chapter 3. The positive phase duration predicted by the simulation was 7.96 ms. If future studies are desired with shorter positive phase duration, this could be achieved by changing either the driver gas or the driver section geometry.

Experimental characterization of the shock tube demonstrated the desired formation of the Friedlander shock wave. A variety of membranes were tested to determine the optimal membrane material and thickness to generate an appropriate peak overpressure for animal studies. The efficiency of each potential membrane was highest near the failure pressure. In the computer model, the simulation assumed ideal membrane rupture: instantaneous and with no associated energy loss. Rupturing and deforming a physical membrane is nonideal, occurring at a finite rate and requiring a nonzero quantity of work [72]. The rupture of the membrane therefore consumes some portion of the energy stored in the pressurized driver section. The decreased efficiency of the transfer of energy between driver section and shock wave at low driver pressures is partially attributable to this energy loss, which is more significant at low driver pressures (lower total energy), than at higher driver pressures. Portions of the potential energy initially stored in the driver section are also lost into the exit jet (gas movement) and boundary effects.

The 0.254 mm BoPET membrane was selected for animal studies. This membrane thickness was able to reliably generate blast overpressures of 228±28 kPa (within our

targeted range) without the use of the arrowhead rupture device. This pressure was produced with efficiency of 36.8±3.6%. The reproducibility of the overpressure and positive phase duration was sufficient for animal studies. Metal membranes had excessive strength for the driver pressures used in these studies, but could be useful in future studies utilizing higher driver pressurization. With metal membranes, scoring the membrane in a cross pattern would be recommended to ensure even rupture of the membrane to create maximum airflow and reduce energy loss due to membrane rupture. Thinner plastic membranes could be used to generate lower strength blasts suitable for smaller experimental subjects (i.e., mice).

Both the computer model and characterization studies of the physical shock tube gave insight into the ideal positioning of the animal subject, which was determined to be located in the last 0.5 m of the shock tube. Placement of the animal inside the tube would induce reflections into the blast profile, disrupting pressure measurements downstream. For this reason, it was deemed important to place the experimental region directly downstream of a pressure transducer, allowing the pressure wave to be captured immediately prior to interacting with the animal subject. The ideal animal location was therefore located at 445 cm from the membrane, and 2 cm downstream from the final tube sensor.

The shock tube developed in this project is a tool for applying moderate blast loading to targets with an accurate Friedlander waveform. The shock tube is capable of developing shock waves up to 345 kPa (50 psi), using increased driver pressures. The major limitations of the tube are the experimental specimen size and difficulty in adjusting pressure wave duration. The experimental size is limited by the diameter of the driven section, which could be addressed in the future by adding an expansion cone to the driven section as used by the Walter Reed Institute [73], which would allow larger animal models to be utilized. Adjustments to the driver gas or modifications to the driver section length can be utilized to adjust the positive phase duration and total energy of the shock wave

2.5 Conclusion

This research demonstrated Friedlander shockwave formation in the Utah shock tube. Device blast parameters were ascertained using Combined Eulerian-Lagrangian computational simulations and through physical characterization with the tube. Ideal animal placement was identified at a location 445 cm from the burst membrane. This location resulted in a shock profile with a 228 kPa peak overpressure and 7 ms positive phase duration. The relationships connecting driver gas, driver pressure, and membrane to blast

metrics such as peak overpressure and positive phase duration were ascertained. Lighter gases, such as hydrogen, were found to decrease phase duration and result in Friedlander wave formation earlier in the tube. Blast pressure efficiency between the driver and driven sections of the tube were increased with natural rupture of thinner membranes, and 0.254 mm BoPET membranes were selected for blast studies. Finally, operation of the tube was improved to eliminate failed blasts (membrane clamps), decrease noise levels (silencer/catch tank), and increase the operating range of the device (pressure upgrades). The work and findings from this research will be used to form the experimental setup for the animal experiments in Chapter 3.

CHAPTER 3

QUANTIFY LONG-TERM VISUAL SYSTEM INJURY CAUSED BY BLAST EXPOSURE

3.1 Introduction

Several animal models generating ocular trauma from primary blast exposure have been reported, but the methodology used in each of these models varies dramatically. Studies have used different animal species (mouse [11], [19], [20], [65], [66], rat [13], [23], [55], rabbit [56]), different mechanisms for blast generation (shock tubes [55], [74], blast chambers [66], [75], paintball guns [11], [19], [20], [65], rifles [14], and small magnitude explosives [67]), and focused on different pressure magnitudes and durations. Additionally, the orientation of animals relative to blast, timepoints, and assessment methodologies differ widely. These variations make direct comparison and interpretation challenging.

3.1.1 Animal Orientation

The two most common animal orientations are front-on and side-on. The frontal arrangement exposes the full body to blast, so experimental subjects may be more susceptible to lung injury in this configuration, leading to higher fatality rates. Additionally, because of the anatomical location of the eyes in the side of the head in the rodent, this exposure differs from a front-on blast in a human due to interactions with the snout and face. However, the advantage of the frontal blast configuration is that both eyes are loaded symmetrically [74], effectively doubling the sample size of the study. The frontal configuration also reduces the possibility of whiplash from the blast wind.

In side-on orientation, one eye is directly exposed to blast while the second eye is indirectly exposed. This orientation is common in studies which place the animal at the end or outside of the shock tube [14]. Placing the animal outside the tube can fully isolate the primary injury mechanism by avoiding the exhaust jet, but the results are extremely sensitive to animal placement. Side-on blast exposure in an animal model may also be more

representative of a frontal exposure in a human due to the lateral placement of eyes in many of the animal models used (including mice, rats, and rabbits) [76].

3.1.2 Injury Assessment

In addition to the many methods used to recreate blast exposure (Chapter 2), damage to the visual system is also assessed using a variety of methods. Common techniques include behavioral assessments of visual function, optical coherence tomography (OCT) imaging, gross pathology, and microscopy or protein analyses with enzyme-linked immunosorbent assay (ELISA), immunofluorescence, and other histological techniques. The time course of testing after blast exposure also varies, with some researchers comparing results pre- and postblast exposure, others performing sequential tracking over time, and some using only one testing timepoint.

Hines-Beard et al. exposed mice to one of three blast levels using a modified paintball gun [20]. The experimental setup created a long duration positive pressure wave (12-18 ms) with reflected blast overpressures of 163, 182, or 210 kPa. Visual system injury was assessed with acuity testing, measurements of IOP, gross pathology, and OCT up to 28 days after blast. Visual ability decreased by 4 weeks after blast exposure, but was not statistically significant due to limited sample size. In general, it appeared that damage induced by the blast trauma was still progressing at the final time point 28 days after the exposure.

In 2013, Zou et al. used open field explosion of 5-kg trinitrotoluene (TNT) to induce ocular trauma in rats [67]. The explosive generated 480 kPa blast pressure at 2m and 180 kPa at 3m. Histological findings in the retina were assessed using western blotting analysis, ELISA, and immunoflourescence staining. Retinal thickness increased relative to control animals at 72h and 2 weeks after blast. Damage to the blood retinal barrier was a suspected cause of the thickening due to increased vascular endothelial growth factor (VEGF), astrocytes, and glial fibrillary acidic protein (GFAP) in blood vessels.

More recently, Choi et al. studied the effects of single and repeated blast overpressure on rats using immunohistochemistry analysis looking for increased GFAP in the retina and activated caspase-3 in the optic nerve. [55]. A compressed air shock tube was used to deliver 70 kPa blasts (duration = 2ms) to rats positioned inside the tube. Single blast exposed rats were sacrificed 5 days after the exposure. The repeated blast group underwent five blasts on consecutive days (one exposure per day) and were sacrificed immediately after the final blast exposure. Repeated exposure led to increased caspase 3 expression and increased GFAP expression, with damage to both the ganglion cell and inner nuclear layers of the retina.

These studies illustrate that ocular damage from blast can be successfully recreated in the laboratory with varying degrees of fidelity to the ideal Friedlander waveform [77]. Retinal thickening, retinal thinning, apoptosis, gliosis, optic nerve avulsion, and loss of photoreceptors are among injuries reported in these studies [20], [55], and injuries seen clinically in human patients [78]. Fewer studies have focused on the anterior portion of the eye, such as the cornea. Hines-Beard et al. noted corneal damage at 7-14 days after blast, but comprehensive tracking of the corneal response to blast is lacking [20]. Furthermore, nearly all blast ocular studies to date have focused on injury sequelae less than 4 weeks after the blast. The exception to this is a study by Mohan et al. evaluating chronic retinal ganglion cell function in different aged mice following blast exposure [66]. Based on the findings of Mohan et al. and those reported by Hines-Beard et al., visual system injuries appear to progress after 4 weeks post blast.

3.2 Methods

3.2.1 Blast Exposure

All animal studies were reviewed by the Institutional Animal Care and Use Committee (IACUC) of the University of Utah. Male Long-Evans rats (n = 54, 399±68g, age 10-14 weeks) were administered carprofen PO (20 mg) 1 day before and 1 day after blast exposure for pain management. On the day of blast exposure, inhaled isoflurane (5%) was administered for light sedation followed by intraperitoneal injection of ketamine (65 mg/kg) and dexmedetomidine (0.14 mg/kg). Anesthesia depth was assessed using toe pinch and eye touch reflexes. Rats were wrapped in a Kevlar shroud up to the neck and placed in a custom 3D-printed holder (see Figure 3.1A) bolted to the tube (see Figure 3.1B), such that the right eye was directly exposed and the left eye was indirectly exposed to the blast (see Figure 3.2). The holder kept the body of the animal outside of the tube and protected from injury. The head was restrained using Velcro strap to prevent excessive head motion. The animal was monitored from an external rear viewing port before and during the blast. Ketamine anesthesia caused relaxation of the orbicularis oculi muscles and therefore the eyelid remained open throughout blast exposure. Control animals (n = 38, 38±53g) were anesthetized similar to the blast exposed animals but were not exposed to a blast. In a subset of animal studies, (n = 4) high-speed video was performed to visualize the motion of the animal inside of the shock tube. A 228 kPa blast exposure with approximately 7 ms positive phase duration was generated using the shock tube described in Chapter 2.

After blast exposure, the holder was removed from the shock tube and the animal

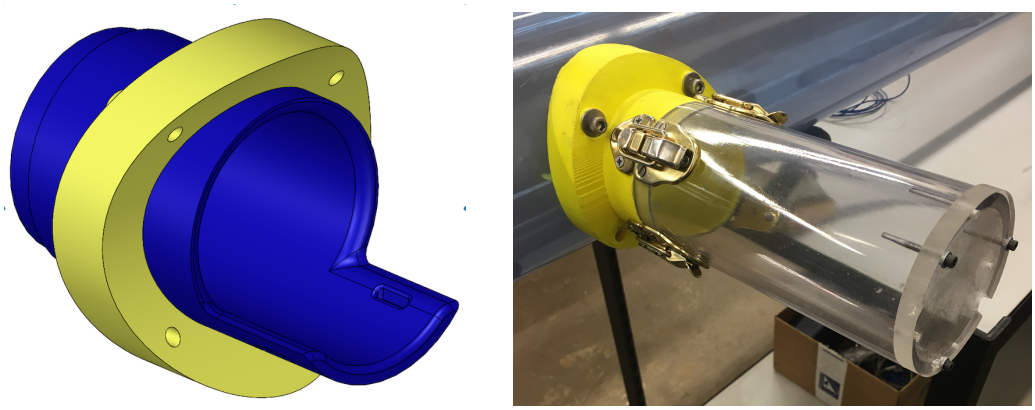

(A) (B)

Figure 3.1: Design of holder to immobilize rat while exposing head to inside of shock tube. (A) Solidworks model for 3D printing showing restraint points. (B) Holder bolted to shock tube using four bolts through the collar section. Clear construction allows monitoring of vitals in anesthetized animals.

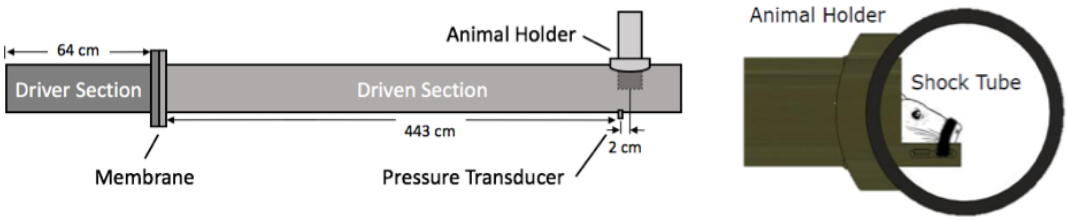

(A) (B)

Figure 3.2: Schematic of holder and animal with relation to the shock tube. (A) A sensor located 2 cm upstream from the animal recorded tube pressure. (B) The right eye was directly exposed the side-on blast.

was inspected for injury. Genteal lubricant eye drops (Alcon, Hunenberg, Switzerland) were applied immediately after blast and at 45-min intervals until recovery of normal blinking. This ensured eyes remained adequately hydrated during the recovery period to avoid the development of dryness and increased corneal opacity. Animals were kept on warming pads and monitored until recovery from anesthesia, at which time they were returned to cages. Animals were kept in standard day-night cycles and provided with food and water ad libitum.

3.2.2 Assessment Timeline

Control and blast exposed rats survived 1 day, 1 week, 4 weeks, or 8 weeks postblast. Baseline contrast sensitivity testing and optical coherence tomography (OCT) of the cornea and retina were performed 1 day prior to blast exposure. Assessments were repeated 1 day after blast exposure, and then weekly until their survival time point (see Figure 3.3). Eyes were collected at each sacrifice endpoint for histology and vitreous proteomic analysis.

3.2.3 Contrast Sensitivity Testing

Visual ability was assessed by contrast thresholding with an optokinetic nystagmus (OKN) test system. The system was designed and built in-house based on similar testing apparati [79], [80], and was comprised of four LCD displays surrounding a transparent animal enclosure (see Figure 3.4A). A closed-circuit video camera provided visualization of the animal during stimulus tracking. The monitors displayed sinusoidal drift gratings rotated clockwise or counterclockwise around the animal enclosure driven via a custom MATLAB (Mathworks, MA) code using the Psychophysics Toolbox extensions [81], [82]. Visual ability of the animal was measured by whether the moving stimulus was correctly tracked by the head and eyes. The drift speed (1.5 Hz) and bar spacing (0.136 rad/cycle) were held constant throughout the test, while the contrast of the grating was varied in 20% increments using a two-down, one-up staircase algorithm [83]–[85].

Before testing, the screens displayed a neutral gray background and the animal was placed in the center of the OKN testing platform. A wait period of approximately 5 min was allowed for the animal to acclimate to the test environment. The contrast grating was initiated and the test continued until a total of six contrast reversals (down-up or up-down) were recorded (see Figure 3.4B). The contrast change between trials was cut in half after three reversals (halfway through the test) to more accurately hone in on a threshold. The final three reversals were averaged to define the contrast threshold.

Each test was repeated three times. The thresholds established at the end of each

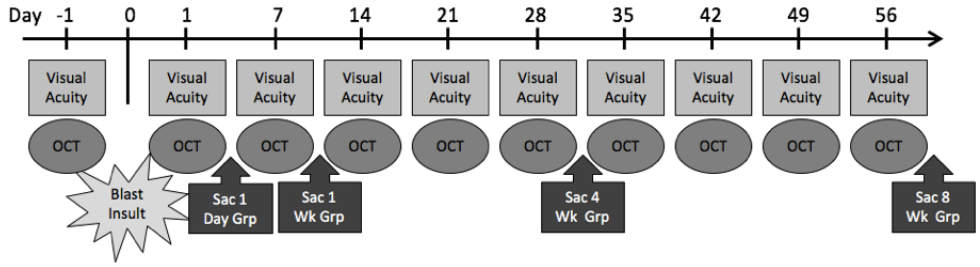

Figure 3.3: Experimental timeline of blast exposure, testing, and study endpoints.

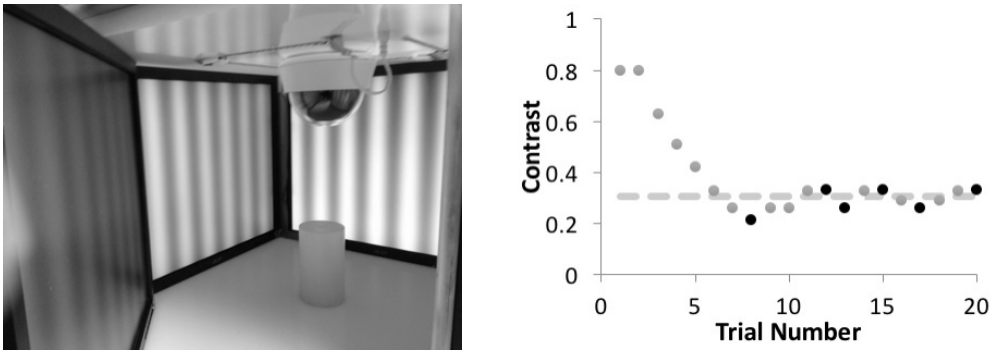

(A) (B)

Figure 3.4: Contrast sensitivity device and representative testing output. (A) Behavior apparatus showing drift grating on external monitors and overhead camera for tracking animal response. (B) Sample test result. Each light dot represents a single stimulus. Dark dots indicate the six reversals of contrast trending direction. The dashed line represents the calculated contrast sensitivity threshold based on the average of the three final reversals.

test were recorded, with the average result of the three tests used for further analysis. All tests were performed by one examiner to maintain consistency.

3.2.4 OCT Imaging

OCT imaging of the retina and cornea was performed using an Envisu R220 Spectral Domain OCT (Bioptigen, Durham, NC). Rats were anesthetized with 4% isoflurane, and pupils dilated with 0.5% tropicamide for 3-5 min prior to imaging. The anesthetized rats were placed on the test bed and imaged using the Bioptigen rat retina lens. Retinal images were captured in a 2.6x2.6 mm field of view, with 1000 A-scans/B-scan and 100 total B-scans. The Bioptigen telecentric lens was used to image the cornea using the same A-scan and B-scan parameters, over a 4x4mm field of view. OCT imaging was performed in both right and left eyes.

Stromal, epithelial, and overall corneal thickness were extracted from the corneal images by measuring the thickest point of each layer using digital calipers (see Figure 3.5A). Overall retinal thickness and retinal pigment epithelium (RPE) were calculated by manually selecting a total of forty edge sets per OCT image stack, with four measurements taken on each of ten B-scans spaced throughout the stack. The retinal nerve fiber layer/ganglion cell layer (NFL/GCL) thickness measurements were generated with a custom MATLAB program which calculated the layer edges in every column (A scan) across each B-scan (green in Figure 3.5B). The optic nerve region was omitted from the measurement, as were blood vessel regions (red in Figure 3.5B). Thickness measurements were divided into 8 radial quadrants around the optic nerve, with four central and four peripheral sections as shown in Figure 3.5C.

3.2.5 Histology and Vitreal Protein Analysis

At sacrifice, rats were euthanized by overdose of inhaled isoflurane and transcardially perfused with phosphate buffered saline (PBS) and formalin. Eyes were extracted to be used for histology (control $n = 18$, blast $n = 22$) or vitreous biomarker studies (control $n = 12$, blast $n = 20$). Eyes for histology were stored in 4% formalin or EZ-Fix (Excalibur Pathology, Norman, OK). Eyes were sectioned (5 μm thickness) at five transverse levels. Slides were stained with hematoxylin and eosin (HE) and terminal deoxynucleotidyl transferase dUTP nick end labeling (TUNEL) staining. Stained slides were examined for injury by a veterinary ocular pathologist masked to the blast exposures.

The eyes used for vitreous protein analysis were eviscerated and the vitreous and lens removed. The vitreous and lens were separated by placing them into a filter centrifuge

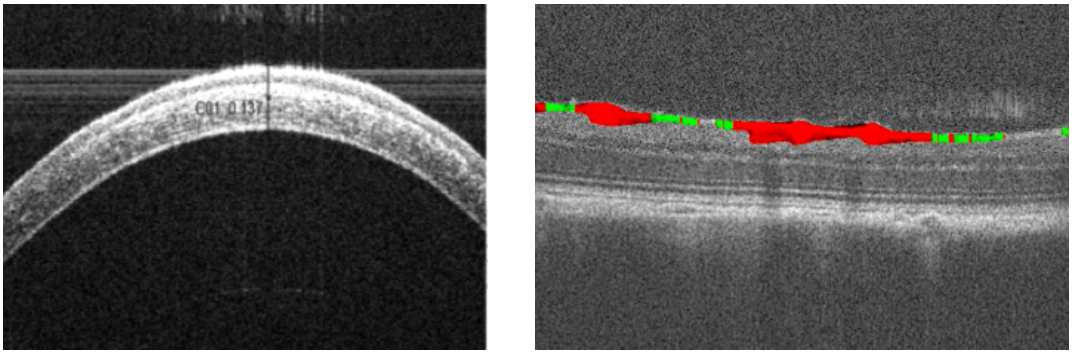

(A) (B)

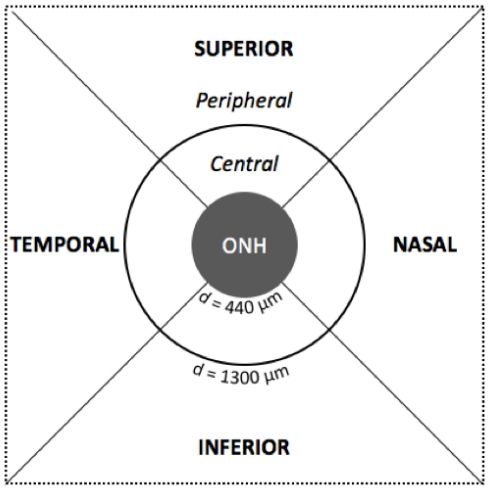

(C)

Figure 3.5: Image analysis procedures for OCT of rat cornea and retina. (A) Corneal image illustrating how digital calipers were used to measure the overall thickness. (B) Retinal image with NFL/GCL layer measurements overlaid (green). Red regions omitted due to the presence of blood vessels. (C) Regions used for analysis of retinal thickness. The optic nerve head (ONH) was used to center the image and was omitted from the thickness analysis.

tube and spun down (10k rpm, 10 min). The separated vitreous (approx. 50 μL) was diluted with phosphate buffer saline (PBS) until a total volume of 150 μL was reached. The sample was then separated into three equal tubes for quantification of Neurofilament Heavy Chain (NfH) and inflammatory cytokines.

To quantify NfH, an ELISA protocol was used according to a technique previously developed by Petzold et al. [86]. Microtitre plates were coated overnight at 4°C with 100 μL of capture antibody, SMI35. The plates were washed three times for 10 min using a barbitone buffer containing 0.1% BSA, and 0.05% Tween 20. After washing, 250 μL of

barbitone block with 1% BSA was added to each well and the plate was incubated at room temperature (RT) for 1 h. After another wash cycle, 50 μL of sample, standard, or negative control was added to each well of the plate in triplicate. After 1 h incubation at RT the wash processes were repeated. After washing, 100 μL of second antibody was added to each well of the plate and incubated for 1 h at RT. Following a third wash cycle 100 μL HRP-labeled swine antirabbit antibody was added to the plates and incubated for 1 h at RT. After a final wash 100 μL TMB substrate was added and incubated for 20 min in a dark room, the reaction was stopped by adding 50 μL of 1 M HCL. The absorbance was read using an ELISA plate reader (Synergy HT Multi-Mode Microplate Reader, BioTek, Winooski, VT) at 450 nm with 750 nm reference wavelength.

Quantification of the inflammatory cytokines was performed using a commercially available array (RayBio Rat Cytokine Antibody Array G). These arrays tested for 19 cytokines including VEGF, LIX and TNF-α. Arrays were processed according to the manufacturers instructions, and the intensities read using a GENEPIX 4000A microarray scanner at an excitation frequency of 532 nm. Cytokines quantification was normalized using positive controls.

3.2.6 IOP Measurement during Blast

In a separate animal set (n = 10), fiber optic pressure sensors (FISO FOP-LS-2FR-30, Quebec, Canada) were placed in each eye to measure the intraocular pressures (IOP) in the directly and indirectly exposed eyes during a blast. Animals were anesthetized as previously described, but dexmedetomidine dosage was increased to 0.25 mg/kg. The lateral commissure was clamped with a hemostat for several seconds to limit bleeding, and then cut to gain access to the posterior half of the eye. The IOP transducers were prethreaded through surgical tubing and into the midsection of an 18G hypodermic needle. Tweezers were used to grasp the conjunctiva near the commissure and rotate the eye in the medial direction. The needle containing the pressure transducer was inserted through the posterior sclera and positioned into the central vitreous chamber. The conjunctiva was released and the eye allowed to gently rotate back into its natural position. Skin sutures and cyanoacrylate adhesive secured the surgical tubing to the back of the rat to limit sensor cable motion during animal positioning and blast wave exposure. The procedure was repeated for the other eye. Rats were secured in the blast tube and exposed to blast as previously described. After blast exposure, animals were euthanized and sensors removed. Due to the mechanical trauma of the IOP procedure, these animals were not used for histology or biomarker studies.

The fiber optic transducers were connected to the FISO signal conditioner with a sampling frequency of 15 kHz. Data from the signal conditioner were recorded with the same acquisition system as the tube-mounted pressure sensors. The IOP data were not filtered because the sample rate from these sensors was below the cutoff frequency used for the tube pressure sensors. IOP traces were analyzed in MATLAB to record peak pressure; rise time; initial slope; and positive, negative, and net impulse for each curve.

3.2.7 Statistical Analyses

Statistical analyses were performed using R (RStudio Inc., Boston, MA). Contrast sensitivity at each time point was compared to the animal's baseline score using a two-tailed matched pair Students t-test, with the Bonferroni correction for multiple comparisons. At each time point, the control group was statistically compared to the blast exposed group via a two-tailed Students t-test. All analyses were performed using an $\alpha = 0.05$ confidence level. The same statistical comparisons were used to assess differences from baseline and from time-matched controls for corneal and retinal layer thicknesses. Statistical comparison between the pressure waveform characteristics in the tube and in the eyes was performed using a one-way matched pair ANOVA with the same Type I error ($\alpha = 0.05$).

3.3 Results

The average ± standard deviation peak overpressure and positive phase duration applied during blast exposure were 228.49±28.49 kPa and 7.06±0.64 ms, respectively. Additional blast characteristics are provided in Table 3.1. A sample time history trace compared to the Friedlander waveform is shown in Figure 3.6.

The overall mortality rate for all blast exposed animals was 7.4% (4/54). A single animal died 15 min after blast, despite showing no immediate signs of injury directly after the blast exposure. Two blast exposed animals experienced apnea immediately after blast

Table 3.1: Summary of blast characteristics from animal blast exposures.

Blast Parameter	Avg Value ± Std. Dev.
Peak Overpressure (kPa)	228.5 ± 28.5
Peak Negative Pressure (kPa)	-50.8 ± 6.6
Positive Phase Duration (ms)	7.1 ± 0.6
Negative Phase Duration (ms)	21.6 ± 2.0
Positive Phase Impulse (Pa·s)	680.5 ± 66.9
Negative Phase Impulse (Pa·s)	571.6 ± 77.9
Net Impulse (Pa·s)	1250.7 ± 102.0

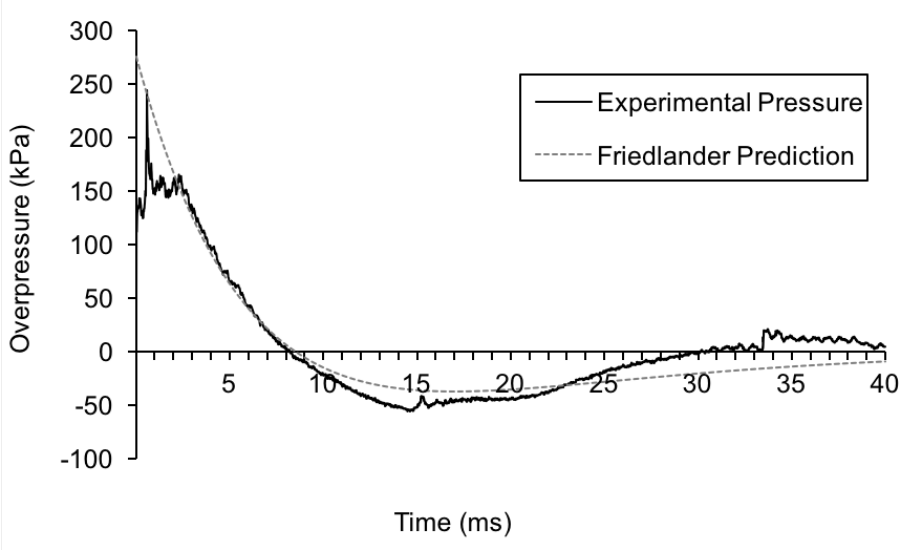

Figure 3.6: Overpressure generated by shock tube compared to idealized Friedlander waveform.

and did not recover. The last animal experienced apnea 30 s after removal from the shock tube (approximately one minute from blast exposure) and did not recover. Two surviving animals also experienced apnea immediately after blast. One recovered spontaneously after approximately 10 s, and the other was manually resuscitated until recovery (30 s). Incidental minor injuries include nosebleed (2/54) and tongue bite (2/54).

Corneas were examined in a subset of animals ($n = 4$) using fluorescein dye roughly 5 min after blast exposure. No abrasions or abnormalities were found, verifying that no secondary contact injuries were inflicted during the blast due to microparticles traveling down the tube. Review of high-speed recordings of blast exposure further confirmed there were no shrapnel injuries.

High-speed video visualized some head movement during the blast exposure. This movement occurred after the primary blast wave had passed by, and was likely caused by movement of air within the tube rather than the pressure wave itself. The holder and restraint straps limited the total displacement of the head, and ensured that the downstream eye did not contact the holder, which would have induced blunt trauma injury mechanisms.

3.3.1 Contrast Sensitivity

Blast exposed animals experienced a measurable and sustained visual system impairment following injury. Contrast sensitivity decreased in blast exposed animals compared to their baseline values the day after exposure and persisted until the end of the study

at 8 weeks (see Figure 3.7). This increase was significant at 1 day, 2 weeks, 5 weeks, 7 weeks, and 8 weeks after blast exposure ($p<0.05$). Contrast sensitivity in blast exposed animals was significantly worse than control animals at all time points after blast exposure ($p<0.05$). Contrast sensitivity in control animals increased from baseline values by 1 week and remained elevated. Statistically significant improvements from baseline were at 3 and 7 weeks after sham blast. ($p<0.05$). This improvement may have been caused by increased comfort with the test enclosure and handling procedures. In a more relaxed state, the animals tended to increase focus on the screens surrounding them.

3.3.2 OCT

Significant structural changes in blast exposed eyes were found with OCT imaging. In general, the changes were temporally delayed from the initial blast exposure by at least 2 weeks. The changes were more substantial in the directly exposed right eye compared to the indirectly exposed left eye, but both eyes experienced significant corneal changes ($p<0.05$).

3.3.2.1 Cornea

Stromal thickness in the indirectly exposed left eye significantly increased by 57±53 μm at one week after blast ($p<0.0001$) and resolved to baseline values by the following week (see Figure 3.8A). Significant stromal thickening was observed in the directly exposed right

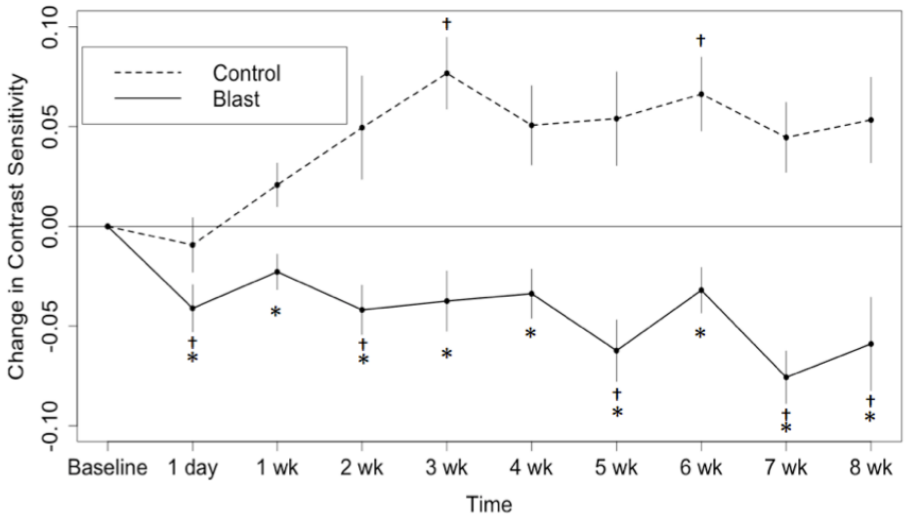

Figure 3.7: Contrast sensitivity changes in blast exposed and control animals over the course of 8 weeks. Error bars indicate standard error of the mean. *Significant differences between control and blast exposed animals at each time point ($p<0.05$). †Significant changes relative to baseline visual ability (Bonferroni adjusted $p<0.05$).

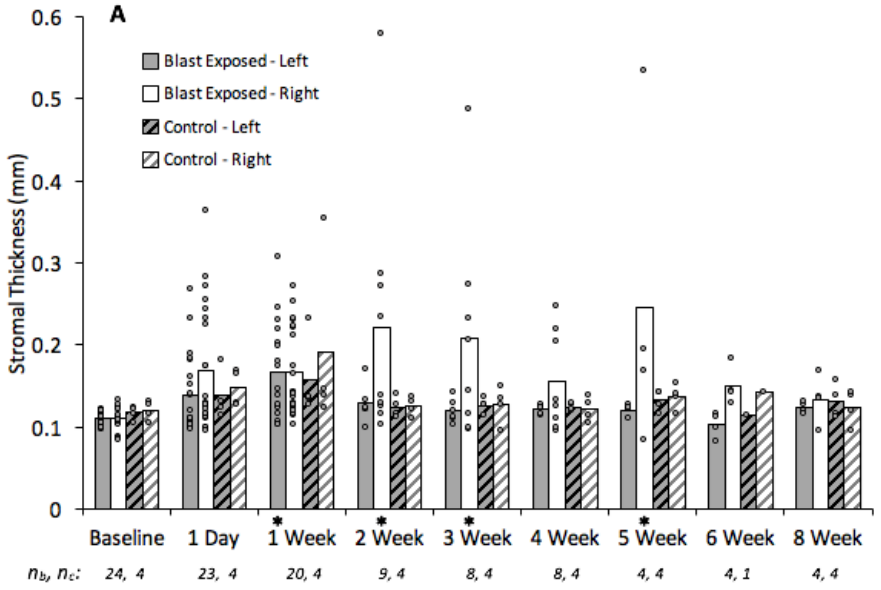

(A)

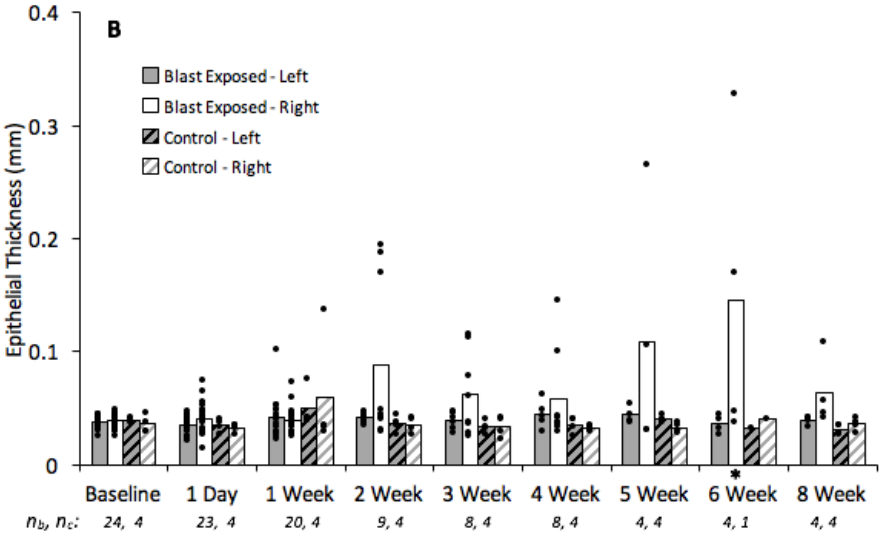

(B)

Figure 3.8: Thickening of the corneal stroma (A) and epithelium (B) as a function of time. Columns represent average thickness with individual thickness measurements overlaid. Significant (Bonferroni adjusted $p<0.05$) changes from baseline are noted by an asterisk (*) below the column. Sample sizes indicated below as n_b, n_c for blast and control, respectively.

eye between 2 and 5 weeks after blast in 42% of the animals surviving at least 1 week after blast ($p<0.033$). The swelling increased by 136±198 μm by week 5. At week 6, both left and right stromal thicknesses returned to near-baseline values, but the right eye was still 40±23 μm thicker than the original baseline measurement. Epithelial thickness of directly exposed right eyes significantly thickened by 107.3±135 μm at 6 weeks after blast (see Figure 3.8B, $\alpha<0.05$). The epithelium decreased to 25±32 μm above baseline thickness by 8 weeks after blast exposure. No significant changes were found in control animals for either the stroma or epithelium.

Although stromal and epithelial swelling mostly resolved by the end of the study, persistent damage was observed in the form of stromal scarring (see Figure 3.9). In total, half of the animals surviving to 8 weeks after blast had corneal thickening at 3-5 weeks, and all of the animals with corneal thickening exhibited stromal scarring at the final study time point. A single control animal (1/38) had corneal thickening at 3-5 weeks; and later experienced stromal scarring at 8 weeks. This injury was thought to be due to an altercation with another animal in the cage.

3.3.2.2 Retina

Retinal thickness changes were not as conclusive as the corneal findings. Statistical analysis of overall thickness found that there was significant thickening of the retina at 7 weeks in the right eye of blast exposed animals when regions were averaged across the central ring (see Figure 3.10, $p = 0.02$). A similar increase was seen in the indirectly exposed eye, but it was not statistically significant. There were no other significant findings in other regions or time points. There were no significant thickness changes from baseline in the RPE layer in any group or time point. The analysis of the combined NFL/GCL likewise found no significant thickness changes from baseline. Retinal image quality varied and was highly dependent on corneal opacity and thickness.

3.3.3 Histology and Protein Analysis

The most common histology injury findings included epithelial irregularity ($n = 17$), axial epithelial defects ($n = 12$), superficial scarring ($n = 5$), and neovascularization ($n = 5$). Epithelial irregularities and defects were seen in both control and blast exposed animals, which was likely due to post processing. Neovascularization was seen only in blast exposed animals. These findings correlate well with the progression of corneal damage seen in the OCT and are summarized in Table 3.2. Lens epithelium swelling was detected in 4/40 (10%) animals. No microscopic retinal injuries were detected in the stained tissues.

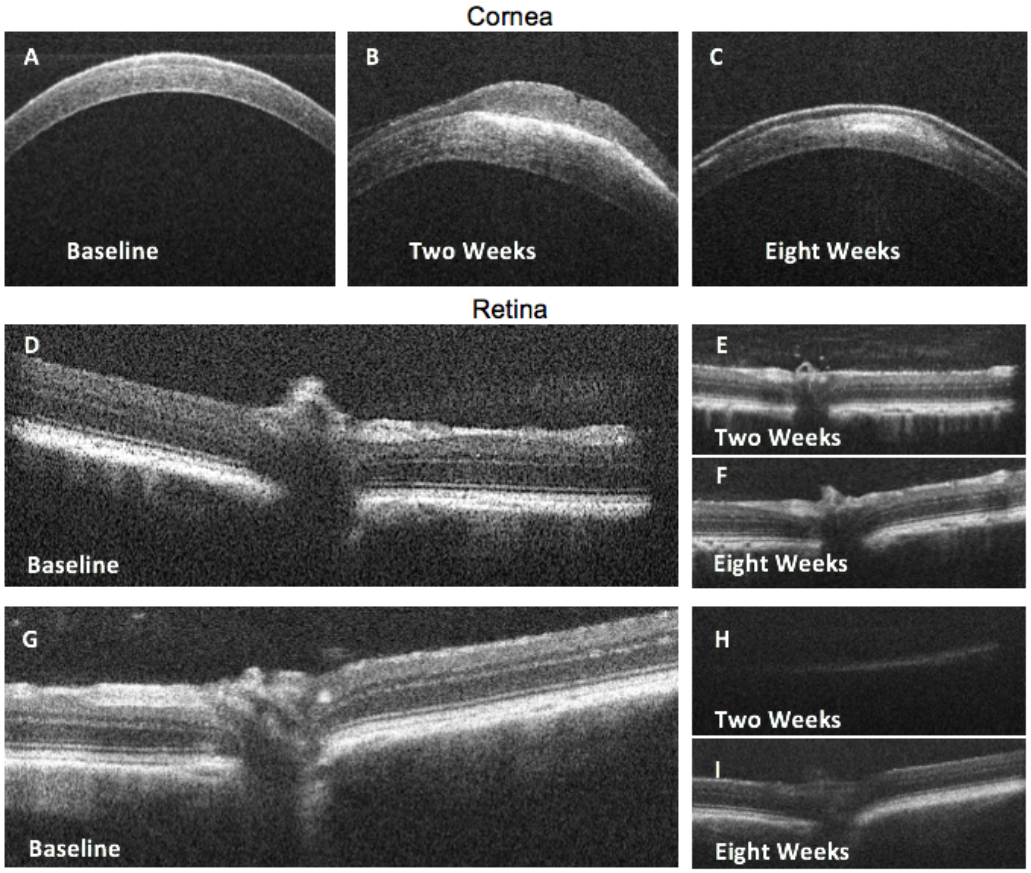

Figure 3.9: OCT timeline of cornea and retina in the right eye (directly exposed) of blast exposed rats. (Top) Progression of corneal damage. (A) All animals at baseline exhibited healthy corneas. (B) Substantial swelling occurred 2 weeks after blast exposure. (C) Thickening decreased 8 weeks after blast exposure but stromal scarring remained. (Bottom) (D-F) Progression of retina in an eye without corneal damage. (G) Baseline image in blast exposed animal that later developed corneal damage shows healthy retina and optic nerve with clear discrimination of retinal layers. (H) At 2 weeks, corneal swelling reduced image quality and no retinal thickness measurements could be made. (I) By 8 weeks, the image quality improved and thickness measurements were recorded.

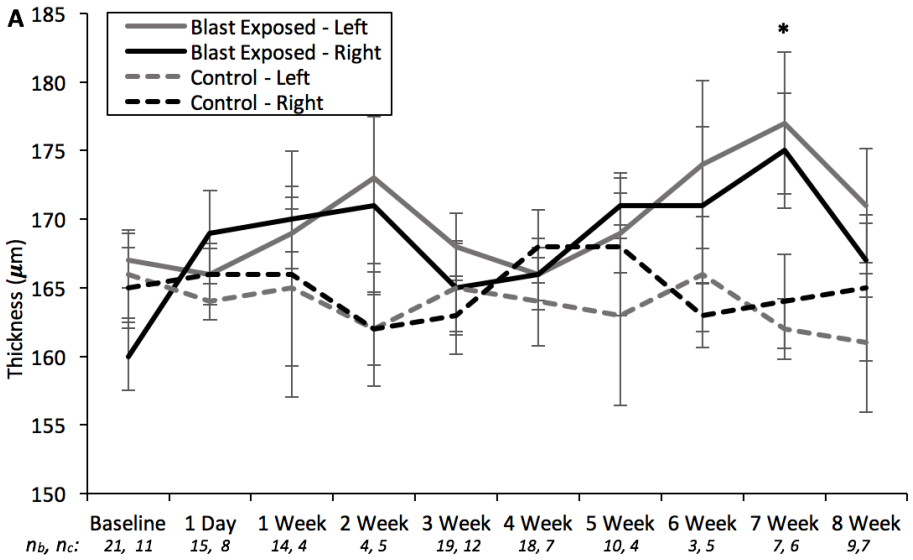

(A)

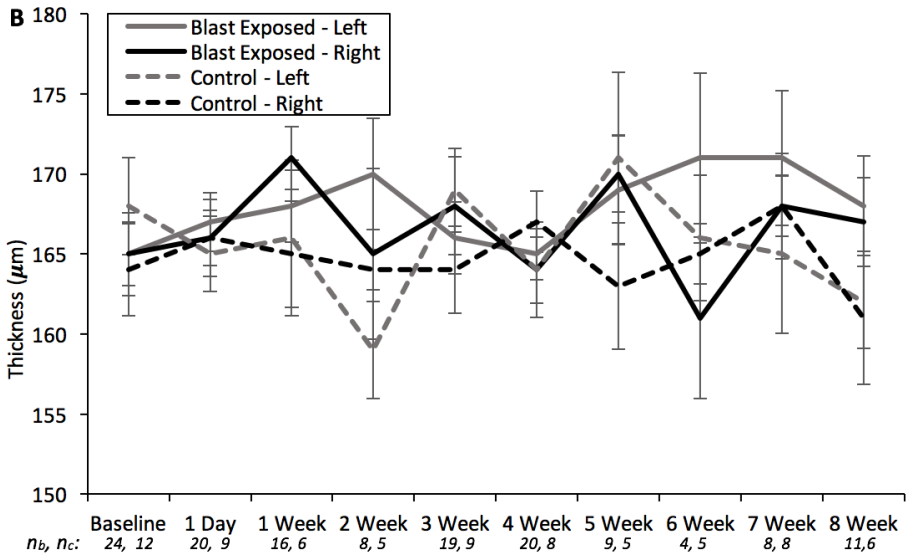

(B)

Figure 3.10: Retinal thickness for direct (right eye) and indirect (left eye) blast exposure. (A) There was significant thickening at 7 weeks in the blast exposed right eye compared to baseline in the central region of the right eye (*$p<0.05$). (B) There were no significant changes in the peripheral region. Error bars indicate standard error. Sample sizes indicated below as n_b, n_c for blast and control, respectively.

Table 3.2: Summary of histology findings (n, %).

	N	Epithelial irregularity	Axial epithelial defect	Superficial scarring	Active keratitis	Neo-vascularization	Lens Swelling	Superficial Calcification
Left								
Control	18	6 (33%)	3 (17%)	1 (6 %)	3 (17%)	-	1 (6 %)	-
1 Day	5	3 (60%)	-	-	-	-	1 (20 %)	-
1 Week	6	1 (17%)	2 (33%)	-	3 (50%)	-	-	2 (33%)
4 Week	5	-	1 (20%)	1 (20%)	-	1 (20%)	-	-
8 Week	6	2 (33%)	-	2 (33%)	-	2 (33%)	-	-
Right								
Control	18	2 (11%)	4 (22%)	-	5 (28%)	-	2 (11%)	-
1 Day	5	-	-	-	-	-	-	-
1 Week	6	2 (33%)	1 (17%)	-	2 (33%)	-	-	2 (33%)
4 Week	5	-	1 (20%)	1 (20%)	-	1 (20%)	-	-
8 Week	6	-	-	1 (17%)	-	1 (17%)	-	-

The left and right eyes of blast exposed animals showed an increase in NfH concentration ($p<0.05$, see Figure 3.11A). Between 4 and 8 weeks, NfH concentration decreased significantly but was still elevated with respect to control. In general, there appeared to be a transient increase in inflammatory cytokine expression at 1 day and 1 week after blast that resolved by the end of the study (see Figure 3.11B). VEGF appeared to increase in blast exposed eyes between 1 day and 4 weeks, but the increase was not significant (see Figure 3.11C). Interleukin 10 (IL-10) intensity significantly increased in the right eye of blast exposed animals at 1 day and 4 weeks after blast, but returned to baseline values by 8 weeks (see Figure 3.11D).

3.3.4 IOP during Blast

IOP was successfully measured in both right and left eyes in eight of the ten animals. During initial blast wave contact with each eye, IOP closely mimicked the general Friedlander waveform. However, after initial contact, IOP readings became erratic. This could have been caused by sensor movement within the eye, contact between the ocular lens and the sensor tip, and/or wave reflection inside the eye. Based on the initial 5 ms of the pressure waveform, it was observed that peak pressure in the directly exposed eye (231.9±40.9 kPa) matched the tube pressure (240.3±39.0 kPa) measured 2 cm in front of the animal within 0.1% with a 0.6775 ms delay (see Figure 3.12). One kPa is equivalent to 7.5 mmHg, so IOP effectively increased from normal IOP (12-22 mmHg) to 1739±307 mmHg during the blast. The IOP peak pressure in the indirectly exposed eye was 30% lower than the directly exposed eye, but this decrease was not statistically significant. Pressurization rate significantly decreased by 61% as the blast wave traveled from the tube into the directly

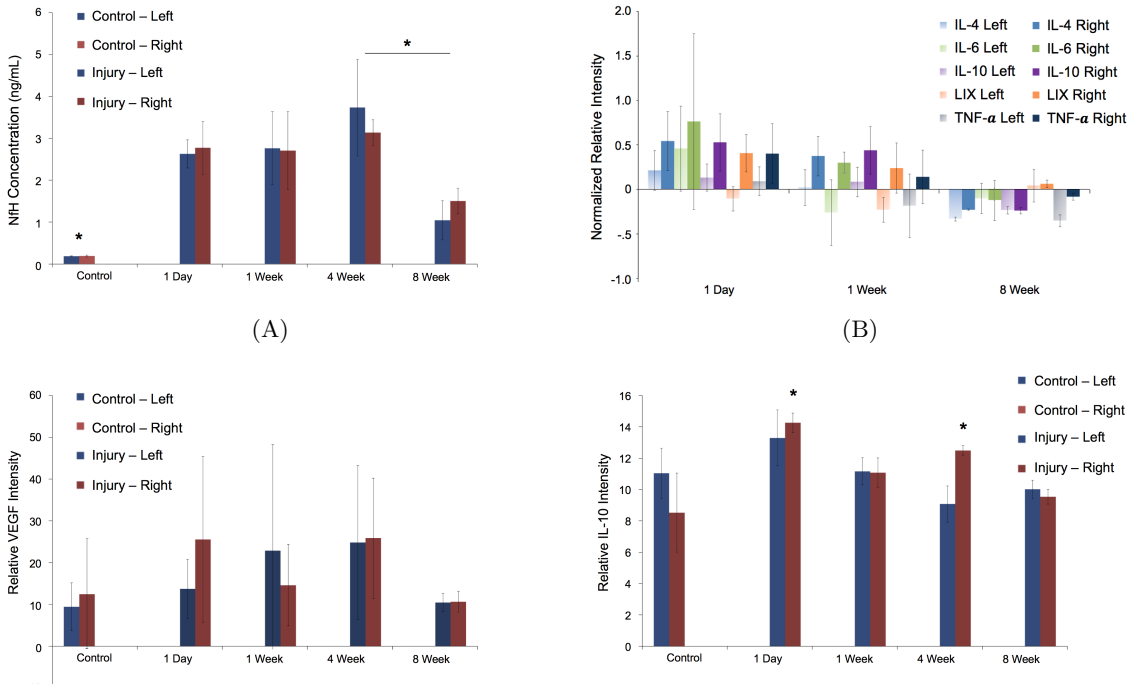

Figure 3.11: Results of vitreous protein quantifications. (A) NfH was significantly greater in injured animals compared to controls for all time points ($p<0.05$). At 8 weeks, NfH significantly decreased towards to control levels. (B) Selected cytokines normalized by relative intensities in control animals. Both eyes had a general increased inflammatory response 1 day after injury, but returned to control levels by 8 weeks. (C) VEGF increased from 1 day to 4 weeks and then returned to baseline, but this trend was not significant. (D) IL-10 was seen to be significantly higher in the right eye at 1 day and 4 weeks following injury compared to controls.

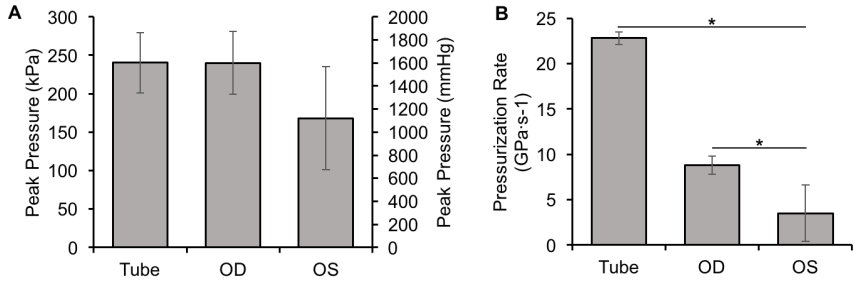

Figure 3.12: Average peak pressure and pressurization rate measured in the shock tube compared to the IOP measured in the left (OS) and right eye (OD) of the animals. (A) There was no significant difference between the peak pressure of the tube and the directly exposed right eye. The peak pressure in the left eye was reduced by 30%, but this was not significant. (B) The pressurization rate was significantly lower in the right eye than in the shock tube and significantly lower in the left eye than the right (*p<0.01).

exposed right eye and significantly decreased by another 60% as the wave traveled through the head into the indirectly exposed left eye ($p<0.01$). The positive phase impulse in the tube and right eye did not significantly differ, but the tube was significantly higher by 32% compared to the left eye ($p<0.05$), and the negative phase impulse magnitude was 35% lower in the right eye than in the tube ($p<0.01$). The net impulses recorded in the tube, left eye, and right eye did not significantly differ.

3.4 Discussion

To improve diagnosis and treatment strategies for blast ocular trauma, it is important to understand the types of injuries that occur as well as the timelines for injury development. The objective of this study was to identify ocular blast exposure sequelae up to 8 weeks. To achieve this objective, we experimentally reproduced open field primary blast ocular trauma in a rodent model, and quantified retinal and corneal structural changes, visual function, histology, and vitreous protein changes for a two month period. Side-on blast was used in this study to limit the exposed area to the head and eye, while protecting the trunk and specifically the lungs of the animal. *In vivo* IOP was measured during some blast exposures to quantify the difference between directly and indirectly exposed eyes. These longer-term studies elucidate the temporal progression of ocular impairment, and may help identify time-dependent diagnostic and treatment strategies for ocular trauma following blast exposure. In our study, a significant number of blast exposed animals developed lasting visual and anatomical defects. Each injury had its own unique temporal time course which is discussed in detail in the following subsections.

3.4.1 Decreased Contrast Sensitivity Was Immediate and Sustained

Contrast sensitivity deficits were immediate and did not improve over two months subsequent to blast exposure. The deficit only appeared in the blast exposed animals. The presence of delayed visual injury has been reported both clinically in blast exposed soldiers [22], [78] as well as by previous experimental studies [75]. However, the diminished visual function in animal studies has been commonly linked to posterior pole eye injuries in the retina, optic nerve, or TBI. In this study, we did not evaluate brain injury, optic nerve damage, or retinal function, so it is unknown what specifically caused the decreased contrast sensitivity. In a small subset of animals (n=9), we evaluated each eye independently and found worse contrast thresholds in the right eye (directly exposed) compared to the left. This suggests that the problem may be related to optic nerve or retinal damage rather than brain injury, which would likely cause bilateral vision deficits.

In our study, no major significant changes were found in retinal thickness. The central region of the blast exposed animals did appear to thicken relative to controls starting at week 1, although this thickening was only statistically significant at 7 weeks. Mohan et al. didn't find significant retinal thinning until three months postinjury [66], so it is possible that retinal thickness changes occur at later timepoints after blast. However, other researchers have reported retinal thinning and degeneration at 2 to 4 weeks after exposure to similar blast pressures [66], [76]. Difference in species, blast mechanism, and study design likely contribute to the conflicting results. Although we did not detect major signficant retinal changes via OCT, NfH levels were increased in blast exposed animals. NfH is released from degenerating retinal ganglion cells and axons into the vitreous [87]. The presence of elevated NfH indicates possible retinal damage that was not detected by OCT.

The lack of significant retinal OCT findings in our study may also be attributable to large variability between animals or impedance of corneal damage on image analysis. An increase in corneal opacity occurs during corneal swelling and likely decreased the effective resolution of the retinal OCT images. At some timepoints, we were unable to visualize the retina at all due to severe corneal damage (see Figure 3.9H). In these cases, retinal damage may have been present, but not captured by the OCT imaging. Further, the lack of definitive structural changes measured in OCT does not preclude functional changes. Future studies using this blast model could address this limitation by including ERG or VEP at each testing time point to assess retinal function in addition to structural changes. Corneal swelling could also contribute to the visual dysfunction seen in our study, but thickening in the cornea peaked at 3 to 5 weeks after blast exposure and does not completely explain

the immediate visual dysfunction. Further, decreases in contrast sensitivity were noted in animals without corneal swelling. The initial decrease in contrast sensitivity at the 1 day time point appeared to present in both the control and blast exposed animals. Some of this decrease may be due to the stress of the anesthesia procedure or residual effects of anesthesia. Additionally, some of the visual deficits occurring before corneal swelling may be attributed to corneal opacity which preceded the measurable swelling at later time points.

3.4.2 Corneal Swelling/Scarring Was Delayed and Temporally Complex

The temporal progression of corneal damage was an interesting finding in this study. The majority of corneal injuries reported in previous blast animal models have been short duration edema and abrasion. One exception to this is a single animal experiencing corneal scarring at 4 weeks after a 162.7 kPa blast in Hines-Beard et al. [20]. In our study, epithelial swelling occurred at 2 weeks, diminished and then experienced a resurgence of significant swelling at 6 weeks, linked to the stromal swelling during weeks 2 through 5. The delay between blast exposure and subsequent cornea swelling may be due to mechanical damage to the corneal endothelium, which allows increased uptake of water from the aqueous into the cornea. Corneal scarring always followed stromal swelling and was present by 8 weeks. Corneal thickness trended towards baseline values by the end of the study, but there was a remaining thickening of 10% (20 μm) in the stroma of both eyes suggesting some residual edema. This edema, coupled with the scarring, likely contributed to the poor overall visual ability in the animals at these later time points.

The majority of corneal injury was seen in the directly exposed eye, but both the directly and indirectly exposed eyes were damaged. At 1 week after blast, both eyes were thickened with respect to baseline by 57 μm. Only the indirectly exposed eye reached statistical significance due to the higher variance in the directly exposed eye. Potential sources for the increased variability could be slight changes in head angle, eyelid position, and head strap tightness. This variance hindered statistical power at the later time points due to the decreased sample sizes resulting from histological sacrifice.

Review of HE and TUNEL stained eyes revealed corneal epitheliopathy in blast exposed animals (Table 3.2). However, a significant number of control animals were flagged for corneal injury, despite no exposure to a blast wave. It is likely that the defects detected in our histology analysis were attributable to artifact or tissue processing, rather being caused by the blast insult. However, with the exception of one control animal, superficial scarring was found only in blast exposed eyes at 4 and 8 weeks after blast. This correlates

well with the timeline of corneal damage seen in OCT imaging. Similarly, neovascularization was only detected in blast exposed animals, and further confirms the activation of corneal inflammation and healing processes suggested by OCT.

The delay between initial blast exposure and subsequent corneal changes indicate that targeted drug treatment may be possible in the 2-week window before symptoms develop. Biomarkers associated with inflammation including LIX and IL-10 were elevated between 1 day and 4 weeks after blast exposure. The timing of these elevated concentrations suggests that these markers may be associated with the corneal swelling detected between 2-6 weeks. After the cytokine levels decreased, swelling likewise resolved, although scar tissue remained. LIX, in particular, has been previously associated with neutrophil infiltration to the stroma and keratitis [88]. Further investigation of the significantly elevated cytokines in blast exposed eyes may reveal the active inflammation pathways as targets for medical intervention.

Initial concerns that the corneal damage might be due to blast fragments of the Mylar membrane were assuaged by fluorescein staining immediately after blast which revealed no signs of abrasions. Thus, it is believed that the damage was truly caused by the blast pressure wave. A cross-sectional study performed by Cockerham et al. in 2014 found similar corneal injuries in blast exposed veterans. Specifically, 25% of nonpenetrative exposures resulted in anterior pole injuries and included stromal scarring [2]. The corneal damage in our model may be more prevalent due to the single mode of blast injury we are simulating. In combat, many soldiers experiencing comparable strength blast loading are also susceptible to other injury mechanisms. Penetrating injuries from shrapnel and flying debris injuries, in particular, may mask some of the effects of pure primary blast on the cornea. Further, protective eyewear may reduce the prevalence of corneal scarring in the clinical population.

3.4.3 IOP Rapidly Increased to Applied Overpressure

Understanding IOP both during and after blast is critical to understanding injury mechanisms. Measurements of *in vivo* IOP during blast exposure revealed that internal ophthalmic pressures were orders of magnitude above normal physiologic levels. This large increase was only for 6 ms. IOP was not tracked longitudinally over the 8 week duration of our study; however, other studies have shown significant transient increases in IOP by 35% in the first 24 h after blast, followed by a significant chronic decrease in IOP [20], [56].

Internal ophthalmic pressures in directly exposed eyes closely matched external tube measurements. Therefore, tube pressure measured 2 cm before the animal is a suitable

surrogate for IOP in directly exposed eyes. Tube pressure may not be a good surrogate for IOP in indirectly exposed eyes, as the tube pressure was higher than in the indirectly exposed eye, although this difference was not significant. IOP in both eyes were orders of magnitude above normal physiologic levels. Decreases in peak pressure and pressurization rate observed in the indirectly exposed eye help account for the lower incidence of long-term stromal swelling and scarring found in left eyes. These data highlight the important role of facial structures and blast wave direction in determining risk of ocular trauma from blast.

3.4.4 Translation of Rodent Eye Findings to Humans

A comparison of the blast parameters found in several types of improvised explosive devices was generated from explosive magnitudes from the National Ground Intelligence Center [89] and equations from Alonso et al. [58], and is shown in Figure 3.13. According to those sources, the pressure and duration used in this study were estimated to be similar to a compact car bomb at a stand-off distance of 15-20 m.

For mortality curves, the work of Bowen in 1968 proposed scaling based on animal mass [6]. However, this scaling was derived from 50% mortality curves, which are largely

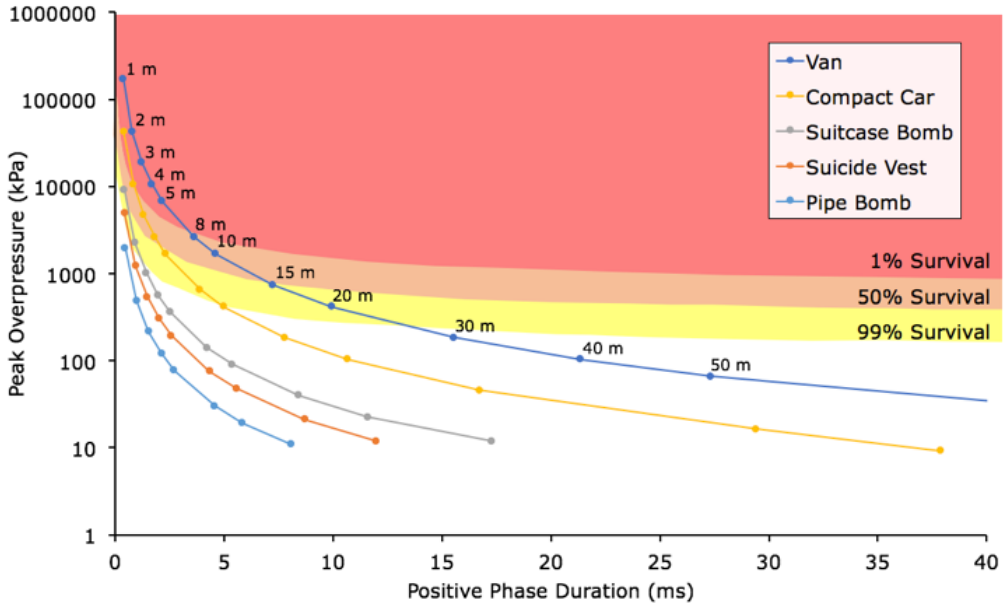

Figure 3.13: Chart of peak overpressure and positive phase durations for a range of explosive sources (individual lines) at different standoff distances (dots) calculated based on explosive magnitudes from the U.S. Army National Ground Intelligence Center [89] and shockwave equations from Alonso et al. [58]. The present study had an average ±SD blast overpressure and duration of 228±28 kPa and 7.1±0.6 ms, respectively.

driven by lung injury mechanics. It is not clear whether the same scaling parameters can be expanded for use in ocular or other injury modes. Therefore, the blast levels used in the majority of experimental models have been based on phenomenological injury findings from preliminary studies. More research remains to be done to truly correlate blast loading so that findings between experimental models can be accurately determined.

There are several distinctions between rat and human eyes that are important to consider when extrapolating findings in this study to a human population. First, rat eyes are laterally placed [90], so most experimental studies can investigate directly and indirectly exposed eyes. Front-on blasts in humans are likely to generate some gradient between directly and indirectly exposed eyes due to the central facial structures. Second, the globe diameter, retinal thickness, and corneal thickness of the rat eye is roughly 20-40% of the human eye [91], [92]. No methodology for scaling currently exists, so it is unclear how experimental blast pressure magnitudes and durations relate to military blast exposures. Third, the cornea makes up a much larger portion of the globe of the eye in the rat compared to the human. This may result in greater relative deformations of the cornea following blast exposure. Finally, the rat lens takes up proportionally greater space than the human lens. The lens is significantly stiffer than all other ocular components, so this difference may have important ramifications on the dynamic response of the eye to blast loading. Despite these distinctions, we chose rats for the development of our ocular blast model because of the availability of established methods for characterizing visual ability, the feasibility of longer-term studies, and the ability to compare findings with other studies in the literature. Computational modeling of the rodent and human eyes in blast may provide further insight into potential implications of species related differences to loading.

3.5 Conclusion

Rat contrast sensitivity significantly decreased immediately following blast exposure, and persisted for at least 8 weeks. Severe, delayed corneal damage may account for some of this visual deficit, but other mechanisms such as retinal functional damage or TBI must be responsible for the immediate visual dysfunction. Although retinal thickness changes were not detected via OCT in the 8 weeks after blast, elevated NfH levels in blast-exposed animals indicated degeneration of the retinal ganglion cell layer. The unique 2-week time delay of corneal swelling suggests a possible treatment window to mitigate corneal swelling and scarring after blast exposure, and potentially improve long-term visual outcomes.

CHAPTER 4

STRESSES AND STRAINS ON THE EYE DURING BLAST EXPOSURE

4.1 Introduction

There are many advantages in using computer modeling to enhance experimental blast models. First, experimental models of blast ocular injury are typically *in vivo* studies, which ethically should only be performed when the data cannot be obtained by other experimental or analytical methods. When appropriate, the use of computer models may "replace" or "reduce" animal experimentation [93]. Second, modeling allows comprehensive extraction of data that would be difficult or impossible to gather experimentally. Prominent examples are tissue stress and strain measurements, which are challenging to capture *in vivo* during blast. These measurements can be easily approximated at any location or timepoint from computational models. A third advantage to using computer models in blast research is in being able to quickly and independently evaluate effects due to differing model parameters, such as loading conditions, geometry, and material coefficients. These comparative studies can be useful in determining important factors without having to run full experimental studies.

For example, a common concern in animal models of blast injury has been how to translate the varied blast loading conditions experienced by humans into corresponding loading for experimental models. Animal models for blast research typically include mice, rats, or rabbits, all of which feature both a smaller body and eyes than blast-exposed soldiers. Additionally, each animal model has dissimilar ocular anatomy, which will likely alter ocular mechanics and therefore injury predictions. Finite element (FE) analysis can be used to compare the effect of anatomical features and globe size on predictions of stress and strain during blast. These parametric simulations can provide insight into how differences between rat and human ocular anatomy relate to injury outcomes.

Numerous studies have used FE modeling to investigate the effects of blast to the ocular system [94]. Studies interested in evaluating how the blast waves interact with facial

features to amplify the blast loading on the eye typically include detailed facial geometry and represent the surrounding environment using Eulerian techniques to simulate the pressure propagation wave and interactions (see Figure 4.1A). Rossi et al. investigated blast loading from a variety of approach angles to a whole head model [21]. From their simulations, perpendicular, or face-on, loading conditions resulted in the highest load being applied to the eye. Further studies with the same model by Esposito et al. examined retinal deformation under blast loading [18]. The orbit of the eye acted to reflect and intensify the pressure in the eye. Additionally, reflections caused subsequent compression and traction at the vitreoretinal interface, which would increase risk of retinal detachment (see Figure 4.1B). Further, the authors found that the pressure in the eye was more dependent on the peak overpressure, rather than the positive duration, of the applied load.

Bhardwaj et al. also used a coupled Eulerian-Lagrangian model to understand the effect of facial structures on pressure loading at the eye [16]. This model simulated a 2.5 kg TNT explosion sourced from either straight on or from the ground. The findings of Rossi et al. and Esposito et al. were replicated, with the highest pressure load on the eye developed from straight on blast loading. Additionally, the nose, brow, and cheekbones acted to focus pressure into the eye and orbit (see Figure 4.2). IOP measured in the eye was periodic in nature, similar to the previous model. The authors predicted risk of damage to extraocular tissues due to globe distortion and to the optic nerve head due to elevated IOP in the posterior eye. However, the IOP developed from blast was not sufficient to cause globe rupture. FE modeling studies by Liu et al. have confirmed globe rupture is not predicted by moderate primary blast loading [95].

Bailoor et al. added protective goggles and spectacles to the model previously developed by Bhardwaj et al. [17]. This model found both types of protective eyewear reduced the peak overpressure transmitted to the eye from blast by 3-20%, with higher protection efficiencies resulting from higher loads. However, both protections concurrently increased the duration of elevated pressure on the eye.

The studies mentioned here agree that the eye is naturally vulnerable to blast loading due to the focusing effect of facial features increasing blast pressure from frontal blast exposure. However, one limitation shared by these models is the difficulty in validating them. Due to the high-speed nature of blast incidents and the confined space of the eye, ocular tissue measurements are incredibly challenging to capture during actual blast events. This lack of available validation data has led previous FE models to be validated with IOP and corneal deformation data from blunt impact. To date, this has been the most accurate

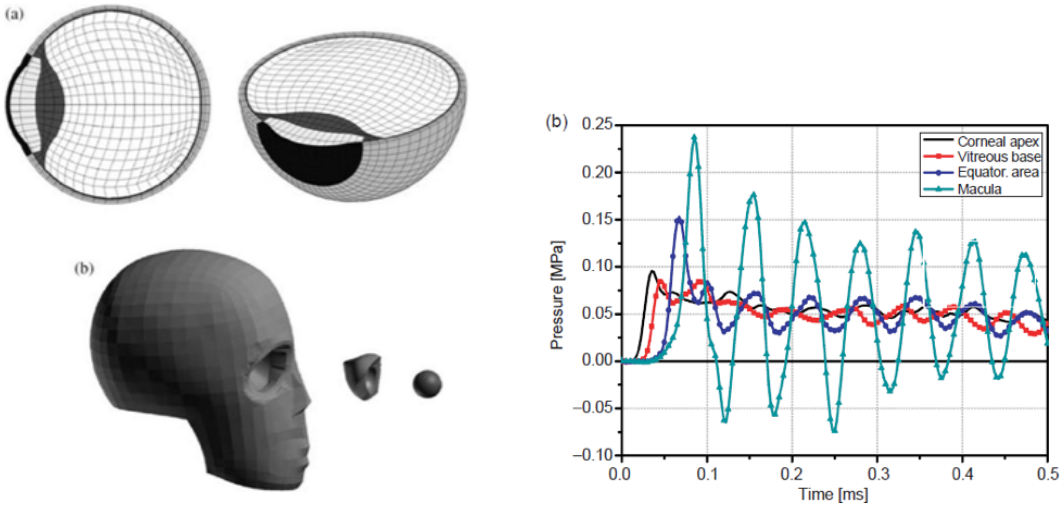

(A) (B)

Figure 4.1: FE model of Rossi and Esposito. (A) Modeled geometry and (B) pressure findings. Model predicted negative pressure at retina. Reproduced with permission from [18], courtesy of www.tandfonline.com.

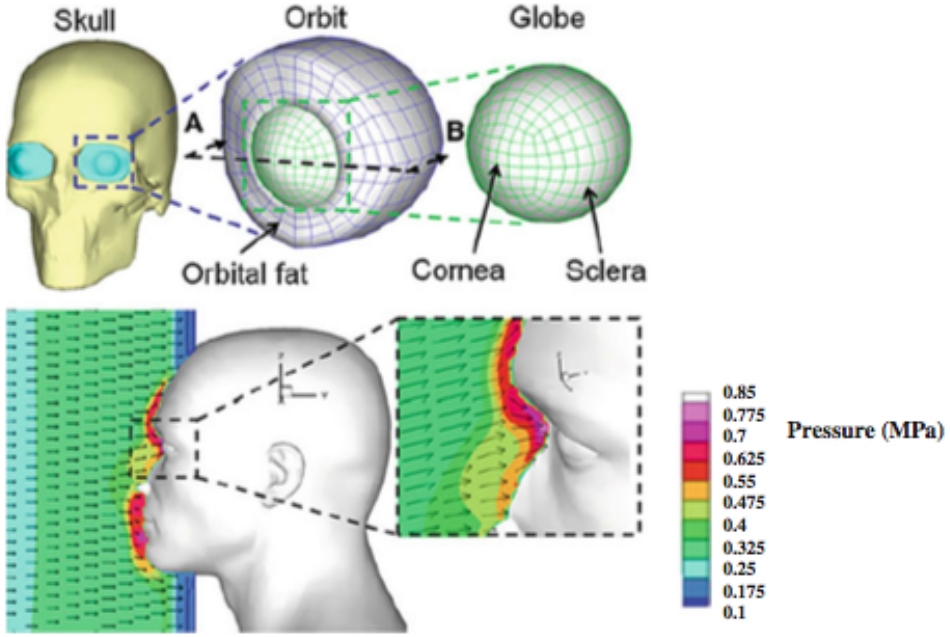

Figure 4.2: Skull and eye model of Bhardwaj et al. Blast overpressure was clearly focused and amplified into the eye by the facial features. Reproduced with permission from [16].

validation available, but it is unlikely this validation is truly sufficient for confidence of model predictions under blast loading.

The objectives of this computational study were to (1) develop a validated model of ocular blast loading; and to (2) investigate how differences between experimental models and loading conditions impact mechanics of the eye. To achieve this, experimental IOP measurements taken during blast (section 3.2.6) were used to validate a rat eye FE model. A parametric study was performed that varied ocular geometries, thereby representing the differences between human and rat eyes. Particular attention was given to how the relatively large cornea and lens of the rat eye change ocular behavior under blast loading. A second parametric study was run that altered blast loading conditions. The results of these parametric studies were used to develop a scaling equation to better understand how to create blast pressures in animal models that are equivalent to human exposures. Outcomes from this study will be useful for ocular blast trauma research community to connect studies using different animal models, blast loading parameters, and to the broader implications of soldiers suffering from primary ocular blast injury.

4.2 Methods

4.2.1 Model Geometry

The model geometry featured four main components: cornea, retina, lens, and vitreous. These components were chosen to represent the dominant anatomical contributors to the mechanical response of the eye, and locations of injury seen in the experimental work described in Chapter 3. Notable exclusions from the model were the optic nerve, extraocular tissues and bony orbit. The optic nerve and extraocular tissues would be mechanically important if the eye moves during the exposure; however, this simulation was focused on injuries due to primary blast exposure only, and not those caused by inertial energies or momentum of the eye. Extraocular muscles have been previously shown to have negligible effects during rapid blunt trauma [96], and were omitted from the model. Orbital geometry has been shown to focus the shock wave into the eye, acting to increase blast severity [16]. Omission of the bony orbit likely reduced the magnitudes of stress and strain, but is assumed to not affect comparisons between loading conditions or geometries.

Rat eye geometry dimensions were based on literature values [91], [92] and verified against thickness measurements from OCT and microscopy done in lab. The exact ocular dimensions used in the model are shown in Table 4.1. From these dimensions, a quarter-symmetry geometry was created to substantially reduced processing time (see Figure 4.3).

This model simplification required the boundary conditions and loads to be symmetric, limiting the ability to evaluate the effect of incidence angle on ocular stress and strain. To match experiment data in Chapter 3, side-on blast was the only loading condition simulated.

4.2.2 Material Properties

In previous ocular blast models, the lens has been represented as either a rigid solid [97], [98] or linear elastic material [99], [100]. Lens deformation was a desired output of the model, so a linear elastic material was selected. All materials in the model were isotropic. The vitreous was modeled as nearly incompressible with a bulk modulus as of 2.272 GPa, which was similarly used by Bhardwaj et al. [16].

Cornea was modeled as a hyperelastic solid. Constitutive models including Mooney-Rivlin, Ogden, and neo-Hookean were used to fit cornea tensile data from Uchio et al. [98]. Material models were evaluated for stability and goodness of fit using the ABAQUS Material Evaluator. A third-order Ogden model was chosen to best represent the hyperelastic characteristics of the cornea material (see Figure 4.4A).

The sclera was modeled as a hyper-viscoelastic material. Hyperelasticity was modeled using a first-order Ogden material model using the model evaluation procedure as previously described, based on sclera tensile data from Uchio et al. [98] (see Figure 4.4B). Viscoelasticity was included using a Prony-series approximation fit from relaxation data previously measured in lab. The material coefficients used for all materials in the model are summarized in Tables 4.2 and 4.3.

4.2.3 Mesh

The vitreous and lens of the eye were meshed with linear hexahedral elements with distortion control and enhanced hourglass control (C3D8R). The majority of the cornea and sclera were similarly meshed, with the exception of the border regions, which were partitioned and meshed using linear tetrahedral elements with distortion control (C3D4). The use of tetrahedral elements was necessary in these regions due to the regional geometry.

The number of elements varied slightly based on each variation of animal geometry. The number of elements for the base rat eye geometry is shown in Table 4.4. The worst aspect ratios listed in the table are the worst from any of the model variations.

A mesh convergence study was performed on the initial rat geometry model. Peak IOP from Chapter 3 was used as the convergence criterion by extracting IOP from the model at the sensor location. The peak IOP was used for the validation due to the close match between tube pressure and peak IOP. The lens was converged first, followed by the

Table 4.1: Dimensions (mm) of rat eye components. Thicknesses listed are anterior thickness for the cornea and posterior thickness for the sclera. Vitreous thickness listed as anterior thickness, posterior thickness.

Component	Axial Diameter	Transverse Diameter	Thickness
Cornea	6.26	6.08	0.16
Sclera	6.26	6.08	0.34
Lens	3.74	3.96	–
Vitreous	5.76	5.56	0.93, 1.08

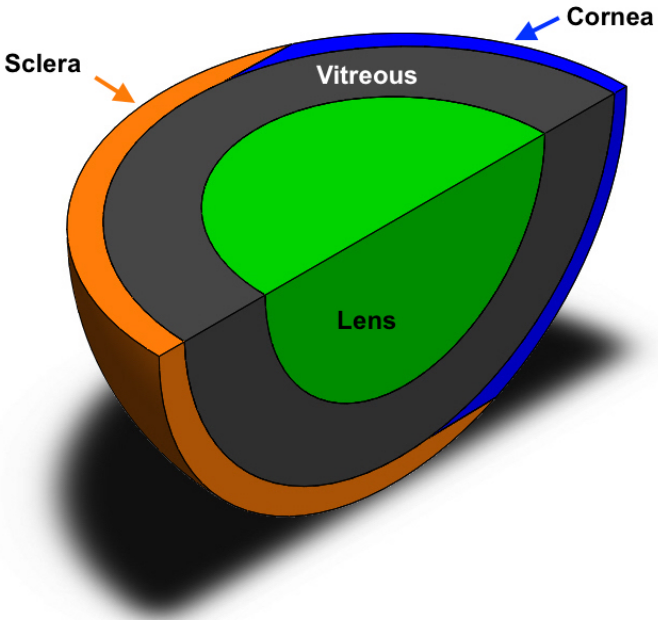

Figure 4.3: Quarter-symmetry 3D rat eye geometry.

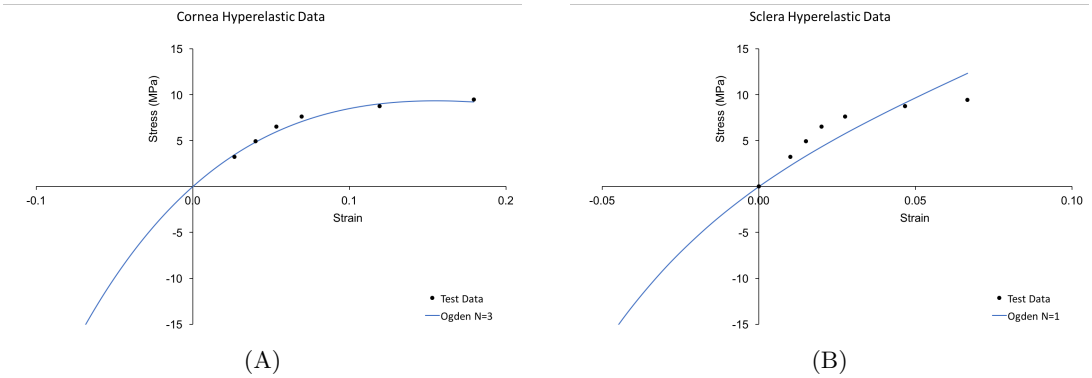

(A) (B)

Figure 4.4: Model fit for cornea and sclera hyperelasticity. Potential models were evaluated for stability and fit to test data. (A) For the cornea, a third-order Ogden model provided the best fit with stability. (B) The sclera was fit with a first-order Ogden model.

Table 4.2: Summary of material properties used in the eye model.

Model Component	Constitutive Model	Poisson's Ratio	Density (kg/m^3)	Reference
Cornea	Hyperelastic 3rd-order Ogden	0.42	1076	[98]
Lens	Isotropic, Linear Elastic, E=5 MPa	0.48	1200	[99], [100]
Vitreous	Isotropic, Bulk Modulus K=2.272 GPa	0.4999	1006	[16]
Sclera	Hyperelastic 1st-order Ogden Viscoelastic Prony-series	0.47	1243	[98]

Table 4.3: Material coefficients for hyperelastic and viscoelastic models.

Cornea: Ogden n=3

i	$\mu_i * 10^6$	α_i	$K_i * 10^{-9}$
1	-331.1	2	1076
2	101.6	4	0
3	280.0	-2	0

Sclera: Ogden n=1

i	$\mu_i * 10^6$	α_i	$K_i * 10^{-9}$
1	80.3	-17.6	1.52

Sclera: Prony Series

i	G_i	K_i	τ_i
1	-0.135	0	0.099
2	0.318	0	2.077
3	0.241	0	17.60
4	0.222	0	247.2

Table 4.4: Number of elements and aspect ratios for each ocular component in baseline rat model. There were 47,417 elements in the entire model.

Part (Element Type)	Elements	Average Aspect Ratio	Worst Aspect Ratio
Cornea (Hex)	1692	1.87	5.61
Cornea (Tet)	1101	2.09	6.08
Vitreous (Hex)	27720	3.74	22.48
Lens (Hex)	1835	1.85	3.79
Sclera (Hex)	11296	1.83	13.82
Sclera (Tet)	3773	1.64	2.58

vitreous, and finally the cornea and sclera. This order of convergence was chosen so the external surface interacting with the loading blast wave would be converged last.

4.2.4 Loads and Boundary Conditions

ConWEP is a tool originally developed by the U.S. Army Corps of Engineers to implement accurate open field air blast pressure loading without directly modeling pressure wave propagation through air. The ConWEP interaction panel allows specification of pressure loading on a specified surface. Using the ConWEP tool, a planar pressure wave interaction was created as a tabulated pressure-time history and was applied to the outer surface of the eye.

The pressure-time history used to define the wave was taken from a single shock tube recording from the Chapter 3 IOP studies, and was representative of the loading conditions applied in all the animal experimental studies. Use of a blast load from the IOP studies allowed model validation with the corresponding IOP trace recorded in the right eye (directly exposed) of that study. The pressure profile applied to the model had a peak overpressure of 244.5 kPa and positive phase duration of 8.2 ms (see Figure 4.5).

The posterior surface of the eye was fixed in all linear and rotational degrees of freedom. This boundary condition was assigned to the rear region defined by 20% of the diameter of the globe. To apply quarter symmetry to the model, additional boundary conditions were applied to the xz and yz faces: y-symmetry and x-symmetry, respectively. These symmetry boundary conditions set the symmetry directions degrees of freedom to zero.

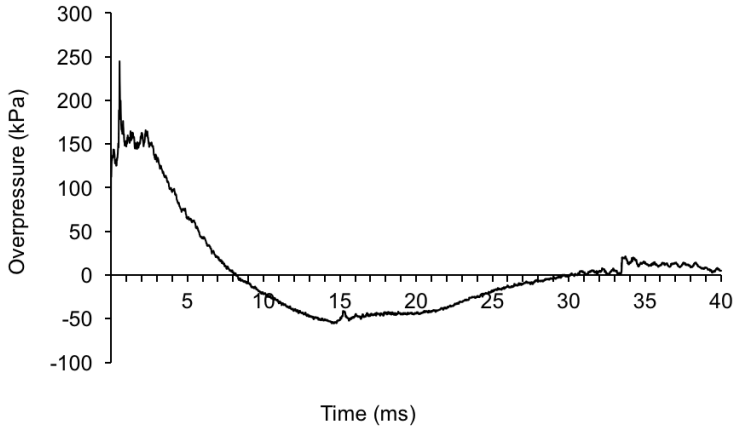

Figure 4.5: Baseline pressure load applied to eye models. Pressure trace was recorded from IOP studies to allow validation against IOP results.

4.2.5 Study Design

The primary goal of this study was to understand the impact of varied ocular size, geometry of anatomical features, and loading conditions on model predictions of IOP, stress, and strain in the ocular tissues. Initial studies simulated the full blast wave interaction, with durations up to 50 ms. The highest magnitude of stress and strain in the eye occurred during the initial 1-2 ms of the simulation, so all subsequent studies simulated only the first 3 ms of the wave interaction. The shorter simulation time decreased computational time by a factor of 10.

4.2.5.1 Scaled Geometries

The three major differences between rodent and human ocular anatomy are the globe diameter, cornea size, and lens size (see Figure 4.6). The diameter of the human eye is 3.9 times that of the rat eye, which corresponds to a 15 times difference in surface area and a 58 times difference in volume. The cornea of the rat comprises nearly half of the corneoscleral outer shell of the eye, while the human cornea is a smaller segment. Finally, the spherical lens fills the majority of the rat eye, with only a small space remaining for vitreous and aqueous. In a human eye, the vitreous fills the majority of the space inside the eye, with the biconvex lens comprising a smaller relative space. Due to the large difference in material properties between the mostly liquid vitreous and relatively stiff lens, the proportion of the eye filled with each substance could drastically change ocular behavior.

In order to understand the differences between a rat and a human eye, a total of six geometries were evaluated in the model that varied the sizes of the globe, cornea, and lens

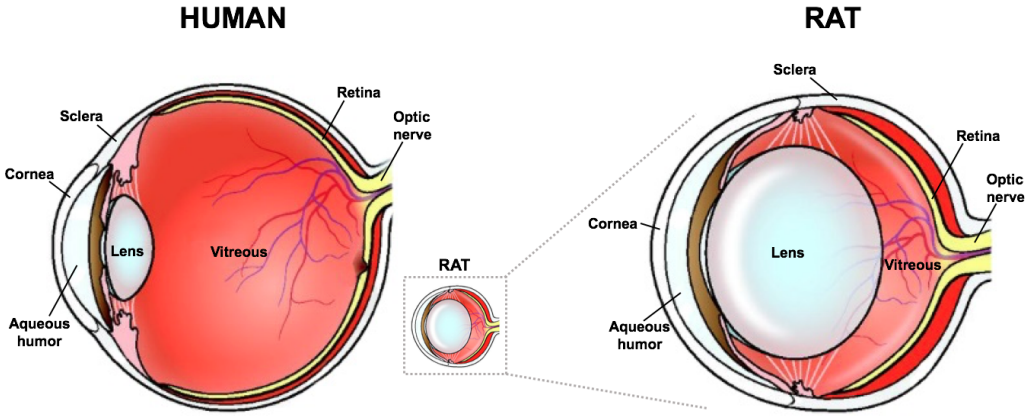

Figure 4.6: Comparison of human and rat ocular geometries. Key differences are globe diameter, lens size, and cornea size. Adapted from Veleri et al. [52].

in relation to each other. The geometries included combinations of rat- and human-sized globes, with varying sizes of the cornea and lens. Therefore, a span of geometries ranging from the rat eye to the human eye could be compared. Descriptions of each geometry can be found in Table 4.5, with an image of each model in Figure 4.7.

To focus the study on the geometric variation between human and rodent anatomy, no variation in material properties was included. All material properties were held constant at the values described above in Section 4.2.2.

4.2.5.2 Scaled Loads

The second parametric study evaluated the effects of blast magnitude and duration on the eye. A total of five different blast pressure profiles were applied to each of the six model geometries. These pressure profiles were generated by scaling the initial blast wave by ± two standard deviations for each its pressure magnitude (see Figure 4.8A) and positive phase duration (see Figure 4.8B). Essentially, the base pressure-time curve was stretched in either the x- or y- axis. Standard deviations were derived from experimental data in Chapter 3. The scaled loads had overpressures ranging from 180 - 280 kPa and positive phase durations of 6 - 10 ms.

4.2.6 Data Analysis

Peak and average IOP at the sensor location, peak lens displacement and strain, and peak corneal displacement, strain, and stress were extracted from all simulations. All strain measures were reported as maximum principal strain. Stress measured in the cornea was the von Mises stress. Peak lens displacement and strain were measured using an element set of seven elements centered around the midline of the lens. Cornea strain and stress were extracted from a ring of elements on the exterior surface of the cornea, while corneal deformation was extracted as the peak deformation across the entire cornea. Peak and average IOP were calculated from nine elements chosen at a location in the vitreous that was replicative of the pressure transducer placement in animal experiments from Chapter 3.

Peak and average data for all 30 simulations (6 geometry models * 5 pressure profiles) were exported to JMP (SAS Institute, Cary, NC) for statistical analysis. The results of each simulation were analyzed to determine the effect of each parameter (globe size, lens size, cornea/sclera ratio, overpressure, and duration) on model outputs using multiple regression. Four key assumptions of valid multiple regression were considered: linearity, reliability, homoscedasticity, and normality.

Table 4.5: Ocular Geometries for Parametric Study

Model Name	Globe Size	Cornea/Sclera Ratio	Lens Shape
Rat	Rat	Rat	Rat
Small Cornea	Rat	Human	Rat
Small Lens	Rat	Rat	Human
Small Human	Rat	Human	Human
Large Rat	Human	Rat	Rat
Human	Human	Human	Human

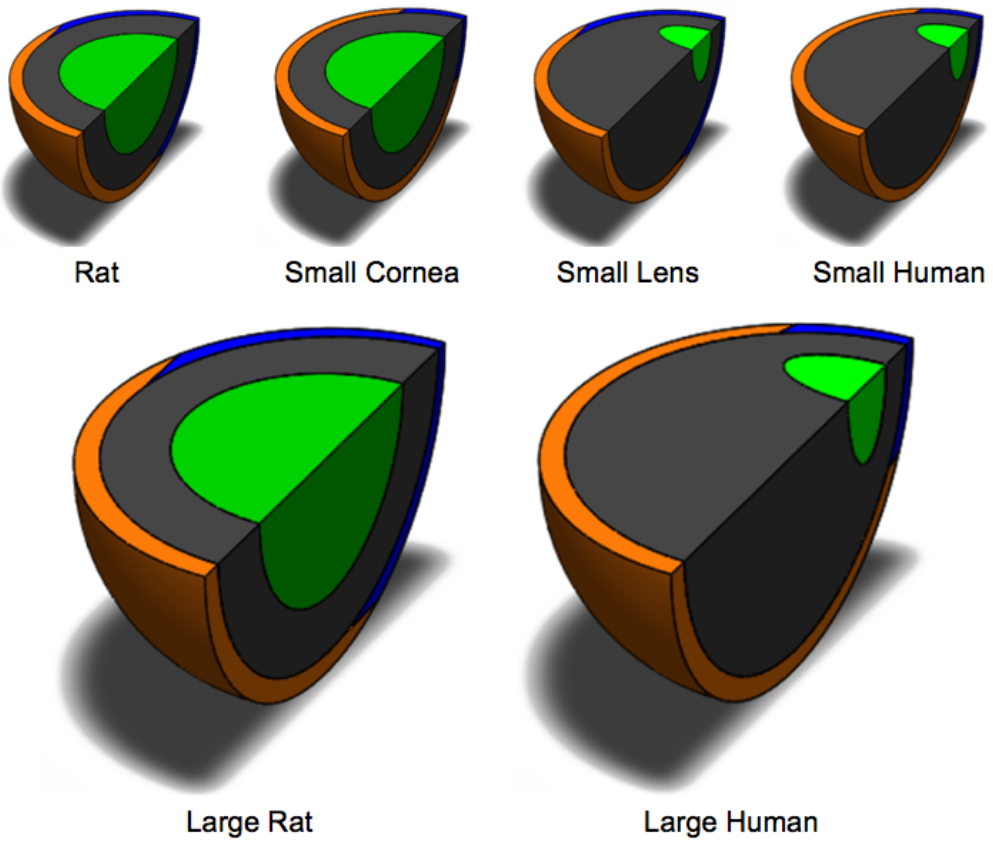

Figure 4.7: Six varied model geometries for blast loading simulations.

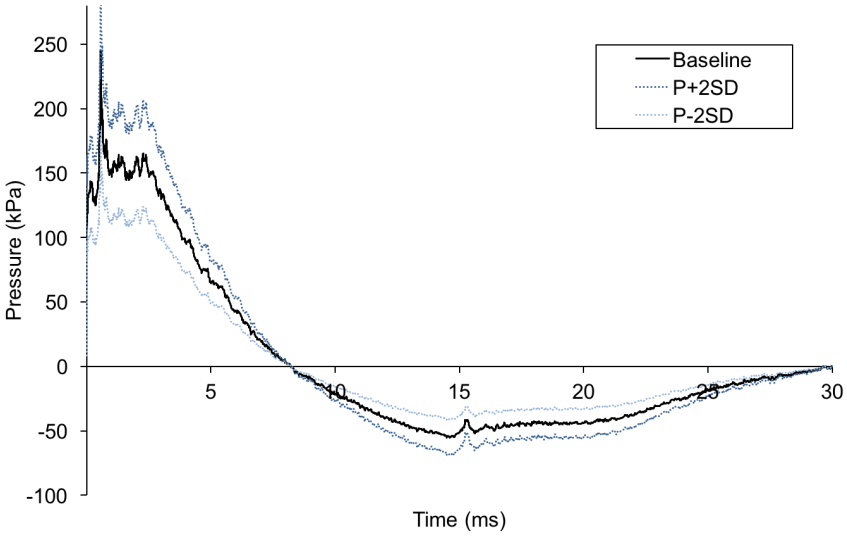

(A)

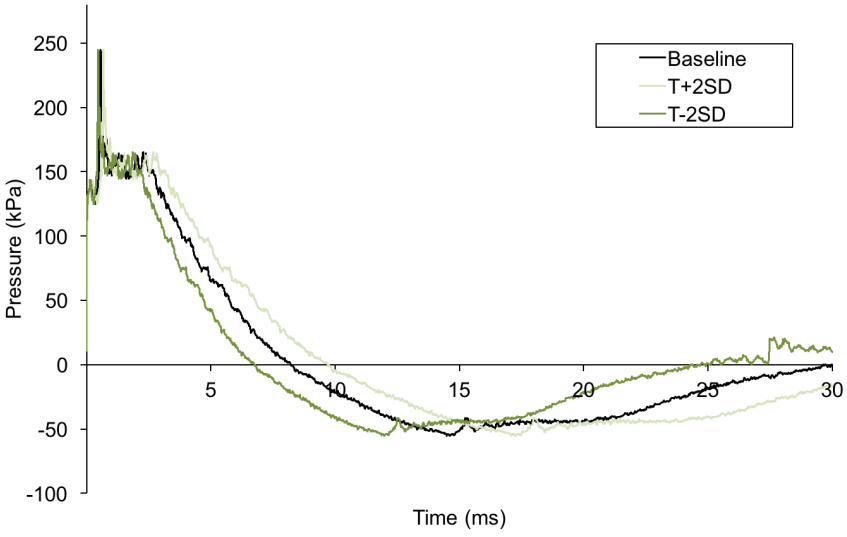

(B)

Figure 4.8: Five loads were applied to all six modeled geometries. (A) Overpressure was scaled by ±2SD from baseline; (B) Duration was scaled by ±2SD. Standard deviations were calculated based on all experimental blast exposures and applied to scale single loading curve from IOP study.

4.2.7 Scaling Equation

A scaling equation was developed such that blast parameters and resulting IOP can be compared for different animal models. The initial proposed equation (see Equation 4.1) used two input parameters: applied blast pressure, P (Pa), and globe axial length, d (mm). These two parameters were chosen due to the fact that they were found to have the largest impact on the overpressure in the eye over the first 3 ms of blast. Model constants, a and b, were solved for using model output data from 12 simulations varying geometry (rat, large rat, human, and small human) and overpressure (baseline ±2SD).

$$IOP = aPd^b \tag{4.1}$$

4.3 Results

4.3.1 Model Convergence

The lens IOP and strain were converged first, using varying lens mesh densities between 161 and 8544 elements (see Figure 4.9). The lens converged at 1000 elements. The vitreous mesh was converged using IOP and corneal displacement from vitreous mesh densities of 750 to 250,000 elements. Convergence was achieved above 18,000 elements as shown below in Figure 4.10. Finally, the cornea and sclera were meshed and converged together to ensure mesh continuity at the corneoscleral boundary. Convergence was assessed using IOP and corneal displacement (see Figure 4.11). Convergence was achieved above 10,000 elements.

The final mesh densities of the model were 1835, 27,720, and 17,862 elements for the lens, vitreous, and cornea/sclera, respectively. For each of the model components, the final meshes were at least 50% more elements than the minimum determined by the convergence study. The mesh density was increased to improve the mesh quality. The round surfaces of the eye were difficult to mesh with hexahedral elements without poor aspect ratios. Increasing the mesh density decreased the number of elements with poor aspect ratios as well as the maximum element aspect ratio. Further, coarse meshes exhibited moderate contact failure at the vitreous border, which were also addressed by increased mesh density.

After model convergence, the predicted IOP at the sensor location (285 kPa) was within 8.7% of the experimental data recorded from Chapter 3 (262.1 kPa). Given the noise in the unfiltered experimental data and the uncertainty of the IOP sensor position within the vitreous, this was considered a successful validation of the model. It is important to note that the peak IOP was the only model parameter with available data to validate against. Other model outputs were not validated, and cannot be directly applied to predict failure

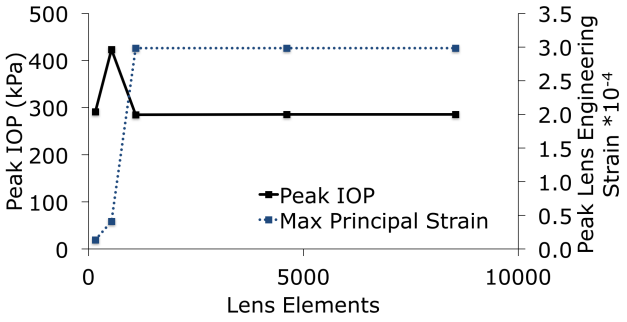

Figure 4.9: Convergence of IOP and lens strain based on lens mesh density. Both metrics converged with roughly 1000 lens elements, with 1835 lens elements used in subsequent studies.

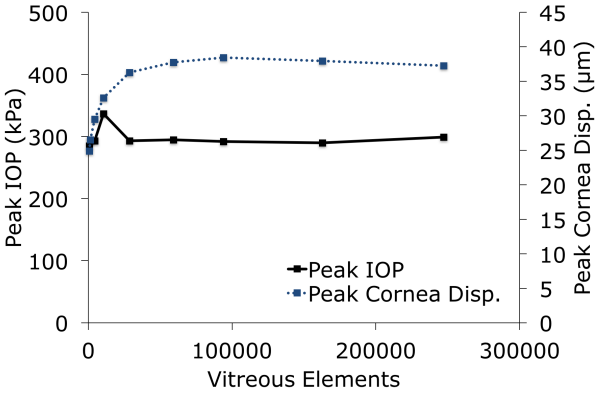

Figure 4.10: Convergence of IOP and cornea displacement based on vitreous mesh density. Both metrics converged at 18,000 elements. Future studies used 27,720 hexahedral elements in the vitreous.

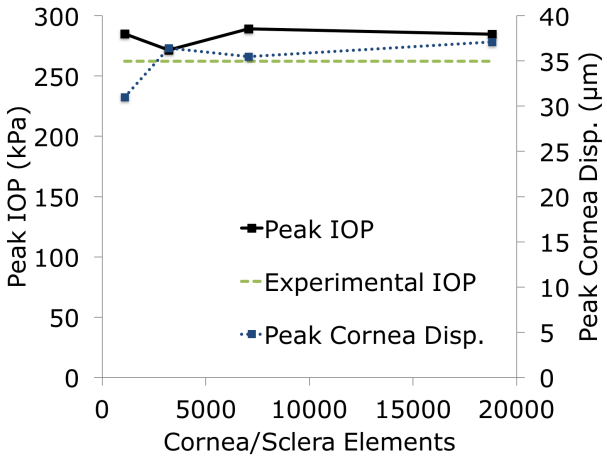

Figure 4.11: Convergence of IOP and cornea displacement based on cornea and sclera mesh density. Both metrics converged above 7000 elements. Future studies used 17,862 elements between the sclera and cornea

or injury. Additionally, the validation was only performed using the peak IOP rather than the instantaneous IOP due to signal artifacts (reflections, probe movement) after the initial IOP peak.

4.3.2 General Observations

The initial tissue deformation as the shock wave passed through the eye could be seen over the first 200 μs of the simulation (see Figure 4.12). The timing of the peak values for all extracted data was strongly linked to the arrival time of the peak overpressure at roughly 1.63 ms. All model geometries and blast loading resulted in compression of the globe in the axial direction. The extent of this compression could be measured by the central corneal deformation (see Figure 4.13).

Review of the assumptions of multiple regression showed that the linearity, reliability, and homoscedasticity conditions were met by the data. However, one assumption that may have been violated was the normal distribution of data. While the model outputs did meet the normality condition, distributions of independent variables were not normal, as they were prescribed at set levels. This could be addressed in later simulation by adding more variation in factor levels to approximate normal distributions.

4.3.3 Scaled Geometries

Globe size significantly impacted every model output with the exception of peak IOP (Table 4.6). Averaged IOP was most sensitive to globe size ($p = 0.011$) and lens size ($p<0.0001$), but was also impacted by cornea size ($p = 0.02$). Cornea stress and strain were significantly sensitive to the globe size and cornea size ($p<0.05$), with corneal displacement sensitive to the globe size ($p<0.0001$), but below the threshold for significance from cornea size ($p = 0.0535$). Lens strain was significantly related to globe, lens, and cornea size, while lens displacement was only sensitive to globe and lens size ($p<0.0001$).

4.3.4 Scaled Loads

Increases in peak overpressure significantly increased peak IOP ($p<0.0001$) and average IOP ($p<0.0001$, see Figure 4.14). The magnitude of pressure loading significantly affected every model output (Table 4.7). Positive phase duration did not significantly affect any of the listed parameters ($p>0.35$). Peak IOP, average IOP, cornea strain, and cornea stress were most strongly correlated with blast pressure ($p<0.0001$).

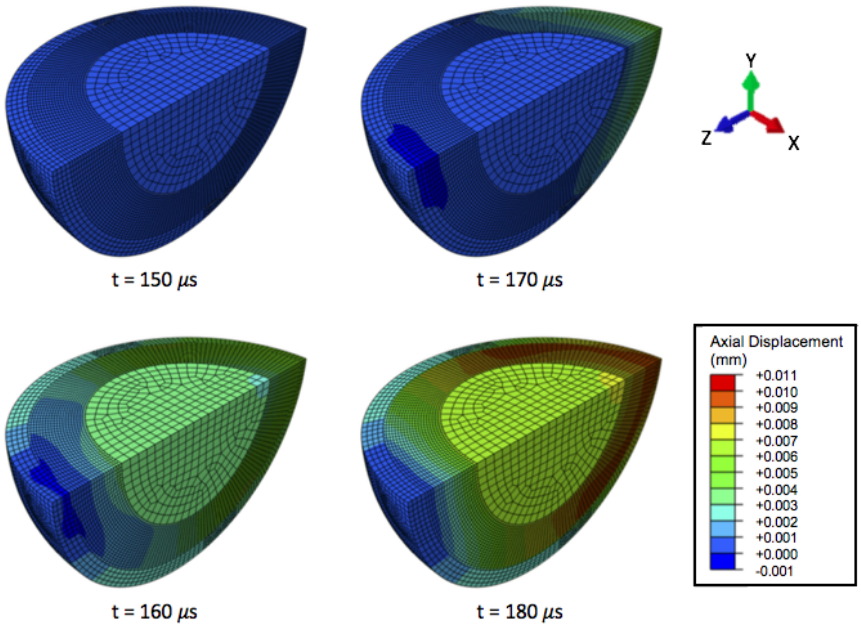

Figure 4.12: Axial displacement (z-axis) during initial pressure wave interaction with the eye.

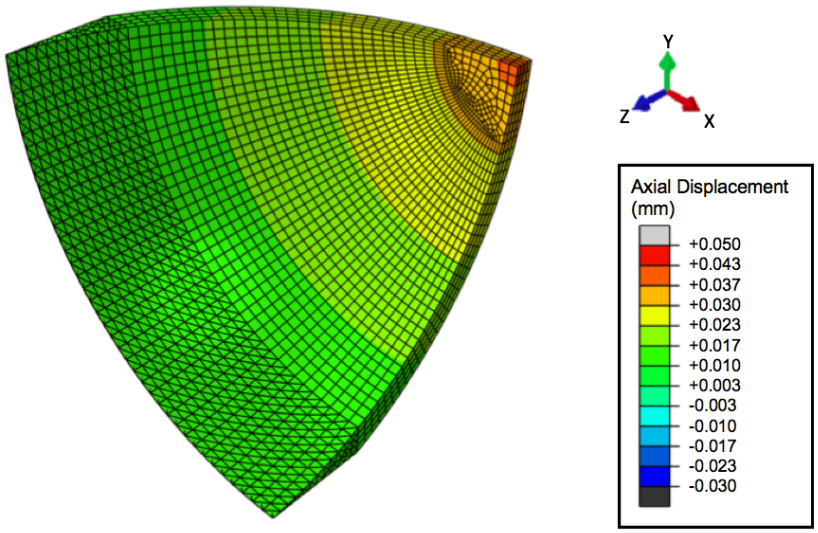

Figure 4.13: Deflection of cornea in anterior-posterior axis (z-axis). Peak deflection was located in central region.

Table 4.6: Statistical significance of model output response to geometry parameters.

Model Output	**Globe Size** p-value	**Lens Size** p-value	**Cornea Size** p-value
Peak IOP	0.6412	0.3105	**0.0018**
Avg IOP	**0.0107**	**<0.0001**	**0.0200**
Cornea Strain	**0.0047**	0.1157	**0.0051**
Cornea Stress	**0.0076**	0.1264	**0.0046**
Cornea Disp.	**<0.0001**	0.1930	0.0535
Lens Strain	**<0.0001**	**<0.0001**	**0.0217**
Lens Disp.	**<0.0001**	**<0.0001**	0.5431

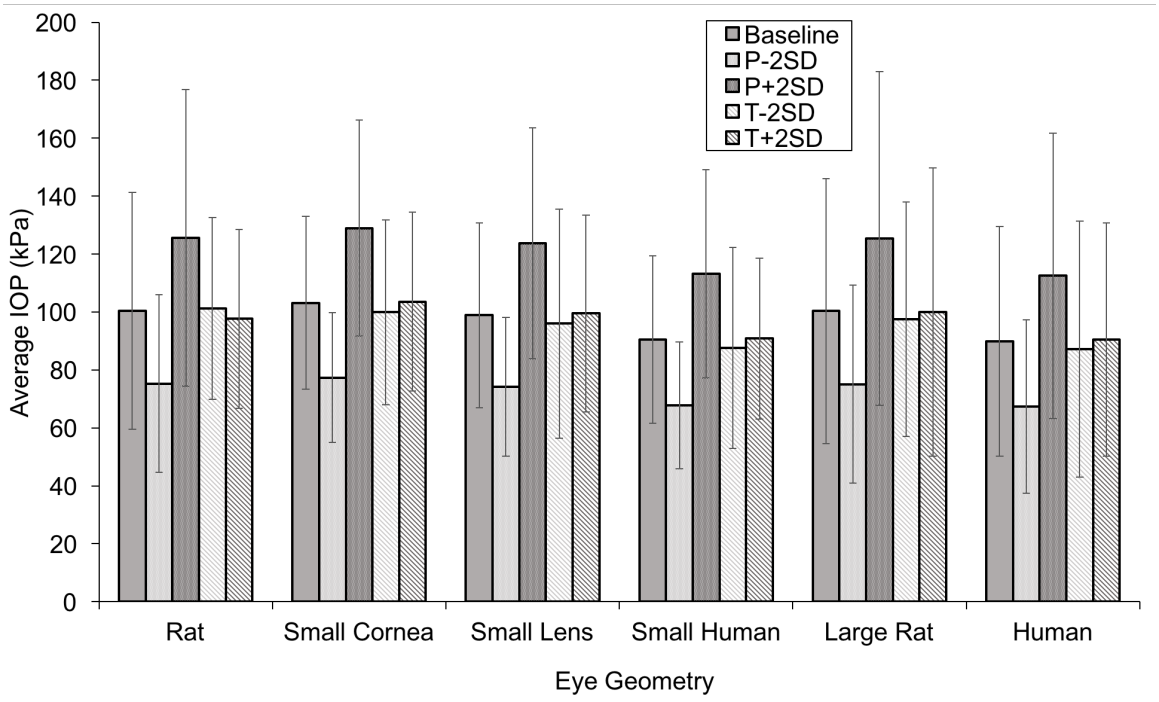

Figure 4.14: Average IOP for each of the six modeled geometries. IOP averaged across nine elements in the posterior vitreous for the initial 3 ms of blast exposure. Error bars indicate standard deviation across those same elements.

Table 4.7: Statistical significance of model output response to input blast overpressure and duration.

Model Output	**Pressure** p-value	**Duration** p-value
Peak IOP	**<0.0001**	0.5088
Avg. IOP	**<0.0001**	0.3529
Cornea Strain	**<0.0001**	0.8225
Cornea Stress	**<0.0001**	0.7658
Cornea Disp.	**0.0132**	0.7670
Lens Strain	**0.0459**	0.5071
Lens Disp.	**0.0033**	0.8352

4.3.5 Scaling Equation

From the initial IOP prediction equation (see Equation 4.1), IOP data were fit to applied blast pressure and globe axial length data. Model constants, a and b, were optimized to minimize error, and were found to be 1.02, and -0.0779, respectively. However, the two degrees of freedom formulation predicted IOP with a coefficient of determination, $R^2 = 0.74$.

To improve the accuracy of the IOP prediction, a third input value was added to the formula, which was the lens axial length, l (mm). The constant a was replaced with Equation 4.2 relating a to the ratio of the lens to the globe.

$$a = 0.85 + \frac{0.49l}{d} \tag{4.2}$$

Using this equation to relate the predicted IOP to the IOP of the simulation, improved prediction accuracy to a R^2 of 0.93 (see Figure 4.15) Afterwards, the equation was validated by the addition of three new simulations representing the rabbit ocular system under blast. With the addition of the new validation data points, the R^2 was 0.919. These validation data points are shown in orange (see Figure 4.15).

4.4 Discussion

This study used a finite element model of an eye to investigate sensitivity of ocular response to varied ocular anatomical geometry and blast wave loading conditions. The model was simplified in comparison to the full facial models of the Nguyen group [16], [17] and others, as the focus was on the parametric effects of the aforementioned geometry and loading conditions. This model is the first ocular blast model to be validated against IOP measured *in vivo* during blast exposure.

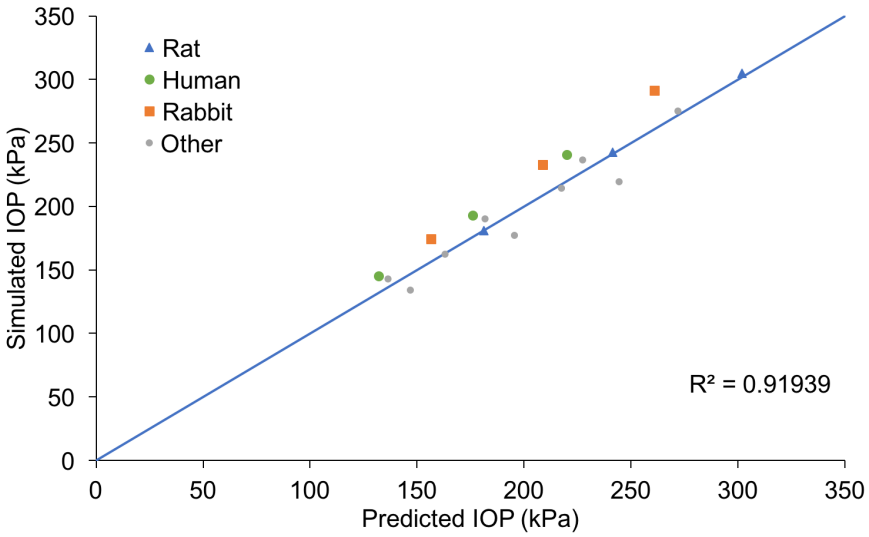

Figure 4.15: Comparison of peak IOP in the FE simulation (y-axis) with predictions from derived equation (x-axis).

Increasing the blast overpressure applied to the eye during the simulation caused significant increases to every model output. These results are consistent with the general expectation that increasing applied force will increase deformation. Scaling the duration of the blast exposure did not significantly impact any peak model outputs, which agreed with the prior computational findings of Esposito et al. [18]. To confirm that the nondetection of the impact of scaled duration was not due to the short simulation time of 3 ms, additional simulations were run up to 50 ms. The peak values extracted from these longer simulations were the same as those extracted from the original three millisecond simulations, indicating that the conclusions reached from shorter simulations were valid.

The range of blast overpressures and phase durations simulated in this model were small (6-10 ms, ±25% from baseline). Blast exposures that have been applied to animals have included positive phase durations ranging between 3 μs [13] and 120 ms [20]. Similar blast overpressures can have significantly different total impulse depending on the duration of the positive phase. The bony orbit of the eye can trap this energy inside of the eye, potentially further increasing damage from the total energy transmitted by the blast, rather than from solely the peak overpressure. It is likely that modeling larger variations of phase duration would cause significantly different mechanical responses in the eye. However, this parametric loading study clearly demonstrated that the material response in the eye was much more dependent on even relatively small percent differences in peak overpressure (180-280 kPa, ±22% from baseline) than it was on changes in phase duration.

From the analysis of the six model geometries, it was determined that the globe diameter had the largest impact on the model outputs, significantly affecting predictions of six of the seven outputs. Variation in globe diameter had an especially large contribution to the displacements measured at the anterior cornea and central lens. Considering that the eye was fixed at the rear, it follows that scaling the entire globe would increase axial deformation values, which are absolute measures and are dependent on length. Measures of strain are normalized by length, so the measures of cornea strain and lens strain were less sensitive to the scaling of the globe, although the globe size was still most predictive of these responses as well. As anticipated, varying either the lens axial length or the cornea size significantly impacted the local model outputs: lens strain/displacement, and cornea stress/strain, respectively. The effect of cornea size on cornea displacement was not quite significant ($p = 0.054$). This is likely due to the extremely dominant effect of globe size on that metric.

These results indicate that animal models with smaller eyes (i.e., smaller globe axial length) will experience higher IOP than larger eyes from the same blast exposure. Therefore, to recreate a specific IOP seen in a human exposed to a blast, the blast loading applied to an animal in a lab must be correspondingly lower. Globe size was the most important parameter for scaling exposures between ocular models, although both the lens size and cornea size also had significant impacts. It is therefore important to note the animal model used in experimental studies, and to compare the implications of size and anatomical differences, when comparing blast exposure levels in experimental models. As a result of these findings, scaling equations were developed to relate ocular scale and anatomy to IOP (see Equations 4.1 and 4.2).

These equations allow the calculation of IOP from given pressure loading and ocular anatomical features. The equations can be combined for a given ocular model as Equation 4.3. By setting two IOPs equal, the equivalent applied pressure loading can be solved for in order to create the same IOP (see Equation 4.4). These equations can be used to compare two different animal models of ocular blast exposure.

$$IOP_{model} = (0.85 + \frac{0.49 l_{model}}{d_{model}}) P_{applied} d_{model}^{-0.0779} \tag{4.3}$$

$$IOP_{model} = IOP_{human} \tag{4.4a}$$

$$a_{model} P_{model} d_{model}^{-0.0779} = a_{human} P_{human} d_{human}^{-0.0779} \tag{4.4b}$$

$$\boxed{P_{model} = P_{human} \frac{a_{human}}{a_{model}} \left(\frac{d_{human}}{d_{model}} \right)^{-0.0779}} \tag{4.4c}$$

where:

$$a_{human} = 0.85 + \frac{0.49 l_{human}}{d_{human}}$$
$$a_{model} = 0.85 + \frac{0.49 l_{model}}{d_{model}}$$

These equations were used to compare injury severity between experimental models found in the literature (Table 4.8). The comparison was limited to shock tube models to limit the disparity between blast devices. It is difficult to evaluate whether the scaled blast accurately predicts injury severity in the models due to the lack of quantitative data, different timepoints used, and different assessment methodologies in each study.

However, the work of Jones et al. quantified corneal thickness changes in rabbits 48 h postblast, finding thickening similar to the corneal thickness increases one day after blast presented in Chapter 3 [56]. The scaled blast of 312 kPa in the present study resulted in normalized thickness changes at 24 h postblast of 39.9% and 17.6% in the directly and indirectly exposed eyes, respectively (bilateral average = 28.7%). The highest blast level in

Table 4.8: Application of Equation 4.4 to shock tube blast models reported in literature. Equivalent scaled human blast loading differs by up to 30% from the experimental loading conditions. Positive phase durations ranged from 2 to 7 ms.

Study	**Animal**	**Experimental Pressure (kPa)**	**Duration (ms)**	**Scaled Pressure (kPa)**	**Injury Findings**
Koliatsos et al. [101]	Mouse	68-105	–	98-151	Optic neuropathy
Wang et al. [102]	Rat	120	2	164	Optic neuropathy and retinal damage
Choi et al. [55]	Rat	70	2	96	Optic neuropathy and retinal damage
Jones et al. [56]	Rabbit	51-132	2.8	60-155	Cornea damage and retinal damage
DeMar et al. [76]	Rat	138	6	189	Optic neuropathy and retinal damage
Present Study	Rat	228	7	312	Cornea damage and contrast deficit

the Jones et al. study was a lower scaled blast level of 155 kPa, and resulted in a smaller normalized thickening of 11.8% at 48 h postblast. The changes in total corneal thickness for each study were normalized by baseline values to allow for comparison between species.

The more severe corneal thickening found in the present study when compared to the Jones et al. study is expected with the increased scaled blast levels. However, the unscaled blast pressures in the models (228 and 132 kPa) would also predict more severe injuries in the present study than the Jones et al. study. Further, it is difficult to compare between the two studies due to differences in timepoints (24 or 48 h) and animal orientation (side-on or face-on). The directly exposed eye in side-on blast is likely more severely exposed than either eye of the face-on orientation, while the least blast load is applied to the indirectly exposed eye.

It is interesting to compare scaling between animal sizes in this equation and that of Bowen et al. for lung injury [6] or more recent scaling equations for blast neurotrauma by Jean et al. [103]. In Bowen, scaling of blast duration was based on pulmonary fatality rates from shock tube experiments using a range of animal species. This relationship was based solely on mass ratios. For the eye, body, or eye mass ratios are not sufficient to generate a similar relationship due to differences in ocular anatomy. Jean et al. translated animal blast exposure to correspondingly scaled human equivalent overpressure to generate equal intracranial pressures (ICP). This approach is similar to that of the present study in that both used FE models to develop scaling predictions and in that the ICP is the brain-specific analogue to the IOP used in the present study. The predictive formula of Jean et al. incorporated not only the body mass, but also the mass of protective tissues relative to the brain size. This relationship predicted that, in contrast to many other injury modalities, the increased size of the human compared to animal models did not act to reduce the relative injury risk. Instead, the human was uniquely vulnerable to brain injury due to the large brain size and thin skull that characterizes human anatomy. Moreover, the decreased susceptibility of small animal models to TBI predicted by the Jean et al. model combined with the increased sensitivity of small animals to ocular injury predicted by the present study indicates that use of small animal studies may feature increased ocular injury and decreased TBI when compared to human equivalent injury.

4.4.1 Limitations

This FE model was designed to simulate the interaction of the globe with the blast wave. The eye itself was also greatly simplified, with only four main ocular components modeled. These components were chosen because they represent the majority of the

mechanical responses of the eye. Addition of more components to the model would therefore not likely change the gross response of the eye, but would allow localized predictions of potential injury. The material properties of the eye were limited based on model complexity and availability of data. In particular, viscoelastic data were sourced from relatively low-rate testing. High-rate viscoelastic testing for ocular tissues could improve the material models used in this and other computational studies modeling blast. Implementation of viscoelasticity in the cornea and vitreous could significantly change the effective stiffness of both tissues under high-rate loading.

The orbit and facial features were not included in the model. Adding these features and more realistic boundary conditions would add significant complexity to the model. Facial features are known to increase the blast pressure experienced by the eye relative to the open field pressure [16], so the effect of facial features could potentially be approximated by applying increased blast loading to compensate for the omission of the missing focusing effect. However, it would be difficult to account for differences in animal facial features without modeling animal specific orbit and facial geometries. Replacing the fixed posterior boundary condition with orbital bone and fatty tissues would allow the eye to displace within the orbit, and could potentially decrease the overall deformation of the eye, while increasing localized concentrations of stress and strain at contact areas. Additionally, the omission of ciliary zonules tethering the lens to the globe could result in overestimation of lens displacement. In the current models, lens displacement was small, but future models that result in larger lens displacements may need to reconsider whether omission of the zonules is appropriate.

Accurate IOP recorded *in vivo* during blast from other animal models would be beneficial to fully validate the model for varied geometries. Accuracy of the scaling equations presented in this chapter may be limited due to unaccounted differences between animal species in both the material properties, as well as the focusing effects of facial features acting to increase the pressure experienced by the eye. As long as animal models used in this equation involve direct blast exposure to the eyes, facial structure differences may induce less significant error into the predictions. Furthermore, DeMar et al. demonstrated that orientation of the eye with respect to blast has a significant impact on injury findings, with side-on blast in a rodent recreating frontal human exposure [76].

The creation of the scaling equation developed in this work is based on the assumption that the IOP equivalence is sufficient to equate blast levels between experimental models. The IOP was chosen because it was the component of the model that was directly

validated by experimental data. However, it is possible that some ocular blast injury modalities are not predicted by IOP. For these cases, Equation 4.4 would not accurately scale risk of injury.

4.5 Conclusion

A parametric computational model was presented to simulate varied blast loading on six ocular geometries. This is the first computational model to be validated against *in vivo* IOP data during blast exposure rather than blunt impact or *ex vivo* experimental data. The three geometry variables investigated were globe size, lens axial length, and cornea size. Each of these variables had significant impacts on the mechanical response of the eye under blast loading. The magnitude of blast overpressure applied to the model had a greater significant effect on model response, than the positive phase duration. Predictions of intraocular pressure were significantly linked to the blast overpressure, globe size, and lens size. These three variables were used to create scaling equations (see Equations 4.1 and 4.2) that predict the peak IOP in the eye. These equations can also be used to compare pressures between different experimental animal models or to connect a human blast exposure to the corresponding experimental blast pressure for the purposes of recreating a similar pressure loading (see Equation 4.4).

CHAPTER 5

CONCLUSIONS AND FUTURE WORK

5.1 Summary of Key Findings

The goal of this research was to study long-term closed globe injury sequelae subsequent to primary blast exposure, and evaluate the effect of anatomical features on ocular injury. A shock tube was assembled and characterized to apply a Friedlander open field blast to a rat model. Visual acuity deficits and delayed cornea damage were detected in animals exposed to blast. IOP was recorded during blast in a subset of animals, providing a valuable validation tool for computer modelling of the eye in blast. Parametric study of the eye under primary blast loading allowed the development of scaling equations to compare blast exposure between animal blast studies and to translate real-world blast parameters into a laboratory setting.

5.1.1 Development of Shock Tube Ocular Injury Model

The tube delivered blast pressures of 230 kPa with positive phase durations of 7 ms. The ideal experimental location for application of the Friedlander waveform was 445 cm from the membrane. A holder apparatus was designed and built to expose the head and eye of the animal to blast, while protecting the torso and lungs.

Each of the three simulated driver gases (helium, hydrogen, and air) created a Friedlander shock wave within the tube. The pressure profiles created by lighter driver gases had shorter positive phase durations. Driver gas was not varied in the characterization of the physical tube, but could be used in the future to tune the positive phase duration generated by the device.

As expected, the use of thicker BoPET membranes allowed higher driver pressures at rupture. The efficiency of energy transfer from the pressurized driver into the shock wave in the driven section was dependent on both driver pressure and membrane thickness. In general, higher pressures increased efficiency for a given membrane thickness, and thinner

membranes were more efficient at a given driver pressure than thicker membranes. Energy loss due to membrane rupture is the logical cause of the different efficiencies.

5.1.2 Experimental Investigation of Ocular Injury Resulting from Blast Exposure

Side-on blast exposure to the right eye of rats resulted in significant contrast sensitivity deficits that were detected one day after blast and did not resolve in the eight weeks after exposure. There was more significant corneal thickening in the directly exposed right eye than the indirectly exposed left eye, and no thickening in control animals. The corneal thickening was delayed in presentation, and although the thickness of the right eye diminished by the end of the eight week study, corneal scarring remained. There were no retinal thickness changes detected during this study. Because there was a delay between blast exposure and corneal damage, a potential treatment window exists to mitigate long-term visual loss due to corneal inflammation and scarring.

Measurements of IOP were recorded *in vivo* during blast exposure. IOP in both eyes increased by orders of magnitude above physiologic levels, with the right eye nearly matching external tube measurements. These data provide valuable validation data for FE models, and quantified load conditions in the eyes during side-on blast.

5.1.3 Investigation of Ocular Blast Using FE Model

Parametric evaluation of the eye under blast loading yielded insight into the importance of both anatomical differences and loading conditions in ocular blast injury. The computer model was validated against IOP measured in experimental studies. The three model parameters most influential on IOP were the blast overpressure magnitude, globe axial length, and lens axial length. These parameters were used to propose a scaling equation that predicts IOP. Accuracy of the model was assessed with human, rat, and rabbit simulations ($R^2 = 0.92$). Differences in orientation, material properties, or facial features were not considered. The scaling equation can be used to compare previous studies using differing animal models and blast pressures, and also to plan future studies to replicate specific human blast loading in animal models.

5.2 Future Work

The shock tube developed in this research accurately recreates the Friedlander waveform. However, the blast pressure created by the device is difficult to control. Improving the driver section of the tube to have variable length would allow for studies at a wide

range of peak overpressures and durations. Increased control of the shock wave parameters generated by the tube would allow an experimental parametric study to test the findings of the computer model described in Chapter 4. Additionally, varying the shock parameters could lead to the development of injury risk thresholds based on experimental data. A second limitation of the shock tube is the limited diameter of the experimental section (15 cm). An expansion cone could be installed on the tube to allow large animal studies to be conducted. Large animals have more similar ocular anatomy to the human eye, and may be easier to directly interpret the results in terms of human injury. Future studies with large animals would also allow direct validation of the alternate ocular geometries used in the computational study and the associated scaling equation.

Delayed ocular injury was observed, with a potential treatment window found between blast exposure and the onset of corneal damage. Further work is necessary to isolate the inflammatory pathways leading to corneal swelling and scarring. Studies performed on eyes from blast exposed rats in this study found that biomarker concentrations including neurofilament heavy chain (NfH), lipopolysaccharide-inducible CXC chemokine (LIX), interleukin-10 (IL-10), and tumor necrosis factor alpha (TNF-α) were increased in the right eye of blast exposed animals compared to control animals. These elevated concentrations correlate with the timing of corneal swelling and are targets for further study with genetic knockout animals to isolate the key pathways of injury, and potential pharmacological mitigation strategies. Corneal swelling may also be linked to changes in endothelial cell density. The endothelium controls fluid uptake from the aqueous to the cornea and dysfunction to this layer could contribute to the corneal swelling seen in this study and requires further study.

Visual acuity significantly decreased in blast exposed animals. Future experimental studies should add additional assessments of visual ability to discern the source of these deficits, as the corneal damage did not fully explain the early onset of visual deficits. Specifically, visual evoked potential (VEP) and electroretinogram (ERG) can assess loss of functionality. Use of these tests in combination can attribute deficits to the optic nerve and retina, and would aid understanding of the visual acuity and contrast sensitivity deficits demonstrated in this and other studies.

In this work, a novel method for recording IOP during blast using fiber optic pressure sensors was developed. Data from these experiments is invaluable as validation data for FE models. However, to date, IOP has only been measured from a single experimental model (rat) under one set of blast loading conditions. The techniques developed here

can be applied in other animal models to develop a larger database of validation data for researchers. Moreover, more accurate data can be acquired from animal models with increased vitreous space. Sensor size was limited in the rat model due to the small eye and high portion of the interior obscured by the lens. Studies in large animals could use larger, more robust pressure transducers to gather improved IOP data.

The computer model developed in this project was relatively simplified. Additional anatomical features, improved boundary conditions, and facial structures could improve the model. These features would allow localized predictions of injury risk, and further differentiate findings between animal models. Additionally, improved material model data for ocular tissues is likely necessary for accurate prediction of stress and strain. The majority of ocular mechanical studies are interested in chronic IOP increases or relatively slow loading conditions, so data for high rate loading is scarce. Data from high rate material testing is essential in ensuring that the rapid blast wave interaction can be accurately modeled.

The eventual goal of primary blast injury research is to develop new protection and treatment solutions to mitigate the frequency and severity of injury. Understanding the inflammatory pathways, injury progression, and vulnerable anatomy involved in blast-related vision loss will allow treatment studies aimed at downregulating injury pathways and the design of new protective equipment to improve outcomes for blast-exposed individuals.

APPENDIX A

CHAPTER 2 DATA TABLES

Table A.1: Computer model pressure-time curve compared to theoretical Friedlander waveform. Figure 2.15 includes these data.

Time (ms)	**Model Pressure (kPa)**	**Friedlander Pressure (kPa)**		**Time (ms)**	**Model Pressure (kPa)**	**Friedlander Pressure (kPa)**
0.000	0.8	120.0		3.012	2.4	-14.7
0.012	3.0	117.6		3.025	2.7	-14.7
0.025	11.5	115.1		3.037	2.9	-14.6
0.038	33.5	112.7		3.050	3.0	-14.6
0.049	65.5	110.4		3.061	3.1	-14.5
0.062	96.8	108.0		3.075	3.2	-14.5
0.074	108.1	105.8		3.088	3.2	-14.4
0.087	109.2	103.4		3.099	3.1	-14.4
0.099	107.7	101.4		3.113	2.8	-14.3
0.112	105.5	99.1		3.125	2.5	-14.2
0.124	104.2	97.0		3.137	2.2	-14.2
0.138	103.5	94.7		3.149	1.8	-14.1
0.149	103.1	92.8		3.162	1.3	-14.1
0.162	102.6	90.7		3.174	0.8	-14.0
0.175	101.9	88.7		3.187	0.4	-14.0
0.187	101.2	86.6		3.199	-0.1	-13.9
0.200	100.6	84.6		3.212	-0.5	-13.8
0.211	100.0	82.9		3.225	-0.9	-13.8
0.224	99.2	81.0		3.237	-1.3	-13.7
0.237	98.4	79.0		3.249	-1.6	-13.7
0.250	97.5	77.1		3.262	-1.9	-13.6
0.262	96.7	75.5		3.274	-2.2	-13.5
0.275	95.8	73.6		3.287	-2.4	-13.5
0.287	95.1	71.9		3.299	-2.6	-13.4
0.299	94.4	70.2		3.312	-2.8	-13.4
0.312	93.6	68.4		3.325	-2.9	-13.3
0.324	92.8	66.8		3.338	-3.0	-13.2
0.336	92.0	65.2		3.349	-3.0	-13.2
0.350	91.1	63.5		3.362	-3.0	-13.1
0.362	90.4	62.0		3.375	-2.9	-13.1
0.375	89.5	60.3		3.387	-2.8	-13.0
0.387	88.8	58.9		3.399	-2.6	-12.9
0.399	87.9	57.4		3.413	-2.3	-12.9
0.413	86.9	55.8		3.425	-2.0	-12.8
0.424	85.8	54.4		3.438	-1.6	-12.8
0.436	84.7	53.1		3.449	-1.3	-12.7
0.450	83.4	51.6		3.462	-0.9	-12.6

Table A.1: Continued

Time (ms)	Model Pressure (kPa)	Friedlander Pressure (kPa)		Time (ms)	Model Pressure (kPa)	Friedlander Pressure (kPa)
0.462	82.2	50.2		3.475	-0.5	-12.6
0.475	80.7	48.8		3.487	0.0	-12.5
0.487	79.2	47.5		3.500	0.4	-12.4
0.499	77.6	46.2		3.512	0.9	-12.4
0.513	75.6	44.8		3.525	1.4	-12.3
0.525	73.7	43.6		3.537	1.8	-12.3
0.537	71.7	42.4		3.550	2.2	-12.2
0.550	69.4	41.1		3.561	2.5	-12.1
0.562	67.3	39.9		3.575	2.9	-12.1
0.574	65.2	38.8		3.586	3.1	-12.0
0.587	62.8	37.6		3.600	3.4	-11.9
0.599	60.7	36.5		3.612	3.5	-11.9
0.612	58.3	35.3		3.625	3.5	-11.8
0.624	56.3	34.2		3.637	3.4	-11.8
0.638	54.1	33.0		3.649	3.2	-11.7
0.650	52.2	32.0		3.663	2.9	-11.6
0.662	50.3	31.0		3.674	2.6	-11.6
0.675	48.1	29.9		3.687	2.2	-11.5
0.688	46.2	28.9		3.700	1.8	-11.5
0.700	44.3	27.9		3.711	1.4	-11.4
0.712	42.4	27.0		3.724	0.9	-11.3
0.724	40.5	26.0		3.737	0.4	-11.3
0.738	38.5	25.0		3.749	-0.1	-11.2
0.750	36.8	24.1		3.763	-0.6	-11.1
0.762	35.2	23.2		3.775	-1.1	-11.1
0.775	33.6	22.3		3.787	-1.6	-11.0
0.787	32.2	21.5		3.799	-2.0	-11.0
0.800	30.6	20.5		3.813	-2.4	-10.9
0.812	29.2	19.7		3.824	-2.6	-10.8
0.824	27.8	18.9		3.838	-2.9	-10.8
0.837	26.2	18.0		3.849	-3.0	-10.7
0.849	25.0	17.3		3.862	-3.1	-10.7
0.863	23.6	16.4		3.875	-3.1	-10.6
0.874	22.5	15.7		3.887	-3.1	-10.5
0.887	21.2	14.9		3.900	-3.0	-10.5
0.899	20.1	14.2		3.912	-2.8	-10.4
0.912	18.9	13.5		3.924	-2.6	-10.4
0.925	17.7	12.7		3.937	-2.4	-10.3
0.936	16.6	12.1		3.950	-2.1	-10.2
0.949	15.5	11.4		3.962	-1.7	-10.2
0.962	14.4	10.7		3.975	-1.3	-10.1
0.975	13.3	10.0		3.987	-0.8	-10.0
0.988	12.3	9.3		4.000	-0.3	-10.0
0.999	11.5	8.7		4.012	0.2	-9.9
1.012	10.5	8.1		4.024	0.7	-9.9
1.025	9.6	7.5		4.037	1.2	-9.8
1.036	8.7	6.9		4.049	1.6	-9.8
1.049	7.8	6.3		4.062	2.0	-9.7
1.062	6.9	5.7		4.075	2.4	-9.6
1.074	6.2	5.2		4.087	2.6	-9.6
1.087	5.4	4.6		4.099	2.9	-9.5
1.100	4.6	4.0		4.112	3.0	-9.5

Table A.1: Continued

Time (ms)	Model Pressure (kPa)	Friedlander Pressure (kPa)		Time (ms)	Model Pressure (kPa)	Friedlander Pressure (kPa)
1.112	3.9	3.5		4.125	3.1	-9.4
1.125	3.2	2.9		4.137	3.1	-9.3
1.137	2.5	2.5		4.149	3.1	-9.3
1.150	1.8	1.9		4.162	2.9	-9.2
1.162	1.2	1.5		4.174	2.7	-9.2
1.175	0.5	0.9		4.187	2.4	-9.1
1.186	-0.1	0.5		4.200	2.0	-9.1
1.200	-0.8	0.0		4.212	1.7	-9.0
1.213	-1.5	-0.5		4.225	1.2	-8.9
1.225	-2.1	-0.9		4.236	0.8	-8.9
1.238	-2.8	-1.3		4.250	0.3	-8.8
1.249	-3.3	-1.7		4.263	-0.2	-8.8
1.262	-3.9	-2.2		4.275	-0.7	-8.7
1.274	-4.4	-2.6		4.287	-1.1	-8.7
1.287	-4.9	-3.0		4.300	-1.5	-8.6
1.300	-5.4	-3.4		4.312	-1.9	-8.6
1.312	-5.8	-3.8		4.325	-2.3	-8.5
1.325	-6.1	-4.1		4.337	-2.5	-8.5
1.337	-6.4	-4.5		4.350	-2.7	-8.4
1.350	-6.6	-4.9		4.362	-2.8	-8.3
1.362	-6.8	-5.2		4.375	-2.9	-8.3
1.374	-6.8	-5.5		4.387	-2.9	-8.2
1.387	-6.8	-5.9		4.399	-2.8	-8.2
1.399	-6.7	-6.2		4.413	-2.7	-8.1
1.412	-6.4	-6.5		4.424	-2.5	-8.1
1.424	-6.0	-6.8		4.438	-2.3	-8.0
1.438	-5.6	-7.2		4.450	-2.0	-8.0
1.450	-5.3	-7.5		4.462	-1.6	-7.9
1.462	-4.9	-7.7		4.474	-1.2	-7.9
1.475	-4.6	-8.0		4.487	-0.8	-7.8
1.487	-4.1	-8.3		4.500	-0.3	-7.8
1.499	-3.5	-8.6		4.513	0.2	-7.7
1.512	-2.8	-8.9		4.525	0.6	-7.7
1.525	-2.1	-9.1		4.538	1.1	-7.6
1.537	-1.4	-9.4		4.550	1.5	-7.6
1.550	-0.5	-9.6		4.562	1.9	-7.5
1.563	0.2	-9.9		4.575	2.2	-7.5
1.575	1.0	-10.1		4.587	2.5	-7.4
1.586	1.6	-10.3		4.600	2.7	-7.4
1.599	2.4	-10.5		4.612	2.8	-7.3
1.612	3.1	-10.7		4.624	2.9	-7.3
1.625	3.9	-11.0		4.637	2.8	-7.2
1.638	4.6	-11.2		4.649	2.7	-7.2
1.649	5.2	-11.4		4.662	2.5	-7.1
1.663	5.7	-11.6		4.674	2.3	-7.1
1.675	6.0	-11.8		4.687	2.0	-7.0
1.688	6.2	-11.9		4.699	1.6	-7.0
1.699	6.3	-12.1		4.713	1.2	-6.9
1.712	6.2	-12.3		4.725	0.8	-6.9
1.724	6.0	-12.5		4.737	0.4	-6.8
1.737	5.7	-12.6		4.750	-0.1	-6.8
1.749	5.4	-12.8		4.762	-0.5	-6.7

Table A.1: Continued

Time (ms)	Model Pressure (kPa)	Friedlander Pressure (kPa)		Time (ms)	Model Pressure (kPa)	Friedlander Pressure (kPa)
1.763	5.1	-13.0		4.774	-0.9	-6.7
1.775	4.8	-13.1		4.788	-1.3	-6.6
1.787	4.4	-13.2		4.800	-1.7	-6.6
1.799	4.0	-13.4		4.812	-2.0	-6.6
1.811	3.5	-13.5		4.825	-2.3	-6.5
1.825	3.0	-13.7		4.837	-2.5	-6.5
1.837	2.4	-13.8		4.849	-2.6	-6.4
1.849	1.9	-13.9		4.862	-2.7	-6.4
1.862	1.4	-14.0		4.875	-2.8	-6.3
1.875	0.8	-14.2		4.887	-2.7	-6.3
1.888	0.3	-14.3		4.900	-2.6	-6.2
1.900	-0.2	-14.4		4.913	-2.4	-6.2
1.912	-0.8	-14.5		4.925	-2.1	-6.1
1.925	-1.4	-14.6		4.938	-1.7	-6.1
1.937	-1.9	-14.7		4.950	-1.3	-6.1
1.950	-2.5	-14.8		4.962	-0.9	-6.0
1.962	-3.0	-14.9		4.974	-0.4	-6.0
1.974	-3.5	-14.9		4.987	0.1	-5.9
1.987	-4.0	-15.0		5.000	0.6	-5.9
1.999	-4.4	-15.1		5.012	1.0	-5.9
2.012	-4.7	-15.2		5.024	1.4	-5.8
2.024	-5.0	-15.3		5.038	1.8	-5.8
2.036	-5.1	-15.3		5.050	2.1	-5.7
2.050	-5.3	-15.4		5.062	2.3	-5.7
2.063	-5.3	-15.5		5.075	2.4	-5.6
2.075	-5.2	-15.5		5.087	2.5	-5.6
2.088	-5.1	-15.6		5.099	2.5	-5.6
2.100	-4.9	-15.6		5.112	2.4	-5.5
2.112	-4.6	-15.7		5.124	2.2	-5.5
2.125	-4.3	-15.7		5.137	2.0	-5.4
2.137	-3.8	-15.8		5.149	1.8	-5.4
2.149	-3.2	-15.8		5.163	1.5	-5.4
2.163	-2.4	-15.9		5.175	1.1	-5.3
2.175	-1.7	-15.9		5.187	0.8	-5.3
2.187	-1.0	-16.0		5.199	0.5	-5.3
2.200	-0.3	-16.0		5.213	0.1	-5.2
2.212	0.5	-16.0		5.226	-0.3	-5.2
2.225	1.2	-16.0		5.238	-0.7	-5.1
2.237	1.9	-16.1		5.250	-1.0	-5.1
2.249	2.4	-16.1		5.263	-1.3	-5.1
2.262	2.8	-16.1		5.275	-1.6	-5.0
2.274	3.0	-16.1		5.287	-1.8	-5.0
2.288	3.0	-16.2		5.299	-2.0	-5.0
2.299	3.0	-16.2		5.312	-2.1	-4.9
2.312	3.0	-16.2		5.325	-2.2	-4.9
2.324	3.0	-16.2		5.337	-2.2	-4.8
2.337	3.1	-16.2		5.350	-2.1	-4.8
2.350	3.3	-16.2		5.362	-2.0	-4.8
2.362	3.6	-16.2		5.375	-1.8	-4.7
2.375	3.7	-16.2		5.387	-1.6	-4.7
2.387	3.7	-16.2		5.400	-1.3	-4.7
2.400	3.6	-16.2		5.412	-1.1	-4.6

Table A.1: Continued

Time (ms)	Model Pressure (kPa)	Friedlander Pressure (kPa)		Time (ms)	Model Pressure (kPa)	Friedlander Pressure (kPa)
2.412	3.4	-16.2		5.425	-0.7	-4.6
2.424	3.2	-16.2		5.437	-0.4	-4.6
2.437	2.8	-16.2		5.450	-0.1	-4.5
2.449	2.5	-16.2		5.462	0.2	-4.5
2.462	2.2	-16.2		5.474	0.6	-4.5
2.474	2.0	-16.2		5.487	0.9	-4.4
2.487	1.8	-16.2		5.499	1.2	-4.4
2.500	1.5	-16.2		5.513	1.4	-4.4
2.513	1.4	-16.2		5.525	1.6	-4.3
2.525	1.2	-16.2		5.537	1.8	-4.3
2.536	1.0	-16.1		5.550	1.9	-4.3
2.550	0.8	-16.1		5.562	1.9	-4.2
2.563	0.4	-16.1		5.574	1.9	-4.2
2.574	0.1	-16.1		5.588	1.8	-4.2
2.588	-0.3	-16.1		5.600	1.7	-4.1
2.600	-0.7	-16.0		5.612	1.5	-4.1
2.612	-1.2	-16.0		5.624	1.3	-4.1
2.625	-1.6	-16.0		5.638	1.0	-4.0
2.637	-2.0	-16.0		5.650	0.7	-4.0
2.649	-2.3	-15.9		5.661	0.5	-4.0
2.662	-2.6	-15.9		5.675	0.1	-4.0
2.675	-2.9	-15.9		5.687	-0.2	-3.9
2.688	-3.0	-15.8		5.699	-0.4	-3.9
2.700	-3.1	-15.8		5.713	-0.7	-3.9
2.712	-3.1	-15.8		5.725	-1.0	-3.8
2.724	-3.0	-15.7		5.737	-1.2	-3.8
2.737	-2.9	-15.7		5.750	-1.4	-3.8
2.750	-2.7	-15.7		5.762	-1.5	-3.7
2.762	-2.5	-15.6		5.774	-1.6	-3.7
2.774	-2.4	-15.6		5.788	-1.7	-3.7
2.787	-2.2	-15.6		5.800	-1.7	-3.7
2.800	-2.0	-15.5		5.813	-1.7	-3.6
2.812	-1.8	-15.5		5.824	-1.7	-3.6
2.824	-1.7	-15.4		5.837	-1.5	-3.6
2.837	-1.4	-15.4		5.850	-1.4	-3.6
2.849	-1.2	-15.3		5.862	-1.2	-3.5
2.862	-0.9	-15.3		5.874	-0.9	-3.5
2.874	-0.6	-15.3		5.887	-0.7	-3.5
2.888	-0.2	-15.2		5.899	-0.4	-3.4
2.900	0.1	-15.2		5.912	-0.1	-3.4
2.911	0.4	-15.1		5.925	0.2	-3.4
2.924	0.6	-15.1		5.937	0.5	-3.4
2.937	0.9	-15.0		5.950	0.8	-3.3
2.950	1.1	-15.0		5.962	1.0	-3.3
2.962	1.3	-14.9		5.974	1.2	-3.3
2.974	1.6	-14.9		5.988	1.4	-3.3
2.988	1.9	-14.8		6.000	1.5	-3.2
3.000	2.2	-14.8		6.012	1.5	-3.2

Table A.2: Pressure-time curves for three driver gases. Figure 2.16 includes these data.

Time (ms)	Helium	Hydrogen	Air		Time (ms)	Helium	Hydrogen	Air
3.30	0.0	0.1	0.0		7.66	21.0	22.0	34.4
3.31	0.0	0.1	0.0		7.68	21.1	22.1	34.2
3.33	0.0	0.1	0.0		7.69	21.2	22.1	33.8
3.34	0.0	0.1	0.0		7.70	21.2	22.2	33.5
3.35	0.0	0.1	0.0		7.71	21.3	22.3	33.3
3.36	0.0	0.1	0.0		7.73	21.4	22.4	33.0
3.38	0.0	0.1	0.0		7.74	21.5	22.4	32.6
3.39	0.0	0.1	0.0		7.75	21.6	22.3	32.3
3.40	0.0	0.4	0.0		7.76	21.7	22.2	32.0
3.41	0.0	1.7	0.0		7.78	21.8	22.1	31.5
3.43	0.0	6.9	0.0		7.79	21.9	21.9	31.2
3.44	0.0	24.2	0.0		7.80	22.0	21.7	30.9
3.45	0.1	61.4	0.0		7.81	22.1	21.5	30.5
3.46	0.1	107.8	0.0		7.83	22.1	21.3	30.2
3.48	0.2	127.8	0.0		7.84	22.1	21.2	29.9
3.49	0.7	130.7	0.0		7.85	22.1	21.0	29.6
3.50	3.1	129.6	0.0		7.86	22.1	20.9	29.3
3.51	11.9	127.6	0.0		7.88	22.1	20.8	29.1
3.53	35.4	126.2	0.0		7.89	22.1	20.7	28.8
3.54	74.3	125.5	0.0		7.90	22.1	20.7	28.6
3.55	108.9	125.0	0.0		7.91	22.0	20.8	28.3
3.56	123.5	124.1	0.0		7.93	22.0	20.9	28.1
3.58	124.4	123.0	0.0		7.94	21.9	21.1	27.9
3.59	123.1	121.7	0.0		7.95	21.8	21.3	27.6
3.60	121.9	120.4	0.0		7.96	21.7	21.5	27.4
3.61	121.4	119.1	0.0		7.98	21.7	21.7	27.0
3.63	121.3	117.7	0.0		7.99	21.6	21.9	26.7
3.64	121.2	116.2	0.0		8.00	21.6	22.2	26.4
3.65	121.1	114.8	0.0		8.01	21.6	22.5	26.1
3.66	120.9	113.3	0.0		8.03	21.6	22.7	25.8
3.68	120.8	111.9	0.0		8.04	21.7	22.9	25.4
3.69	120.5	110.7	0.0		8.05	21.7	23.0	25.1
3.70	120.3	109.4	0.0		8.06	21.7	23.1	24.7
3.71	120.1	108.3	0.0		8.08	21.7	23.1	24.5
3.73	119.8	107.3	0.0		8.09	21.7	23.0	24.2
3.74	119.5	106.2	0.0		8.10	21.7	22.8	23.9
3.75	119.1	105.0	0.0		8.11	21.6	22.6	23.6
3.76	118.6	103.6	0.1		8.13	21.5	22.4	23.3
3.78	118.1	102.0	0.3		8.14	21.3	22.2	23.1
3.79	117.4	100.3	1.1		8.15	21.2	22.0	22.8
3.80	116.6	98.9	4.5		8.16	20.9	21.8	22.5
3.81	115.8	97.6	10.6		8.18	20.7	21.6	22.3
3.83	115.0	96.6	30.4		8.19	20.5	21.5	22.1
3.84	114.1	95.6	60.5		8.20	20.2	21.3	21.8
3.85	113.1	94.8	78.0		8.21	20.0	21.2	21.5
3.86	112.1	93.8	89.1		8.23	19.8	21.1	21.2
3.88	111.1	92.8	90.8		8.24	19.7	21.0	20.9
3.89	110.0	91.6	90.3		8.25	19.6	20.9	20.6
3.90	108.8	90.6	90.1		8.26	19.4	20.9	20.4
3.91	107.7	89.6	90.1		8.28	19.3	20.8	20.1
3.93	106.6	88.7	90.6		8.29	19.2	20.8	19.9
3.94	105.4	87.7	91.0		8.30	19.1	20.7	19.6
3.95	104.1	86.8	91.1		8.31	19.0	20.6	19.4
3.96	102.9	86.0	91.1		8.33	19.0	20.4	19.1

Table A.2: Continued

Time (ms)	Helium	Hydrogen	Air		Time (ms)	Helium	Hydrogen	Air
3.98	101.6	85.2	91.1		8.34	18.9	20.2	18.8
3.99	100.5	84.6	91.1		8.35	18.7	19.9	18.6
4.00	99.5	84.0	91.0		8.36	18.6	19.7	18.3
4.01	98.5	83.5	90.8		8.38	18.5	19.4	18.1
4.03	97.4	83.0	90.7		8.39	18.4	19.1	17.9
4.04	96.4	82.6	90.5		8.40	18.3	18.8	17.6
4.05	95.3	82.1	90.3		8.41	18.2	18.6	17.4
4.06	94.3	81.6	90.1		8.43	18.1	18.5	17.2
4.08	93.0	81.1	89.9		8.44	17.9	18.3	17.0
4.09	91.8	80.6	89.7		8.45	17.8	18.3	16.8
4.10	90.5	80.1	89.6		8.46	17.6	18.1	16.6
4.11	89.4	79.8	89.3		8.48	17.4	18.0	16.5
4.13	88.1	79.5	89.1		8.49	17.3	17.7	16.3
4.14	86.9	79.3	88.9		8.50	17.1	17.4	16.1
4.15	85.8	79.1	88.6		8.51	17.0	17.0	15.9
4.16	84.9	79.0	88.3		8.53	16.8	16.7	15.7
4.18	84.0	78.8	88.1		8.54	16.7	16.5	15.4
4.19	83.3	78.6	88.0		8.55	16.5	16.4	15.2
4.20	82.7	78.3	88.0		8.56	16.4	16.4	15.0
4.21	81.9	78.0	88.0		8.58	16.2	16.6	14.8
4.23	81.1	77.8	88.1		8.59	16.1	16.8	14.6
4.24	80.4	77.7	88.2		8.60	15.9	17.0	14.5
4.25	79.4	77.6	88.4		8.61	15.8	17.1	14.3
4.26	78.6	77.5	88.6		8.63	15.7	17.0	14.1
4.28	77.7	77.5	88.9		8.64	15.6	16.9	13.9
4.29	76.8	77.3	89.0		8.65	15.5	16.7	13.7
4.30	75.9	77.2	89.0		8.66	15.4	16.4	13.5
4.31	75.1	77.0	89.0		8.68	15.3	16.2	13.3
4.33	74.1	76.9	88.9		8.69	15.2	16.1	13.1
4.34	73.3	76.7	88.8		8.70	15.1	15.9	13.0
4.35	72.5	76.5	88.7		8.71	15.1	15.8	12.8
4.36	71.7	76.3	88.5		8.73	15.0	15.7	12.7
4.38	71.0	75.9	88.4		8.74	14.9	15.7	12.6
4.39	70.2	75.5	88.2		8.75	14.8	15.6	12.4
4.40	69.5	75.0	88.1		8.76	14.7	15.6	12.3
4.41	68.7	74.5	88.0		8.78	14.5	15.6	12.2
4.43	68.1	73.9	87.9		8.79	14.4	15.6	12.0
4.44	67.4	73.3	87.8		8.80	14.3	15.5	11.9
4.45	66.8	72.8	87.7		8.81	14.2	15.4	11.8
4.46	66.2	72.2	87.5		8.83	14.1	15.3	11.7
4.48	65.7	71.7	87.4		8.84	13.9	15.1	11.5
4.49	65.2	71.2	87.3		8.85	13.8	14.9	11.5
4.50	64.6	70.7	87.1		8.86	13.7	14.8	11.4
4.51	64.1	70.3	87.0		8.88	13.7	14.7	11.3
4.53	63.5	70.0	87.0		8.89	13.6	14.6	11.2
4.54	63.0	69.7	87.0		8.90	13.5	14.6	11.2
4.55	62.4	69.5	87.0		8.91	13.5	14.5	11.1
4.56	61.9	69.4	87.1		8.93	13.4	14.5	11.1
4.58	61.5	69.2	87.2		8.94	13.4	14.4	11.0
4.59	61.1	69.2	87.2		8.95	13.3	14.3	11.0
4.60	60.7	69.1	87.2		8.96	13.3	14.2	11.0
4.61	60.3	69.1	87.1		8.98	13.2	14.0	11.0
4.63	60.0	69.1	86.9		8.99	13.2	13.9	11.0
4.64	59.6	69.1	86.7		9.00	13.2	13.8	11.0

Table A.2: Continued

Time (ms)	Helium	Hydrogen	Air		Time (ms)	Helium	Hydrogen	Air
4.65	59.3	69.1	86.4		9.01	13.2	13.8	10.9
4.66	59.1	69.0	85.9		9.03	13.1	13.9	10.9
4.68	58.8	68.9	85.6		9.04	13.1	14.0	10.9
4.69	58.5	68.8	85.0		9.05	13.0	14.2	10.9
4.70	58.1	68.5	84.4		9.06	12.9	14.3	10.9
4.71	57.8	68.3	83.8		9.08	12.8	14.3	10.9
4.73	57.3	68.1	83.3		9.09	12.7	14.2	10.9
4.74	56.9	67.9	82.9		9.10	12.6	13.9	10.9
4.75	56.5	67.7	82.4		9.11	12.5	13.4	11.0
4.76	56.1	67.6	81.8		9.13	12.3	12.9	11.0
4.78	55.7	67.4	81.3		9.14	12.2	12.5	11.1
4.79	55.4	67.2	80.9		9.15	12.1	12.3	11.1
4.80	55.1	67.0	80.4		9.16	12.0	12.2	11.2
4.81	54.8	66.8	79.9		9.18	11.8	12.3	11.2
4.83	54.5	66.6	79.5		9.19	11.8	12.5	11.3
4.84	54.2	66.5	79.2		9.20	11.7	12.8	11.4
4.85	53.9	66.4	79.0		9.21	11.6	13.0	11.4
4.86	53.6	66.4	79.0		9.23	11.6	13.1	11.5
4.88	53.5	66.4	78.9		9.24	11.6	13.2	11.5
4.89	53.4	66.3	79.0		9.25	11.6	13.2	11.5
4.90	53.4	66.2	79.3		9.26	11.6	13.3	11.5
4.91	53.5	66.1	79.8		9.28	11.6	13.4	11.5
4.93	53.5	66.0	80.6		9.29	11.7	13.5	11.5
4.94	53.5	65.8	81.4		9.30	11.7	13.5	11.5
4.95	53.5	65.6	82.2		9.31	11.7	13.4	11.4
4.96	53.5	65.3	83.1		9.33	11.7	13.2	11.4
4.98	53.4	65.0	83.9		9.34	11.7	12.8	11.4
4.99	53.4	64.6	84.4		9.35	11.7	12.3	11.4
5.00	53.4	64.1	84.9		9.36	11.7	11.9	11.4
5.01	53.3	63.6	85.2		9.38	11.6	11.6	11.4
5.03	53.1	63.1	85.4		9.39	11.5	11.4	11.4
5.04	52.9	62.6	85.4		9.40	11.4	11.5	11.4
5.05	52.6	62.1	85.5		9.41	11.3	11.7	11.4
5.06	52.4	61.6	85.4		9.43	11.2	12.0	11.4
5.08	52.1	61.0	85.4		9.44	11.1	12.3	11.4
5.09	51.9	60.4	85.3		9.45	11.0	12.4	11.3
5.10	51.6	59.7	85.2		9.46	10.9	12.4	11.3
5.11	51.4	59.0	85.1		9.48	10.8	12.3	11.3
5.13	51.2	58.3	85.0		9.49	10.7	12.2	11.3
5.14	50.9	57.6	84.9		9.50	10.6	11.9	11.3
5.15	50.6	57.0	84.8		9.51	10.5	11.8	11.2
5.16	50.3	56.5	84.6		9.53	10.5	11.6	11.2
5.18	50.0	55.9	84.4		9.54	10.4	11.5	11.3
5.19	49.7	55.3	84.2		9.55	10.4	11.6	11.3
5.20	49.5	54.7	84.1		9.56	10.4	11.7	11.3
5.21	49.3	54.1	83.9		9.58	10.4	11.8	11.3
5.23	49.2	53.5	83.6		9.59	10.5	12.0	11.3
5.24	49.2	53.0	83.4		9.60	10.5	12.2	11.4
5.25	49.2	52.5	83.1		9.61	10.6	12.3	11.5
5.26	49.2	52.0	82.9		9.63	10.6	12.5	11.5
5.28	49.2	51.7	82.7		9.64	10.6	12.6	11.6
5.29	49.3	51.3	82.6		9.65	10.6	12.6	11.7
5.30	49.4	51.1	82.4		9.66	10.6	12.5	11.8
5.31	49.5	50.8	82.4		9.68	10.6	12.4	11.9

Table A.2: Continued

Time (ms)	Helium	Hydrogen	Air		Time (ms)	Helium	Hydrogen	Air
5.33	49.8	50.5	82.3		9.69	10.5	12.3	11.9
5.34	50.0	50.1	82.2		9.70	10.4	12.1	12.0
5.35	50.2	49.6	82.1		9.71	10.2	12.0	12.0
5.36	50.3	49.1	82.0		9.73	10.1	11.9	12.1
5.38	50.4	48.6	82.0		9.74	10.0	11.9	12.1
5.39	50.4	48.1	82.1		9.75	9.9	11.8	12.1
5.40	50.4	47.7	82.2		9.76	9.8	11.8	12.1
5.41	50.3	47.4	82.3		9.78	9.8	11.9	12.1
5.43	50.1	47.1	82.4		9.79	9.7	11.9	12.1
5.44	49.9	46.9	82.6		9.80	9.7	11.8	12.1
5.45	49.7	46.6	82.7		9.81	9.7	11.8	12.1
5.46	49.5	46.3	82.7		9.83	9.7	11.8	12.1
5.48	49.2	46.1	82.7		9.84	9.7	11.7	12.1
5.49	48.9	45.8	82.7		9.85	9.8	11.7	12.1
5.50	48.6	45.6	82.7		9.86	9.8	11.7	12.1
5.51	48.4	45.4	82.7		9.88	9.8	11.7	12.1
5.53	48.2	45.2	82.7		9.89	9.9	11.8	12.1
5.54	48.2	45.0	82.6		9.90	9.9	11.8	12.1
5.55	48.2	44.7	82.6		9.91	9.8	12.0	12.1
5.56	48.2	44.4	82.6		9.93	9.8	12.1	12.1
5.58	48.3	44.0	82.5		9.94	9.8	12.3	12.1
5.59	48.5	43.6	82.5		9.95	9.8	12.6	12.1
5.60	48.5	43.3	82.5		9.96	9.8	12.8	12.0
5.61	48.5	43.0	82.4		9.98	9.8	12.9	12.0
5.63	48.5	42.7	82.4		9.99	9.8	12.9	12.0
5.64	48.4	42.6	82.3		10.00	9.8	12.7	11.9
5.65	48.2	42.4	82.2		10.01	9.8	12.4	11.9
5.66	48.2	42.2	82.0		10.03	9.7	11.9	11.9
5.68	48.2	42.0	81.9		10.04	9.7	11.4	11.8
5.69	48.2	41.8	81.7		10.05	9.6	11.0	11.8
5.70	48.2	41.7	81.7		10.06	9.6	10.6	11.8
5.71	48.2	41.5	81.6		10.08	9.5	10.2	11.8
5.73	48.2	41.4	81.5		10.09	9.4	10.0	11.8
5.74	48.2	41.3	81.4		10.10	9.3	9.9	11.8
5.75	48.1	41.1	81.2		10.11	9.3	9.8	11.8
5.76	48.0	40.9	81.1		10.13	9.2	9.8	11.8
5.78	47.8	40.7	81.0		10.14	9.1	9.8	11.7
5.79	47.5	40.4	80.9		10.15	9.1	9.8	11.7
5.80	47.1	40.2	80.9		10.16	9.1	9.7	11.6
5.81	46.7	40.0	80.9		10.18	9.0	9.6	11.6
5.83	46.3	39.7	81.0		10.19	8.9	9.5	11.6
5.84	45.9	39.5	81.0		10.20	8.8	9.3	11.6
5.85	45.7	39.3	81.0		10.21	8.8	9.1	11.6
5.86	45.5	39.0	81.1		10.23	8.7	8.9	11.5
5.88	45.4	38.9	81.2		10.24	8.6	8.7	11.5
5.89	45.4	38.7	81.3		10.25	8.5	8.5	11.4
5.90	45.3	38.6	81.4		10.26	8.5	8.4	11.4
5.91	45.1	38.5	81.5		10.28	8.4	8.3	11.3
5.93	44.8	38.4	81.6		10.29	8.3	8.2	11.2
5.94	44.3	38.3	81.6		10.30	8.2	8.1	11.2
5.95	43.9	38.2	81.6		10.31	8.1	7.9	11.2
5.96	43.3	38.2	81.6		10.33	8.0	7.6	11.1
5.98	42.8	38.1	81.5		10.34	7.8	7.2	11.2
5.99	42.3	37.9	81.4		10.35	7.7	6.8	11.2

Table A.2: Continued

Time (ms)	Helium	Hydrogen	Air		Time (ms)	Helium	Hydrogen	Air
6.00	41.9	37.8	81.3		10.36	7.4	6.5	11.2
6.01	41.4	37.6	81.2		10.38	7.2	6.1	11.2
6.03	41.0	37.4	81.2		10.39	6.9	5.8	11.2
6.04	40.6	37.2	81.2		10.40	6.7	5.4	11.2
6.05	40.2	37.1	81.3		10.41	6.4	5.2	11.2
6.06	39.8	36.9	81.4		10.43	6.1	4.9	11.2
6.08	39.4	36.8	81.4		10.44	5.8	4.7	11.2
6.09	39.0	36.7	81.5		10.45	5.6	4.5	11.2
6.10	38.6	36.5	81.5		10.46	5.4	4.3	11.2
6.11	38.3	36.3	81.4		10.48	5.2	4.1	11.2
6.13	37.8	36.2	81.4		10.49	5.1	4.0	11.2
6.14	37.3	36.1	81.2		10.50	5.0	3.8	11.2
6.15	36.8	36.0	81.0		10.51	4.9	3.6	11.2
6.16	36.2	35.9	80.7		10.53	4.7	3.4	11.2
6.18	35.7	35.8	80.4		10.54	4.5	3.1	11.1
6.19	35.3	35.7	80.1		10.55	4.3	2.8	11.1
6.20	34.8	35.7	79.6		10.56	4.0	2.5	11.0
6.21	34.4	35.6	79.3		10.58	3.7	2.2	10.9
6.23	34.1	35.6	78.9		10.59	3.5	1.8	10.8
6.24	33.8	35.7	78.5		10.60	3.2	1.4	10.7
6.25	33.6	35.9	78.0		10.61	2.9	1.1	10.6
6.26	33.4	36.1	77.6		10.63	2.6	0.8	10.5
6.28	33.2	36.4	77.2		10.64	2.4	0.5	10.5
6.29	33.0	36.7	76.8		10.65	2.1	0.3	10.4
6.30	32.7	36.9	76.4		10.66	1.8	0.1	10.4
6.31	32.5	37.2	76.0		10.68	1.6	-0.1	10.4
6.33	32.3	37.4	75.6		10.69	1.3	-0.3	10.5
6.34	32.2	37.6	75.1		10.70	1.1	-0.5	10.6
6.35	32.1	37.8	74.6		10.71	0.9	-0.8	10.7
6.36	31.9	38.0	74.1		10.73	0.7	-1.1	10.7
6.38	31.7	38.3	73.6		10.74	0.5	-1.4	10.8
6.39	31.5	38.5	73.1		10.75	0.2	-1.7	10.8
6.40	31.2	38.6	72.6		10.76	0.0	-2.0	10.8
6.41	30.9	38.8	72.1		10.78	-0.2	-2.2	10.7
6.43	30.6	38.8	71.7		10.79	-0.5	-2.4	10.7
6.44	30.3	38.9	71.1		10.80	-0.7	-2.5	10.6
6.45	30.1	38.9	70.8		10.81	-0.9	-2.5	10.5
6.46	29.8	38.9	70.2		10.83	-1.1	-2.4	10.4
6.48	29.5	38.9	69.6		10.84	-1.1	-2.2	10.3
6.49	29.2	38.8	69.0		10.85	-1.2	-1.9	10.2
6.50	28.9	38.6	68.5		10.86	-1.1	-1.6	10.0
6.51	28.6	38.4	68.1		10.88	-1.0	-1.3	9.8
6.53	28.2	38.2	67.6		10.89	-0.9	-1.0	9.7
6.54	28.0	37.9	67.1		10.90	-0.7	-0.8	9.5
6.55	27.7	37.6	66.6		10.91	-0.6	-0.6	9.4
6.56	27.5	37.2	66.1		10.93	-0.5	-0.5	9.3
6.58	27.3	36.8	65.7		10.94	-0.4	-0.4	9.2
6.59	27.1	36.5	65.5		10.95	-0.3	-0.4	9.2
6.60	27.0	36.2	65.1		10.96	-0.3	-0.4	9.1
6.61	26.8	35.8	64.7		10.98	-0.3	-0.4	9.1
6.63	26.7	35.5	64.3		10.99	-0.3	-0.4	9.0
6.64	26.6	35.1	63.9		11.00	-0.3	-0.5	8.8
6.65	26.5	34.8	63.5		11.01	-0.3	-0.5	8.7
6.66	26.4	34.5	63.1		11.03	-0.4	-0.6	8.5

Table A.2: Continued

Time (ms)	Helium	Hydrogen	Air		Time (ms)	Helium	Hydrogen	Air
6.68	26.4	34.2	62.6		11.04	-0.4	-0.5	8.2
6.69	26.2	33.9	62.3		11.05	-0.4	-0.5	8.0
6.70	26.1	33.7	61.8		11.06	-0.4	-0.5	7.8
6.71	25.9	33.4	61.3		11.08	-0.5	-0.5	7.5
6.73	25.7	33.1	60.8		11.09	-0.5	-0.6	7.3
6.74	25.4	32.8	60.3		11.10	-0.6	-0.6	7.1
6.75	25.3	32.4	59.8		11.11	-0.6	-0.8	6.9
6.76	25.1	32.0	59.3		11.13	-0.6	-0.9	6.8
6.78	24.9	31.6	58.8		11.14	-0.6	-1.0	6.6
6.79	24.8	31.3	58.4		11.15	-0.5	-1.0	6.4
6.80	24.6	31.0	58.0		11.16	-0.4	-1.0	6.3
6.81	24.5	30.7	57.6		11.18	-0.3	-0.9	6.1
6.83	24.4	30.4	57.3		11.19	-0.2	-0.8	5.9
6.84	24.3	30.2	56.9		11.20	-0.2	-0.7	5.7
6.85	24.2	30.0	56.6		11.21	-0.2	-0.6	5.4
6.86	24.1	29.9	56.2		11.23	-0.3	-0.5	5.2
6.88	24.0	29.8	55.7		11.24	-0.3	-0.3	5.0
6.89	23.9	29.6	55.3		11.25	-0.4	-0.2	4.8
6.90	23.8	29.5	54.9		11.26	-0.4	-0.1	4.6
6.91	23.7	29.4	54.5		11.28	-0.3	0.1	4.5
6.93	23.6	29.2	54.1		11.29	-0.2	0.2	4.3
6.94	23.5	29.1	53.8		11.30	0.0	0.3	4.1
6.95	23.5	29.0	53.5		11.31	0.1	0.4	3.9
6.96	23.4	28.9	53.1		11.33	0.3	0.5	3.7
6.98	23.3	28.7	52.8		11.34	0.5	0.4	3.6
6.99	23.2	28.5	52.5		11.35	0.6	0.4	3.4
7.00	23.1	28.3	52.2		11.36	0.6	0.3	3.2
7.01	23.1	28.1	51.9		11.38	0.6	0.3	3.0
7.03	23.1	27.9	51.6		11.39	0.6	0.3	2.8
7.04	23.1	27.7	51.3		11.40	0.5	0.3	2.7
7.05	23.1	27.5	51.0		11.41	0.3	0.4	2.5
7.06	23.1	27.4	50.7		11.43	0.2	0.4	2.4
7.08	23.1	27.3	50.3		11.44	0.0	0.5	2.3
7.09	23.1	27.2	49.8		11.45	-0.1	0.4	2.2
7.10	23.1	27.1	49.4		11.46	-0.3	0.3	2.1
7.11	23.1	27.0	49.0		11.48	-0.4	0.2	1.9
7.13	23.1	26.8	48.5		11.49	-0.5	0.1	1.7
7.14	23.0	26.7	48.1		11.50	-0.6	-0.1	1.6
7.15	23.0	26.5	47.7		11.51	-0.6	-0.3	1.4
7.16	22.9	26.3	47.3		11.53	-0.6	-0.4	1.2
7.18	22.8	26.1	47.0		11.54	-0.6	-0.5	1.0
7.19	22.7	25.9	46.7		11.55	-0.6	-0.7	0.8
7.20	22.5	25.6	46.5		11.56	-0.6	-0.8	0.7
7.21	22.4	25.4	46.3		11.58	-0.6	-0.9	0.6
7.23	22.4	25.1	46.1		11.59	-0.5	-0.9	0.5
7.24	22.3	24.8	45.8		11.60	-0.5	-0.9	0.4
7.25	22.2	24.6	45.4		11.61	-0.5	-0.9	0.3
7.26	22.1	24.4	45.1		11.63	-0.5	-0.8	0.2
7.28	22.1	24.3	44.8		11.64	-0.4	-0.7	0.2
7.29	22.0	24.2	44.5		11.65	-0.3	-0.5	0.1
7.30	21.9	24.1	44.2		11.66	-0.2	-0.4	0.1
7.31	21.9	24.1	43.8		11.68	-0.1	-0.3	0.1
7.33	21.8	24.1	43.5		11.69	0.0	-0.2	0.0
7.34	21.7	24.1	43.1		11.70	0.1	-0.2	0.0

Table A.2: Continued

Time (ms)	Helium	Hydrogen	Air		Time (ms)	Helium	Hydrogen	Air
7.35	21.6	24.2	42.7		11.71	0.2	-0.1	0.0
7.36	21.5	24.3	42.3		11.73	0.3	-0.1	0.0
7.38	21.5	24.4	41.9		11.74	0.3	-0.1	0.0
7.39	21.4	24.4	41.6		11.75	0.3	0.0	0.1
7.40	21.3	24.4	41.2		11.76	0.4	0.0	0.1
7.41	21.3	24.4	40.9		11.78	0.4	0.0	0.2
7.43	21.3	24.3	40.4		11.79	0.4	0.0	0.2
7.44	21.3	24.1	40.1		11.80	0.4	0.0	0.2
7.45	21.3	23.9	39.7		11.81	0.4	0.0	0.2
7.46	21.2	23.7	39.4		11.83	0.4	0.0	0.2
7.48	21.2	23.5	39.0		11.84	0.3	0.1	0.2
7.49	21.1	23.2	38.5		11.85	0.2	0.1	0.2
7.50	21.0	22.9	38.2		11.86	0.1	0.2	0.2
7.51	20.9	22.7	37.9		11.88	-0.1	0.2	0.2
7.53	20.9	22.5	37.6		11.89	-0.2	0.2	0.1
7.54	20.8	22.3	37.3		11.90	-0.3	0.2	0.1
7.55	20.8	22.1	36.9		11.91	-0.5	0.1	0.0
7.56	20.7	22.0	36.7		11.93	-0.6	0.0	0.0
7.58	20.7	21.9	36.4		11.94	-0.7	-0.2	0.0
7.59	20.7	21.8	36.2		11.95	-0.7	-0.4	0.0
7.60	20.7	21.8	35.9		11.96	-0.7	-0.5	0.1
7.61	20.8	21.8	35.6		11.98	-0.7	-0.7	0.2
7.63	20.8	21.8	35.3		11.99	-0.7	-0.7	0.3
7.64	20.9	21.9	35.1		12.00	-0.7	-0.8	0.4
7.65	20.9	21.9	34.7					

Table A.3: Pressure time curves measured by seven sensors along the driven section. Figure 2.18 includes these data

Time (ms)	77 cm	137 cm	199 cm	260 cm	321 cm	382 cm	443 cm
0.000	0.04	0.00	0.01	0.02	0.00	0.00	-0.06
0.100	0.30	0.03	0.06	0.03	-0.06	-0.07	-0.18
0.199	1.02	-0.06	0.13	0.03	-0.06	0.03	-0.12
0.299	1.36	0.00	0.10	-0.04	-0.01	0.09	-0.16
0.399	2.80	0.00	0.04	-0.14	-0.01	-0.02	-0.04
0.499	4.77	-0.03	0.09	-0.15	0.00	0.03	-0.06
0.598	12.45	0.01	0.19	-0.23	0.00	0.00	-0.03
0.698	24.03	0.00	0.19	-0.32	0.03	0.04	-0.10
0.798	40.14	0.00	0.27	-0.27	0.12	0.09	-0.03
0.898	56.37	-0.07	0.22	-0.38	0.04	0.00	-0.07
0.997	55.82	-0.01	0.27	-0.14	0.01	0.06	-0.12
1.097	62.56	-0.06	0.27	-0.11	0.13	0.06	-0.03
1.197	63.23	0.07	0.09	0.08	0.06	0.09	0.06
1.297	70.43	0.15	0.15	0.12	0.03	0.15	0.06
1.396	66.51	0.32	0.27	0.02	0.06	0.00	0.13
1.496	75.02	0.48	0.31	-0.07	0.04	0.04	0.25
1.596	70.39	0.60	0.34	-0.38	0.06	0.10	0.41
1.696	70.71	0.60	0.31	-0.60	-0.01	0.06	0.60
1.795	74.70	1.37	0.33	-0.60	0.10	-0.02	0.66
1.895	72.32	-0.35	0.18	-0.23	0.09	0.00	0.76
1.995	72.71	0.93	0.10	0.06	0.03	0.04	0.95
2.095	76.00	6.69	0.07	0.23	0.13	0.03	1.02
2.194	74.60	42.27	-0.01	-0.03	0.03	0.04	1.04
2.294	73.72	67.41	0.09	-0.32	0.01	-0.02	1.02
2.394	75.01	56.26	0.24	-0.67	0.07	0.00	1.11
2.494	78.79	57.77	0.25	-0.81	0.03	0.07	0.98
2.593	76.31	66.53	0.03	-0.67	0.07	0.00	0.95
2.693	78.25	66.80	0.06	-0.41	0.00	0.07	0.69
2.793	80.58	64.99	0.48	-0.01	-0.01	0.01	0.54
2.893	81.85	66.12	0.21	0.14	0.01	-0.02	0.34
2.992	77.77	67.04	-0.48	0.06	0.10	0.10	0.38
3.092	75.88	66.80	0.70	-0.12	-0.03	0.03	0.31
3.192	79.22	67.16	-0.40	-0.21	0.07	0.09	0.45
3.292	81.85	68.61	3.08	-0.41	-0.01	0.07	0.55
3.391	73.31	68.99	-1.85	-0.58	0.04	0.04	0.67
3.491	80.20	67.42	7.54	-0.79	0.06	0.00	0.58
3.591	80.52	70.02	58.40	-0.75	0.10	-0.09	0.82
3.691	77.42	70.62	81.53	-0.47	0.09	0.04	0.76
3.790	70.99	71.43	66.22	0.24	0.09	0.01	0.93
3.890	63.82	73.98	68.62	0.32	0.15	0.01	0.99
3.990	70.67	72.43	79.56	0.54	0.15	0.01	0.85
4.090	71.58	71.90	64.88	-0.37	0.01	0.03	0.61
4.189	66.60	75.68	72.61	-0.57	-0.03	0.03	0.28
4.289	65.07	72.78	70.32	-1.72	0.00	0.07	0.09
4.389	63.28	73.80	70.99	0.69	0.10	0.03	0.06
4.489	62.18	70.92	76.46	-3.08	0.16	0.06	0.13
4.588	59.58	71.46	71.89	4.47	0.00	-0.03	0.50
4.688	55.08	73.37	73.49	-6.65	0.01	0.03	0.55
4.788	58.87	70.69	78.36	12.14	0.04	0.01	0.67
4.888	47.71	68.45	73.75	-7.24	-0.16	0.00	0.51
4.987	51.31	70.42	78.18	94.29	0.06	0.01	0.70
5.087	54.81	65.38	77.72	65.14	0.09	0.12	0.61

Table A.3: Continued

Time (ms)	77 cm	137 cm	199 cm	260 cm	321 cm	382 cm	443 cm
5.187	51.40	64.99	74.98	78.98	-0.13	-0.06	0.80
5.287	46.10	64.29	77.18	70.84	-0.12	0.03	0.82
5.386	49.24	64.32	78.83	62.24	0.38	0.01	1.01
5.486	44.97	61.02	77.88	74.91	-0.25	0.13	0.77
5.586	43.75	58.53	74.31	64.15	0.16	0.06	0.57
5.686	39.19	56.99	76.98	63.86	0.01	0.04	0.23
5.785	39.56	58.76	74.09	73.91	-0.92	0.10	-0.04
5.885	46.39	56.53	73.35	72.45	1.69	-0.30	0.26
5.985	38.79	55.83	72.43	75.24	-1.82	0.37	0.76
6.085	36.28	50.41	70.34	73.85	80.89	-0.75	-0.09
6.184	36.04	51.26	67.67	71.88	81.64	0.71	2.06
6.284	35.79	52.79	70.20	69.42	68.28	-1.15	-1.45
6.384	37.41	45.75	68.53	66.19	68.48	0.88	2.41
6.484	34.04	49.61	67.04	68.91	72.66	-0.94	-1.58
6.583	30.39	45.24	63.35	70.38	73.25	0.53	1.87
6.683	33.67	44.40	60.86	73.17	75.19	0.00	-1.04
6.783	32.60	45.50	61.50	75.63	78.34	-0.50	2.11
6.883	38.52	46.50	57.94	73.40	78.93	0.16	-1.72
6.982	30.94	42.17	59.39	69.97	75.35	1.34	2.74
7.082	27.05	41.82	58.21	71.56	75.97	-1.56	-3.68
7.182	26.84	41.47	52.33	64.00	76.88	0.45	2.95
7.282	26.82	35.30	54.78	64.03	77.04	3.82	-2.53
7.381	27.36	35.52	53.16	60.50	77.53	43.82	1.36
7.481	26.84	36.86	52.21	61.64	74.16	73.70	0.36
7.581	27.94	38.02	48.74	63.61	76.65	73.84	-0.94
7.681	29.44	34.12	45.06	59.87	75.21	64.96	1.20
7.780	25.07	34.01	46.84	60.85	75.00	79.50	-1.52
7.880	26.84	38.19	46.14	63.31	75.84	73.96	1.46
7.980	28.13	31.88	46.17	59.66	76.56	72.79	0.04
8.080	27.22	32.42	44.04	54.06	75.49	78.21	0.54
8.179	26.84	30.79	42.26	47.62	75.54	71.66	2.31
8.279	25.46	34.18	44.83	46.20	74.06	77.04	-4.35
8.379	28.25	31.55	39.02	47.19	70.76	73.07	4.96
8.479	30.12	31.05	39.26	48.19	70.58	73.55	-4.16
8.578	23.35	26.72	38.94	44.70	68.92	75.56	2.00
8.678	22.98	26.34	36.05	46.21	70.10	73.70	4.59
8.778	19.59	29.33	38.43	46.06	67.58	71.47	49.98
8.878	25.03	29.70	32.59	41.10	67.46	75.32	77.01
8.977	22.98	26.23	33.89	42.75	60.19	76.27	77.74
9.077	20.70	24.06	35.23	36.74	63.69	73.82	70.93
9.177	20.94	27.06	36.05	37.27	62.79	72.68	76.71
9.277	20.73	26.10	33.92	38.11	62.90	74.87	80.83
9.376	22.80	25.37	29.48	34.66	59.11	72.01	74.12
9.476	17.54	25.72	32.62	38.29	55.09	69.83	76.64
9.576	15.43	23.93	32.25	37.87	59.13	70.05	72.53
9.676	15.05	25.95	28.81	36.01	56.67	67.82	72.71
9.775	15.80	25.27	29.73	34.21	53.33	67.62	68.10
9.875	19.64	25.53	29.60	29.58	52.85	65.38	59.18
9.975	17.96	22.44	29.02	25.62	49.35	64.87	53.97
10.075	16.61	22.21	28.14	27.08	50.10	62.10	49.98
10.174	12.55	24.11	27.15	27.69	48.54	61.21	40.04
10.274	14.48	25.75	28.05	28.61	48.78	61.74	34.30
10.374	16.03	21.22	26.86	29.57	45.77	59.83	33.81
10.474	14.39	21.33	25.44	28.52	46.63	60.74	29.76

Table A.3: Continued

Time (ms)	77 cm	137 cm	199 cm	260 cm	321 cm	382 cm	443 cm
10.573	12.33	19.20	25.47	28.29	42.64	55.97	25.34
10.673	13.47	20.34	23.16	25.16	44.81	54.84	21.45
10.773	14.77	22.31	25.04	25.13	44.38	55.04	17.73
10.873	14.44	18.45	24.92	25.49	40.01	53.30	16.29
10.972	13.19	16.19	23.92	23.83	40.67	51.72	12.86
11.072	9.45	18.20	26.10	22.27	39.59	49.33	9.81
11.172	9.89	19.06	24.67	20.59	42.96	48.33	7.46
11.272	10.33	16.83	23.34	21.75	39.95	50.59	4.79
11.371	10.40	13.41	23.04	22.69	42.24	48.01	2.79
11.471	11.45	14.03	22.43	25.11	38.29	46.57	0.79
11.571	8.94	16.97	21.51	21.78	36.57	43.52	-1.33
11.671	10.33	14.61	21.54	18.55	39.27	43.60	-2.82
11.770	8.32	12.60	20.81	18.03	37.14	42.76	-4.38
11.870	10.36	15.39	21.85	16.26	38.57	44.30	-6.31
11.970	10.00	11.35	19.20	16.44	37.89	41.51	-6.33
12.070	8.41	11.74	19.87	19.51	35.35	40.20	-9.85
12.169	7.22	13.74	18.04	20.56	35.55	39.66	-12.11
12.269	5.99	10.96	17.52	18.45	32.60	37.76	-11.51
12.369	9.42	11.06	17.20	17.34	30.75	37.95	-13.36
12.469	5.83	10.07	16.16	17.59	31.47	35.32	-15.28
12.568	8.47	11.50	16.00	17.97	29.90	34.11	-16.01
12.668	5.47	11.18	15.82	15.91	30.66	29.24	-18.31
12.768	9.40	7.98	13.45	15.56	30.15	26.75	-17.80
12.868	6.20	8.67	14.70	17.88	30.28	24.26	-16.73
12.967	9.35	8.41	11.75	14.80	29.20	22.32	-14.74
13.067	4.68	6.69	11.96	15.58	29.75	21.22	-15.87
13.167	4.09	6.56	13.51	14.06	29.59	17.91	-17.37
13.267	7.70	8.10	12.75	13.55	29.49	15.94	-17.31
13.366	7.52	6.57	12.78	11.74	30.45	12.91	-14.33
13.466	10.85	5.83	11.26	11.90	27.04	11.34	-11.31
13.566	4.16	8.20	11.10	11.18	26.94	8.25	-12.98
13.666	5.07	6.50	10.47	10.01	26.58	6.33	-13.75
13.765	8.83	5.74	9.29	10.64	24.49	3.57	-15.34
13.865	7.89	4.65	9.47	9.31	25.05	2.58	-14.01
13.965	4.16	5.23	9.96	8.92	22.59	-0.18	-9.66
14.065	5.05	5.67	8.12	8.77	22.88	-0.86	-10.30
14.164	3.75	4.75	8.67	8.45	22.11	-1.17	-11.16
14.264	6.79	2.87	7.49	7.76	21.57	-2.26	-12.22
14.364	6.21	4.23	6.72	7.16	22.21	-5.94	-12.65
14.464	2.99	5.13	7.57	4.37	21.60	-4.16	-8.59
14.563	4.82	5.20	6.32	5.67	18.91	-5.94	-9.64
14.663	2.80	4.94	6.15	4.16	17.46	-7.05	-8.64
14.763	4.03	3.50	6.57	4.62	15.32	-6.96	-9.66
14.863	4.82	4.90	5.00	3.12	14.16	-9.16	-11.40
14.962	2.89	3.79	6.51	3.83	12.30	-10.84	-11.98
15.062	2.14	3.56	4.74	3.60	10.67	-12.82	-12.13
15.162	2.89	3.22	5.35	3.54	8.50	-13.95	-13.40
15.262	2.83	3.80	4.47	2.96	6.08	-15.50	-10.93
15.361	1.43	4.17	5.23	0.80	3.83	-16.62	-11.24
15.461	1.06	4.62	5.26	2.15	3.29	-16.77	-11.06
15.561	1.12	2.74	2.99	0.68	1.85	-19.08	-11.76
15.661	1.83	4.76	3.99	3.77	-0.78	-18.29	-12.95
15.760	1.76	2.78	2.61	1.74	-1.92	-20.50	-9.61
15.860	3.64	2.74	0.86	0.62	-3.37	-21.65	-8.68

Table A.3: Continued

Time (ms)	77 cm	137 cm	199 cm	260 cm	321 cm	382 cm	443 cm
15.960	-0.07	2.24	2.37	-2.34	-4.95	-21.62	-8.05
16.060	1.61	1.76	1.59	-2.49	-5.63	-22.31	-7.85
16.159	-0.01	0.89	2.20	-0.97	-6.61	-23.83	-8.86
16.259	2.25	1.97	2.13	-1.89	-8.16	-24.41	-8.17
16.359	0.01	1.66	1.67	-1.90	-9.94	-25.53	-8.69
16.459	-0.02	2.40	1.09	-3.09	-11.36	-26.15	-8.55
16.558	1.33	0.41	0.21	-2.52	-12.02	-27.25	-9.37
16.658	2.77	-0.95	0.52	-1.81	-12.88	-27.08	-11.21
16.758	1.24	0.50	2.31	-1.49	-14.57	-28.27	-11.84
16.858	1.13	0.58	1.50	-3.74	-15.05	-30.38	-11.15
16.957	2.47	0.38	0.54	-5.44	-16.23	-29.94	-12.83
17.057	-0.02	-1.65	0.39	-7.83	-17.88	-30.57	-12.36
17.157	-1.15	-0.47	0.48	-10.63	-18.95	-31.34	-13.30
17.257	0.51	0.16	0.71	-11.91	-18.76	-31.46	-13.12
17.356	1.62	-0.39	-0.30	-11.28	-19.73	-32.64	-12.29
17.456	1.56	-1.66	-0.39	-11.57	-21.59	-32.46	-11.57
17.556	1.02	-2.62	0.64	-13.35	-22.19	-34.55	-10.71
17.656	1.03	-2.00	-0.63	-14.34	-21.82	-34.30	-10.36
17.755	2.22	-1.58	-0.25	-15.65	-23.32	-33.30	-10.96
17.855	0.99	-0.79	-0.68	-16.39	-23.54	-31.35	-10.68
17.955	1.48	-2.29	-2.28	-17.73	-24.65	-27.83	-10.33
18.055	1.03	-1.83	-1.88	-18.70	-24.86	-27.77	-10.68
18.154	2.10	-1.45	-1.30	-19.24	-26.68	-27.02	-12.89
18.254	1.73	-1.23	-1.97	-20.43	-26.84	-26.09	-11.98
18.354	3.75	-2.49	-3.04	-20.31	-27.72	-26.88	-12.92
18.454	3.39	-2.88	-3.40	-21.61	-27.76	-28.03	-12.10
18.553	1.36	-3.70	-2.45	-22.79	-27.57	-27.80	-12.32
18.653	1.91	-2.85	-3.71	-23.92	-28.96	-26.91	-11.65
18.753	2.34	-0.26	-4.38	-24.75	-28.63	-26.29	-11.81
18.853	1.54	-0.66	-6.20	-25.04	-29.39	-27.52	-11.82
18.952	2.86	-2.60	-6.78	-26.47	-30.53	-25.23	-10.55
19.052	3.09	-3.36	-6.90	-27.51	-30.82	-23.54	-9.67
19.152	4.01	-2.18	-8.51	-27.84	-31.95	-24.44	-9.53
19.252	2.98	-2.54	-9.43	-27.65	-32.63	-22.45	-9.94
19.351	3.35	-4.29	-10.74	-27.87	-33.18	-24.27	-9.66
19.451	3.09	-4.98	-11.40	-28.85	-34.06	-25.69	-9.64
19.551	1.06	-1.42	-12.13	-29.95	-34.40	-24.38	-9.86
19.651	1.42	-1.46	-12.92	-31.82	-34.47	-24.33	-10.46
19.750	3.88	-1.88	-14.03	-32.68	-33.96	-23.98	-10.90
19.850	4.76	-3.03	-14.38	-33.23	-34.85	-24.54	-9.42
19.950	2.87	-2.90	-15.04	-34.20	-34.74	-23.83	-10.59

Table A.4: Membrane thickness characterization data. Driven pressure and efficiency measured as functions of driver pressure (left column) and membrane thickness (0.127, 0.178, and 0.254 mm). Figure 2.20 includes these data.

	Driven Pressure (kPa)			**Efficiency (Driven/Driver)**		
Driver Pressure	**Membrane Thickness (mm)**			**Membrane Thickness (mm)**		
(kPa)	**0.127**	**0.178**	**0.254**	**0.127**	**0.178**	**0.254**
103.35	7.58			0.073		
172.25	51.12	40.21		0.297	0.233	
241.15	124.98	77.22	24.59	0.518	0.320	0.102
289.38	129.18			0.446		
310.05		146.98	75.22		0.474	0.243
323.83	154.80			0.478		
378.95		198.74	132.07		0.524	0.349
447.85		170.03	137.18		0.380	0.306
516.75		220.47	172.25		0.427	0.333
620.10			228.49			0.368

APPENDIX B

CHAPTER 3 DATA TABLES

Table B.1: Animal IDs with associated group and blast level with key blast parameters.

Animal ID	Eyes	Group	Blast Level	Max Pressure (PSI)	+ Phase (ms)	Net Impulse (PSI*s)
130618-1	Histology	Char	Blast	30.729	7.396	0.184
130618-2	Histology	Char	Blast	Not Recorded	Not Recorded	Not Recorded
130621-1	Histology	8 Week	Blast	Not Recorded	Not Recorded	Not Recorded
130621-2	Histology	4 Week	Blast	34.509	7.490	0.167
130621-3	Histology	8 Week	Blast	38.649	7.651	0.180
131017-1	Histology	1 Day	Control	N/A	N/A	N/A
131017-2	Histology	1 Day	Control	N/A	N/A	N/A
131017-3	Histology	1 Day	Control	N/A	N/A	N/A
131107-1	Histology	1 Week	Control	N/A	N/A	N/A
131107-2	Histology	1 Week	Control	N/A	N/A	N/A
131107-3	Histology	1 Week	Control	N/A	N/A	N/A
131127-1	Histology	1 Week	Control	N/A	N/A	N/A
131127-2	Histology	1 Week	Control	N/A	N/A	N/A
131127-3	Histology	1 Week	Control	N/A	N/A	N/A
131210-1	Histology	1 Week	Blast	36.808	7.778	0.201
131210-2	Histology	1 Week	Blast	35.281	7.622	0.207
131210-3	Histology	1 Week	Blast	36.366	7.607	0.203
140121-1	Histology	8 Week	Blast	30.744	7.591	0.189
140121-2	Histology	8 Week	Blast	33.670	7.510	0.195
140121-3	Histology	8 Week	Blast	34.158	7.470	0.193
140130-1	Histology	4 Week	Blast	36.748	7.667	0.206
140130-2	Histology	4 Week	Blast	33.771	7.641	0.195
140130-3	Histology	4 Week	Blast	33.019	7.688	0.193
140212-1	Histology	1 Day	Control	N/A	N/A	N/A
140212-2	Histology	1 Day	Control	N/A	N/A	N/A
140212-3	Histology	1 Day	Control	N/A	N/A	N/A
140226-1	Histology	1 Day	Blast	34.514	7.643	0.202
140226-2	Histology	1 Day	Blast	35.534	7.666	0.204
140226-3	Histology	1 Day	Blast	Not Recorded	Not Recorded	Not Recorded
140319-1	Histology	8 Week	Control	N/A	N/A	N/A
140319-2	Histology	8 Week	Control	N/A	N/A	N/A
140319-3	Histology	8 Week	Control	N/A	N/A	N/A
140326-1	Histology	4 Week	Control	N/A	N/A	N/A
140326-2	Histology	4 Week	Control	N/A	N/A	N/A
140326-3	Histology	4 Week	Control	N/A	N/A	N/A
140508-1	Vitreous	1 Week	Control	N/A	N/A	N/A
140508-2	Vitreous	1 Week	Control	N/A	N/A	N/A
140508-3	Vitreous	1 Week	Control	N/A	N/A	N/A
140508-4	Vitreous	1 Week	Control	N/A	N/A	N/A

Table B.1: Continued

Animal ID	Eyes	Group	Blast Level	Max Pressure (PSI)	+ Phase (ms)	Net Impulse (PSI*s)
140520-1	Vitreous	1 Day	Control	N/A	N/A	N/A
140520-2	Vitreous	1 Day	Control	N/A	N/A	N/A
140520-3	Vitreous	1 Day	Control	N/A	N/A	N/A
140520-4	Vitreous	1 Day	Control	N/A	N/A	N/A
140529-1	Vitreous	4 Week	Blast	32.515	6.717	0.184
140529-2	Vitreous	4 Week	Blast	36.422	8.026	0.182
140529-3	Vitreous	4 Week	Blast	34.833	7.918	0.184
140529-4	Vitreous	4 Week	Blast	32.916	7.525	0.191
140604-1	Vitreous	1 Week	Blast	37.750	7.458	0.207
140604-2	Histology	1 Week	Blast	34.196	7.660	0.188
140604-3	Histology	1 Week	Blast	33.840	7.385	0.181
140617-1	Histology	1 Day	Blast	36.206	7.462	0.188
140617-2	Histology	1 Day	Blast	35.946	7.393	0.195
140617-3	Vitreous	1 Day	Blast	36.636	7.464	0.186
140617-4	Vitreous	1 Day	Blast	35.742	7.372	0.193
141104-1	Vitreous	4 Week	Blast	Not Recorded	Not Recorded	Not Recorded
141104-2	Vitreous	4 Week	Blast	Not Recorded	Not Recorded	Not Recorded
141111-1	Vitreous	8 Week	Blast	34.252	6.264	0.159
141111-2	Vitreous	8 Week	Blast	32.007	7.030	0.164
141111-3	Vitreous	8 Week	Blast	31.707	6.353	0.171
141111-4	Died	8 Week	Blast	29.047	6.572	0.151
141111-5	Histology	8 Week	Blast	32.055	7.510	0.182
141120-1	Vitreous	1 Day	Blast	Not Recorded	Not Recorded	Not Recorded
141120-2	Vitreous	1 Day	Blast	31.341	6.667	0.164
141120-3	Vitreous	1 Day	Blast	30.529	6.662	0.160
141212-1	Vitreous	1 Week	Blast	29.009	6.185	0.168
141212-2	Vitreous	1 Week	Blast	29.915	5.918	0.193
141212-3	Vitreous	1 Week	Blast	28.984	6.485	0.166
141212-4	Vitreous	1 Week	Blast	31.670	6.602	0.160
141212-5	Vitreous	1 Week	Blast	29.728	5.954	0.172
141212-6	Vitreous	1 Week	Blast	28.721	6.337	0.169
150309-1	Vitreous	8 Week	Control	N/A	N/A	N/A
150309-2	Vitreous	8 Week	Control	N/A	N/A	N/A
150309-3	Vitreous	8 Week	Control	N/A	N/A	N/A
150309-4	Vitreous	8 Week	Control	N/A	N/A	N/A
150608-1	Vitreous	1 Day	Control	N/A	N/A	N/A
150608-2	Vitreous	1 Day	Control	N/A	N/A	N/A
150608-3	Vitreous	1 Day	Control	N/A	N/A	N/A
150608-4	Vitreous	1 Day	Control	N/A	N/A	N/A
150716-1	Died	8 Week	Blast	N/A	N/A	N/A
150716-2	Vitreous	8 Week	Blast	29.130	6.007	0.180
150716-3	Vitreous	8 Week	Blast	28.921	6.567	0.164
150716-4	Vitreous	8 Week	Blast	33.182	6.934	0.165
150716-C1	Vitreous	8 Week	Control	N/A	N/A	N/A
150716-C2	Vitreous	8 Week	Control	N/A	N/A	N/A
150716-C3	Vitreous	8 Week	Control	N/A	N/A	N/A
150716-C4	Vitreous	8 Week	Control	N/A	N/A	N/A
160414-4	Histology	1 Week	Blast	Not Recorded	Not Recorded	Not Recorded
160414-5	Died	1 Week	Blast	Not Recorded	Not Recorded	Not Recorded
160414-6	Died	1 Week	Blast	Not Recorded	Not Recorded	Not Recorded
160613-1	Histology	1 Week	Blast	Not Recorded	Not Recorded	Not Recorded
160613-2	Histology	1 Week	Blast	Not Recorded	Not Recorded	Not Recorded

Table B.2: Contrast sensitivity test data for blast exposed animals.

Animal ID	Base	1 Day	1 Wk	2 Wk	3 Wk	4 Wk	5 Wk	6 Wk	7 Wk	8 Wk
130621-1	0.152	0.144	0.202	0.273	0.245	0.217	0.240	0.221	0.234	0.278
130621-2	0.202	0.104	0.222	0.356	0.236	0.327				
130621-3	0.227	0.084	0.142	0.168	0.104	0.147	0.181	0.204	0.279	0.144
131210-1	0.217	0.364	0.235							
131210-2	0.244	0.291	0.185							
131210-3	0.273	0.412	0.185							
140121-1	0.199	0.210	0.266	0.273	0.244	0.221	0.273	0.237	0.213	0.232
140121-2	0.222	0.311	0.245	0.258	0.309	0.260	0.348	0.239	0.291	0.253
140121-3	0.162	0.194	0.233	0.320	0.247	0.173	0.297	0.203	0.229	0.231
140130-1	0.211	0.265	0.315	0.248	0.246	0.275				
140130-2	0.257	0.266	0.325	0.262	0.251	0.266				
140130-3	0.232	0.299	0.362	0.336	0.272	0.234				
140226-1	0.240									
140226-2	0.140	0.243								
140226-3	0.233	0.299								
140529-1	0.306	0.370	0.290	0.330	0.390	0.332	.			
140529-2	0.263	0.336	0.264	0.294	0.310	0.317				
140529-3	0.246	0.278	0.281	0.246	0.257	0.324				
140529-4	0.268	0.259	0.351	0.288	0.210	0.281				
140604-1	0.217	0.360	0.267							
140604-2	0.327	0.298	0.357							
140604-3	0.229	0.248	0.244							
140617-1	0.323	0.385								
140617-2	0.252	0.254								
140617-3	0.348	0.491								
140617-4	0.381	0.376								
141104-1	0.242	0.203	0.236	0.200	0.174	0.197				
141104-2	0.302	0.365	0.325	0.390	0.274	0.391				
141111-1	0.301	0.288	0.277	0.236	0.305	0.221	0.281		0.367	0.325
141111-2	0.205	0.374	0.268	0.291	0.264	0.281	0.325		0.368	0.470
141111-3	0.256	0.351	0.300	0.295	0.259	0.232	0.281		0.332	0.331
141111-4	0.239									
141111-5	0.223	0.296	0.276	0.290	0.304	0.341	0.312		0.315	0.342
141120-1	0.208	0.259								
141120-2	0.205	0.339								
141120-3	0.283	0.272								
141212-1	0.266	0.319	0.334							
141212-2	0.342	0.420	0.312							
141212-3	0.345	0.411	0.246							
141212-4	0.291	0.342	0.366							
141212-5	0.284	0.342	0.284							
141212-6	0.231	0.343	0.261							
150318-1	0.238	0.415	0.293	0.237	0.467	0.320	0.272	0.254		0.260
150318-2	0.220	0.205	0.222	0.266	0.361	0.341	0.320	0.308		0.303
150318-3	0.198	0.195	0.233	0.215	0.242	0.236	0.240	0.242		0.236
150318-4	0.283	0.266	0.277	0.308	0.307	0.258	0.325	0.281		0.248

Table B.3: Contrast sensitivity test data for control animals.

Animal ID	Base	1 Day	1 Wk	2 Wk	3 Wk	4 Wk	5 Wk	6 Wk	7 Wk	8 Wk
131017-2	0.195	0.490								
131017-3	0.190	0.248								
131107-1	0.237	0.291	0.192							
131107-2	0.325	0.352	0.266							
131107-3	0.239	0.215	0.158							
131127-1	0.175	0.204	0.204							
131127-2	0.172	0.209	0.208							
131127-3	0.225	0.240	0.249							
140212-1	0.210	0.278								
140212-2	0.179	0.188								
140212-3	0.222	0.184								
140319-1	0.347	0.370	0.208	0.246	0.241	0.307	0.297	0.310	0.336	0.296
140319-2	0.273	0.192	0.249	0.232	0.219	0.200	0.261	0.216	0.246	0.166
140319-3	0.246	0.233	0.239	0.250	0.153	0.224	0.235	0.199	0.183	0.236
140326-1	0.351	0.367	0.246	0.234	0.214	0.241				
140326-2	0.174	0.199	0.222	0.271	0.167	0.222				
140326-3	0.216	0.175	0.247	0.256	0.233	0.204				
140508-1	0.226	0.251	0.216							
140508-2	0.206	0.200	0.166							
140508-3	0.194	0.160	0.202							
140508-4	0.225	0.305	0.220							
140520-1	0.205	0.194								
140520-2	0.221	0.195								
140520-3	0.330	0.377								
140520-4	0.173	0.183								
150309-1	0.363	0.274	0.374	0.208	0.282	0.221	0.294	0.264	0.288	0.314
150309-2	0.281	0.270	0.243	0.261	0.209	0.239	0.294	0.279	0.292	0.299
150309-3	0.360	0.222	0.321	0.218	0.185	0.231	0.187	0.206	0.236	0.214
150309-4	0.277	0.239	0.264	0.219	0.220	0.292	0.202	0.210	0.254	0.249

Table B.4: Measurement of cornea and layer thicknesses in the right eye.

Animal ID	Base	1 Day	1 Wk	2 Wk	3 Wk	4 Wk	5 Wk	6 Wk	7 Wk	8 Wk
Overall Thickness (mm)										
140604-1	0.141	0.291	0.269							
140604-2	0.15	0.166	0.326							
140604-3	0.144	0.152	0.208							
141104-1	0.161	0.169	0.128	0.174	0.126					
141104-2	0.136	0.228	0.143	0.179	0.181	0.176				
141111-1	0.146		0.27	0.441	0.324	0.249	0.781	0.501		0.166
141111-2	0.148	0.137	0.161	0.161	0.141	0.145	0.116	0.176		0.192
141111-3	0.161	0.138	0.271	0.317	0.791	0.426	0.243	0.314		0.204
141111-5	0.159	0.31	0.264	0.774	0.173	0.235	0.2	0.18		0.18
141120-1	0.13	0.13								
141120-2	0.133	0.121								
141120-3	0.152	0.142								
141211-1	0.164	0.161	0.166							
141211-2	0.157	0.157	0.171							
141211-3	0.166	0.157	0.171							
141211-4	0.157	0.298	0.194							
141211-5	0.152	0.439	0.185							
141211-6	0.149	0.149	0.154							
150309-1	0.154	0.164	0.173	0.173	0.176	0.159	0.171	0.183	0.164	0.133
150309-2	0.161	0.204	0.492	0.154	0.157	0.149	0.171		0.188	0.18
150309-3	0.173	0.154	0.18	0.176	0.19	0.169	0.19		0.173	0.171
150309-4	0.135	0.197	0.154	0.137	0.118	0.14	0.145		0.154	0.154
150318-1	0.124	0.145	0.408	0.526	0.647	0.417	0.299	0.303		0.184
150318-2	0.159	0.126	0.138	0.15	0.143	0.136	0.152	0.155		0.154
150318-3	0.164	0.164	0.186	0.182	0.198	0.175	0.154	0.154		0.186
150318-4		0.17	0.149	0.149	0.137	0.165	0.128	0.161		0.17
160412-1	0.133	0.238	0.161	0.133	0.14	0.135				
160412-2	0.124	0.172	0.161	0.172		0.154				
160412-3	0.128	0.212	0.314	0.491	0.345	0.135				
160412-4	0.136	0.163	0.161							
160613-1	0.158	0.321	0.254							
160613-2	0.168	0.303	0.161							
Stromal Thickness (mm)										
140604-1	0.108	0.244	0.231							
140604-2	0.106	0.117	0.253							
140604-3	0.106	0.137	0.175							
141104-1	0.115	0.126	0.103	0.126	0.098					
141104-2	0.105	0.175	0.115	0.138	0.144	0.133				
141111-1	0.105		0.211	0.271	0.273	0.22	0.535	0.183		0.169
141111-2	0.104	0.099	0.123	0.116	0.116	0.111	0.085	0.129		0.136
141111-3	0.123	0.11	0.232	0.286	0.487	0.248	0.195	0.144		0.095
141111-5	0.124	0.255	0.222	0.58	0.232	0.205	0.169	0.143		0.134
141120-1	0.105	0.1								
141120-2	0.103	0.095								
141120-3	0.112	0.112								
141211-1	0.122	0.122	0.143							
141211-2	0.122	0.127	0.143							
141211-3	0.122	0.117	0.136							
141211-4	0.112	0.233	0.165							
141211-5	0.115	0.364	0.141							
141211-6	0.107	0.117	0.117							
150309-1	0.117	0.129	0.138	0.131	0.134	0.129	0.136	0.143	0.124	0.095
150309-2	0.131	0.169	0.355	0.122	0.127	0.115	0.141		0.15	0.138

Table B.4: Continued

Animal ID	Base	1 Day	1 Wk	2 Wk	3 Wk	4 Wk	5 Wk	6 Wk	7 Wk	8 Wk
150309-3	0.127	0.127	0.146	0.136	0.15	0.138	0.153		0.134	0.143
150309-4	0.105	0.165	0.124	0.11	0.095	0.105	0.117		0.129	0.119
150318-1	0.095	0.116	0.369	0.408	0.628	0.355	0.251	0.246		0.157
150318-2	0.117	0.087	0.101	0.112	0.108	0.099	0.114	0.116		0.108
150318-3	0.14	0.126	0.13	0.144	0.165	0.135	0.123	0.128		0.149
150318-4		0.13	0.107	0.109	0.107	0.126	0.1	0.116		0.133
160412-1	0.088	0.225	0.119	0.103	0.1	0.095				
160412-2	0.086	0.13	0.126	0.13		0.126				
160412-3	0.084	0.175	0.272	0.234	0.207	0.1				
160412-4	0.109	0.128	0.13							
160613-1	0.133	0.284	0.223							
160613-2	0.128	0.272	0.128							
Epithelial Thickness (mm)										
140604-1	0.033	0.047	0.038							
140604-2	0.044	0.049	0.073							
140604-3	0.042	0.015	0.033							
141104-1	0.046	0.043	0.025	0.048	0.028					
141104-2	0.031	0.053	0.028	0.041	0.037	0.043				
141111-1	0.041		0.059	0.17	0.061	0.1	0.266	0.328		0.041
141111-2	0.044	0.038	0.038	0.045	0.025	0.034	0.031	0.047		0.056
141111-3	0.038	0.028	0.039	0.031	0.113	0.145	0.106	0.17		0.109
141111-5	0.035	0.055	0.042	0.194	0.079	0.03	0.031	0.037		0.046
141120-1	0.025	0.03								
141120-2	0.03	0.026								
141120-3	0.04	0.03								
141211-1	0.042	0.039								
141211-2	0.035	0.03	0.028							
141211-3	0.044	0.04	0.035							
141211-4	0.045	0.065	0.029							
141211-5	0.037	0.075	0.044							
141211-6	0.042	0.032	0.037							
150309-1	0.037	0.035	0.035	0.042	0.042	0.03	0.035	0.04	0.04	0.038
150309-2	0.03	0.035	0.137	0.032	0.03	0.034	0.03		0.038	0.042
150309-3	0.046	0.027	0.034	0.04	0.04	0.031	0.037		0.039	0.028
150309-4	0.03	0.032	0.03	0.027	0.023	0.035	0.028		0.025	0.035
150318-1	0.03	0.032	0.073	0.083	0.397	0.096	0.072	0.065		0.035
150318-2	0.042	0.032	0.042	0.04	0.038	0.035	0.041	0.042		0.034
150318-3	0.043	0.043	0.058	0.04	0.036	0.037	0.036	0.031		0.04
150318-4		0.039	0.037	0.045	0.037	0.044	0.041	0.042		0.037
160412-1	0.049	0.031	0.045	0.03	0.036	0.036				
160412-2	0.034	0.04	0.047	0.04		0.037				
160412-3	0.042	0.041	0.038	0.188	0.115	0.041				
160412-4	0.034	0.046	0.028							
160613-1	0.034	0.037	0.044							
160613-2	0.031	0.031	0.036							

Table B.5: Measurement of cornea and layer thicknesses in the left eye.

Animal ID	Base	1 Day	1 Wk	2 Wk	3 Wk	4 Wk	5 Wk	6 Wk	7 Wk	8 Wk
Overall Thickness (mm)										
140604-1	0.142	0.211	0.23							
140604-2	0.137	0.219	0.357							
140604-3	0.135	0.193	0.298							
141104-1	0.146	0.133	0.131	0.213	0.148					
141104-2	0.164	0.146	0.151	0.156	0.171	0.169				
141111-1	0.144	0.136	0.159	0.14	0.135	0.154	0.147	0.108		0.152
141111-2	0.141	0.137	0.159	0.166	0.176	0.145	0.166	0.145		0.166
141111-3	0.133	0.152	0.147	0.18	0.154	0.189	0.166	0.149		0.159
141111-5	0.152	0.123		0.161	0.166	0.173	0.178	0.152		0.173
141120-1	0.157	0.149								
141120-2	0.123	0.145								
141120-3	0.149	0.137								
141211-1	0.157	0.298	0.219							
141211-2	0.154	0.178	0.233							
141211-3	0.159	0.161	0.171							
141211-4	0.145	0.208	0.169							
141211-5		0.183	0.176							
141211-6	0.157	0.14	0.133							
150309-1	0.157	0.161	0.176	0.152	0.161	0.159	0.183	0.147	0.157	0.152
150309-2	0.161	0.207	0.308	0.154	0.154	0.147	0.161		0.171	0.14
150309-3	0.164	0.149	0.178	0.185	0.176	0.161	0.18		0.207	0.185
150309-4	0.142	0.171	0.166	0.149	0.147	0.169	0.166		0.18	0.173
150318-1	0.168	0.134	0.147	0.181	0.168	0.155	0.159	0.148		0.137
150318-2	0.161	0.145	0.128	0.163	0.166	0.164	0.155	0.145		0.166
150318-3	0.168	0.173	0.175	0.179	0.175	0.179	0.196	0.154		0.193
150318-4		0.191	0.151	0.179	0.172	0.156	0.151	0.172		0.177
160412-1	0.137	0.37	0.177	0.164	0.154	0.126				
160412-2	0.114	0.165	0.163	0.349	0.254	0.215				
160412-3	0.135	0.249	0.21	0.261	0.303	0.165				
160412-4	0.154	0.186	0.221							
160613-1	0.168	0.282	0.262							
160613-2	0.144	0.149	0.317							
Stromal Thickness (mm)										
140604-1	0.111	0.19	0.202							
140604-2	0.099	0.182	0.308							
140604-3	0.104	0.162	0.245							
141104-1	0.108	0.1	0.103	0.171	0.11					
141104-2	0.121	0.11	0.126	0.121	0.143	0.126				
141111-1	0.103	0.103	0.117	0.1	0.103	0.115	0.11	0.082		0.119
141111-2	0.105	0.106	0.123	0.121	0.13	0.116	0.121	0.1		0.127
141111-3	0.097	0.109	0.107	0.133	0.112	0.127	0.127	0.117		0.117
141111-5	0.11	0.098		0.124	0.119	0.124	0.124	0.112		0.131
141120-1	0.117	0.105								
141120-2	0.098	0.11								
141120-3	0.115	0.103								
141211-1	0.119	0.268	0.179							
141211-2	0.117	0.138	0.198							
141211-3	0.115	0.119	0.138							
141211-4	0.1	0.184	0.146							
141211-5	0.12	0.141	0.127							
141211-6	0.112	0.103	0.103							
150309-1	0.117	0.124	0.134	0.117	0.127	0.119	0.143	0.115	0.122	0.117
150309-2	0.124	0.181	0.232	0.127	0.127	0.122	0.117		0.127	0.112

Table B.5: Continued

Animal ID	Base	1 Day	1 Wk	2 Wk	3 Wk	4 Wk	5 Wk	6 Wk	7 Wk	8 Wk
150309-3	0.122	0.115	0.136	0.141	0.136	0.127	0.143		0.16	0.158
150309-4	0.105	0.131	0.127	0.112	0.115	0.129	0.127		0.141	0.138
150318-1	0.126	0.103	0.106	0.132	0.134	0.108	0.116	0.116		0.11
150318-2	0.119	0.105	0.105	0.126	0.123	0.117	0.112	0.112		0.13
150318-3	0.13	0.132	0.133	0.13	0.144	0.147	0.151	0.119		0.151
150318-4		0.147	0.119	0.144	0.123	0.121	0.119	0.133		0.144
160412-1	0.107	0.311	0.144	0.14	0.128	0.107				
160412-2	0.084	0.142	0.126	0.3	0.19	0.156				
160412-3	0.1	0.163	0.179	0.228	0.228	0.123				
160412-4	0.114	0.151	0.175							
160613-1	0.119	0.233	0.23							
160613-2	0.112	0.11	0.219							
Epithelial Thickness (mm)										
140604-1	0.031	0.021	0.028							
140604-2	0.038	0.037	0.049							
140604-3	0.031	0.031	0.053							
141104-1	0.038	0.033	0.028	0.042	0.038					
141104-2	0.043	0.036	0.025	0.035	0.028	0.043				
141111-1	0.041	0.033	0.042	0.04	0.032	0.039	0.037	0.026		0.033
141111-2	0.036	0.031	0.036	0.045	0.046	0.029	0.045	0.045		0.039
141111-3	0.036	0.043	0.04	0.047	0.042	0.062	0.039	0.032		0.042
141111-5	0.042	0.025		0.037	0.047	0.049	0.054	0.04		0.042
141120-1	0.04	0.044								
141120-2	0.025	0.035								
141120-3	0.034	0.034								
141211-1	0.038	0.03	0.04							
141211-2	0.037	0.04	0.035							
141211-3	0.044	0.042	0.033							
141211-4	0.045	0.024	0.023							
141211-5	0.04	0.042	0.049							
141211-6	0.045	0.037	0.03							
150309-1	0.04	0.037	0.042	0.035	0.034	0.04	0.04	0.032	0.035	0.035
150309-2	0.037	0.026	0.076	0.027	0.027	0.025	0.044		0.044	0.028
150309-3	0.042	0.034	0.042	0.044	0.04	0.034	0.037		0.047	0.027
150309-4	0.037	0.04	0.039	0.037	0.032	0.04	0.039		0.039	0.035
150318-1	0.048	0.039	0.035	0.04	0.036	0.034	0.042	0.04		0.033
150318-2	0.038	0.045	0.022	0.042	0.04	0.051	0.043	0.038		0.042
150318-3	0.043	0.041	0.043	0.042	0.031	0.041	0.052	0.043		0.041
150318-4		0.045	0.05	0.041	0.045	0.042	0.044	0.05		0.049
160412-1	0.028	0.071	0.031	0.035	0.029	0.023				
160412-2	0.033	0.029	0.037	0.05	0.059	0.069				
160412-3	0.037	0.1	0.041	0.033	0.077	0.041				
160412-4	0.041	0.043	0.052							
160613-1	0.031	0.047	0.045							
160613-2	0.035	0.034	0.102							

Table B.6: Tube pressure data from the driven section compared to IOP measured in the right and left eye during IOP studies.

Time (ms)	Tube (kPa)	Right (kPa)	Left (kPa)		Time (ms)	Tube (kPa)	Right (kPa)	Left (kPa)
0.0	0.15	0.02	-0.11		10.6	-2.29	-4.90	-7.48
0.2	-0.02	0.04	-0.15		10.8	-3.09	-4.85	-7.46
0.4	0.60	0.05	-0.08		11.0	-3.35	-4.44	-7.50
0.6	-0.08	0.10	-0.09		11.2	-2.42	-4.00	-7.57
0.8	-0.43	0.13	-0.11		11.4	-3.06	-3.91	-7.69
1.0	7.29	0.07	-0.01		11.6	-4.21	-3.91	-7.82
1.2	20.75	0.08	-0.12		11.8	-3.64	-3.98	-7.90
1.4	15.06	0.06	-0.14		12.0	-3.89	-4.02	-8.02
1.6	26.60	0.93	-0.26		12.2	-4.98	-4.02	-8.08
1.8	24.98	4.86	-1.52		12.4	-4.92	-4.07	-8.15
2.0	21.77	7.07	19.15		12.6	-4.95	-4.05	-8.15
2.2	24.79	7.51	19.10		12.8	-5.18	-4.12	-8.11
2.4	21.93	11.14	19.39		13.0	-5.14	-4.10	-8.13
2.6	19.40	14.05	18.90		13.2	-5.05	-3.74	-8.20
2.8	25.42	15.75	12.38		13.4	-4.79	-3.20	-8.27
3.0	24.69	18.05	5.51		13.6	-4.76	-2.94	-8.28
3.2	19.11	19.22	10.23		13.8	-4.89	-2.95	-8.25
3.4	22.15	16.57	13.13		14.0	-4.89	-3.16	-8.04
3.6	24.41	13.00	11.24		14.2	-5.34	-3.38	-7.72
3.8	19.89	9.80	-0.90		14.4	-5.59	-3.69	-7.41
4.0	18.09	6.41	-4.23		14.6	-5.11	-3.91	-7.12
4.2	17.47	0.02	-5.19		14.8	-4.89	-4.08	-6.74
4.4	17.25	-4.29	-6.46		15.0	-5.53	-4.03	-6.23
4.6	14.54	-5.78	-7.68		15.2	-5.24	-3.86	-5.85
4.8	11.70	-6.52	-8.05		15.4	-5.66	-3.78	-5.52
5.0	12.94	-6.14	-7.21		15.6	-5.66	-3.82	-5.06
5.2	11.99	-3.87	-5.11		15.8	-5.46	-3.80	-4.49
5.4	7.91	2.32	13.08		16.0	-5.46	-3.75	-3.56
5.6	9.06	3.90	12.28		16.2	-5.82	-3.70	-2.40
5.8	9.68	3.56	8.71		16.4	-5.85	-3.69	-0.48
6.0	6.87	2.13	4.18		16.6	-5.75	-3.84	1.07
6.2	5.66	0.32	1.56		16.8	-5.85	-3.95	1.05
6.4	5.99	-1.37	-0.13		17.0	-6.07	-3.99	0.71
6.6	5.27	-2.35	-1.60		17.2	-6.20	-3.98	0.23
6.8	4.36	-2.79	-2.43		17.4	-6.17	-4.01	-0.99
7.0	3.12	-2.87	-2.72		17.6	-6.33	-4.06	-2.22
7.2	2.92	-2.87	-3.04		17.8	-6.07	-4.04	-3.01
7.4	2.50	-2.85	-3.69		18.0	-6.33	-3.57	-3.33
7.6	1.22	-2.85	-4.34		18.2	-6.55	-3.06	-3.23
7.8	1.39	-2.73	-4.80		18.4	-6.49	-2.85	-2.96
8.0	1.19	-3.26	-5.34		18.6	-6.52	-2.99	-2.61
8.2	0.54	-3.65	-5.68		18.8	-6.55	-3.26	-2.57
8.4	0.34	-3.96	-6.01		19.0	-6.36	-3.49	-2.75
8.6	-0.08	-4.17	-6.05		19.2	-6.36	-3.58	-2.77
8.8	-0.37	-4.31	-5.92		19.4	-6.30	-3.54	-2.71
9.0	-0.79	-4.59	-6.01		19.6	-5.98	-3.47	-2.79
9.2	-0.62	-4.81	-6.27		19.8	-6.01	-3.47	-3.08
9.4	-1.23	-4.87	-6.66		20.0	-5.91	-3.53	-3.37
9.6	-1.65	-4.80	-6.98		20.2	-5.62	-3.64	-3.52
9.8	-1.43	-4.74	-7.20		20.4	-5.53	-3.67	-3.50
10.0	-1.94	-4.86	-7.33		20.6	-5.46	-3.59	-3.48

Table B.6: Continued

Time (ms)	**Tube (kPa)**	**Right (kPa)**	**Left (kPa)**		**Time (ms)**	**Tube (kPa)**	**Right (kPa)**	**Left (kPa)**
10.2	-2.39	-4.97	-7.35		20.8	-5.30	-3.54	-3.42
10.4	-2.20	-4.95	-7.42		21.0	-5.08	-3.43	-3.34

APPENDIX C

CHAPTER 4 DATA TABLES

Table C.1: Pressure-time blast load curves applied to models as shown in Figure 4.8.

Time(ms)	Pressure (kPa)				Time (ms)		Pressure (kPa)
	Baseline	**+2SDPress**	**-2SDPress**		**-2SDTime**	**+2SDTime**	
0	11.1	13.9	8.3		0.0	0.0	11.1
0.2	142.4	178.0	106.8		0.2	0.2	142.4
0.4	131.2	164.0	98.4		0.5	0.3	131.2
0.6	201.5	251.9	151.1		0.7	0.5	201.5
0.8	176.0	220.1	132.0		0.9	0.7	176.0
1	150.8	188.5	113.1		1.2	0.8	150.8
1.2	152.9	191.1	114.7		1.4	1.0	152.9
1.4	161.8	202.2	121.3		1.7	1.1	161.8
1.6	147.9	184.9	110.9		1.9	1.3	147.9
1.8	146.6	183.3	110.0		2.1	1.5	146.6
2	159.1	198.9	119.3		2.4	1.6	159.1
2.2	151.9	189.9	113.9		2.6	1.8	151.9
2.4	162.5	203.1	121.9		2.8	2.0	162.5
2.6	148.7	185.8	111.5		3.1	2.1	148.7
2.8	141.3	176.6	106.0		3.3	2.3	141.3
3	131.1	163.9	98.4		3.5	2.5	131.1
3.2	123.7	154.6	92.8		3.8	2.6	123.7
3.4	116.7	145.8	87.5		4.0	2.8	116.7
3.6	112.8	141.0	84.6		4.2	3.0	112.8
3.8	102.8	128.5	77.1		4.5	3.1	102.8
4	96.0	120.0	72.0		4.7	3.3	96.0
4.2	92.8	116.1	69.6		5.0	3.4	92.8
4.4	82.9	103.6	62.2		5.2	3.6	82.9
4.6	75.2	94.0	56.4		5.4	3.8	75.2
4.8	74.9	93.6	56.2		5.7	3.9	74.9
5	65.3	81.6	49.0		5.9	4.1	65.3
5.2	64.4	80.5	48.3		6.1	4.3	64.4
5.4	61.4	76.8	46.1		6.4	4.4	61.4
5.6	53.9	67.4	40.5		6.6	4.6	53.9
5.8	47.5	59.4	35.7		6.8	4.8	47.5
6	42.9	53.6	32.1		7.1	4.9	42.9
6.2	39.8	49.8	29.9		7.3	5.1	39.8
6.4	34.0	42.5	25.5		7.6	5.2	34.0
6.6	26.4	33.0	19.8		7.8	5.4	26.4
6.8	23.6	29.5	17.7		8.0	5.6	23.6
7	19.9	24.8	14.9		8.3	5.7	19.9
7.2	15.5	19.4	11.6		8.5	5.9	15.5
7.4	13.2	16.6	9.9		8.7	6.1	13.2
7.6	7.0	8.8	5.3		9.0	6.2	7.0

Table C.1: Continued

Time(ms)	Pressure (kPa)				Time (ms)		Pressure (kPa)
	Baseline	+2SDPress	-2SDPress		-2SDTime	+2SDTime	
7.8	5.0	6.3	3.8		9.2	6.4	5.0
8	3.0	3.7	2.2		9.4	6.6	3.0
8.2	1.0	1.2	0.7		9.7	6.7	1.0
8.4	-5.2	-6.6	-3.9		9.9	6.9	-5.2
8.6	-6.1	-7.7	-4.6		10.1	7.1	-6.1
8.8	-7.5	-9.3	-5.6		10.4	7.2	-7.5
9	-9.6	-12.0	-7.2		10.6	7.4	-9.6
9.2	-13.2	-16.5	-9.9		10.9	7.5	-13.2
9.4	-15.3	-19.1	-11.5		11.1	7.7	-15.3
9.6	-16.5	-20.7	-12.4		11.3	7.9	-16.5
9.8	-20.2	-25.2	-15.1		11.6	8.0	-20.2
10	-22.0	-27.6	-16.5		11.8	8.2	-22.0
10.2	-23.9	-29.9	-17.9		12.0	8.4	-23.9
10.4	-25.1	-31.4	-18.8		12.3	8.5	-25.1
10.6	-26.4	-33.0	-19.8		12.5	8.7	-26.4
10.8	-27.7	-34.6	-20.8		12.7	8.9	-27.7
11	-31.5	-39.4	-23.7		13.0	9.0	-31.5
11.2	-34.4	-43.1	-25.8		13.2	9.2	-34.4
11.4	-33.7	-42.1	-25.3		13.5	9.3	-33.7
11.6	-36.6	-45.7	-27.4		13.7	9.5	-36.6
11.8	-37.9	-47.4	-28.5		13.9	9.7	-37.9
12	-41.1	-51.3	-30.8		14.2	9.8	-41.1
12.2	-41.4	-51.8	-31.1		14.4	10.0	-41.4
12.4	-40.9	-51.1	-30.7		14.6	10.2	-40.9
12.6	-43.3	-54.2	-32.5		14.9	10.3	-43.3
12.8	-45.2	-56.5	-33.9		15.1	10.5	-45.2
13	-47.8	-59.7	-35.8		15.3	10.7	-47.8
13.2	-48.2	-60.2	-36.1		15.6	10.8	-48.2
13.4	-48.3	-60.3	-36.2		15.8	11.0	-48.3
13.6	-50.0	-62.5	-37.5		16.0	11.2	-50.0
13.8	-51.0	-63.8	-38.3		16.3	11.3	-51.0
14	-51.9	-64.8	-38.9		16.5	11.5	-51.9
14.2	-52.4	-65.5	-39.3		16.8	11.6	-52.4
14.4	-53.5	-66.8	-40.1		17.0	11.8	-53.5
14.6	-54.9	-68.6	-41.1		17.2	12.0	-54.9
14.8	-54.8	-68.5	-41.1		17.5	12.1	-54.8
15	-51.4	-64.3	-38.6		17.7	12.3	-51.4
15.2	-46.7	-58.3	-35.0		17.9	12.5	-46.7
15.4	-46.3	-57.9	-34.7		18.2	12.6	-46.3
15.6	-51.6	-64.5	-38.7		18.4	12.8	-51.6
15.8	-49.0	-61.3	-36.8		18.6	13.0	-49.0
16	-47.2	-58.9	-35.4		18.9	13.1	-47.2
16.2	-47.3	-59.2	-35.5		19.1	13.3	-47.3
16.4	-50.2	-62.8	-37.7		19.4	13.4	-50.2
16.6	-47.4	-59.3	-35.6		19.6	13.6	-47.4
16.8	-44.2	-55.2	-33.1		19.8	13.8	-44.2
17	-46.9	-58.6	-35.1		20.1	13.9	-46.9
17.2	-45.4	-56.8	-34.1		20.3	14.1	-45.4
17.4	-46.5	-58.1	-34.8		20.5	14.3	-46.5
17.6	-44.9	-56.1	-33.7		20.8	14.4	-44.9
17.8	-44.8	-56.1	-33.6		21.0	14.6	-44.8
18	-42.6	-53.3	-32.0		21.2	14.8	-42.6
18.2	-42.2	-52.7	-31.6		21.5	14.9	-42.2

Table C.1: Continued

Time(ms)	Pressure (kPa)				Time (ms)		Pressure (kPa)
	Baseline	**+2SDPress**	**-2SDPress**		**-2SDTime**	**+2SDTime**	
18.4	-45.1	-56.4	-33.9		21.7	15.1	-45.1
18.6	-44.8	-56.0	-33.6		21.9	15.3	-44.8
18.8	-44.2	-55.3	-33.2		22.2	15.4	-44.2
19	-44.2	-55.3	-33.2		22.4	15.6	-44.2
19.2	-43.6	-54.5	-32.7		22.7	15.7	-43.6
19.4	-44.5	-55.6	-33.4		22.9	15.9	-44.5
19.6	-43.5	-54.3	-32.6		23.1	16.1	-43.5
19.8	-44.6	-55.7	-33.4		23.4	16.2	-44.6
20	-44.2	-55.3	-33.2		23.6	16.4	-44.2
20.2	-44.0	-55.0	-33.0		23.8	16.6	-44.0
20.4	-43.3	-54.1	-32.5		24.1	16.7	-43.3
20.6	-42.6	-53.2	-31.9		24.3	16.9	-42.6
20.8	-42.6	-53.2	-31.9		24.5	17.1	-42.6
21	-42.2	-52.8	-31.7		24.8	17.2	-42.2
21.2	-40.6	-50.7	-30.4		25.0	17.4	-40.6
21.4	-40.6	-50.8	-30.5		25.3	17.5	-40.6
21.6	-39.2	-49.0	-29.4		25.5	17.7	-39.2
21.8	-39.7	-49.6	-29.7		25.7	17.9	-39.7
22	-38.4	-47.9	-28.8		26.0	18.0	-38.4
22.2	-35.7	-44.6	-26.8		26.2	18.2	-35.7
22.4	-35.3	-44.1	-26.5		26.4	18.4	-35.3
22.6	-33.6	-42.0	-25.2		26.7	18.5	-33.6
22.8	-33.0	-41.3	-24.8		26.9	18.7	-33.0
23	-30.8	-38.6	-23.1		27.1	18.9	-30.8
23.2	-28.8	-36.0	-21.6		27.4	19.0	-28.8
23.4	-28.5	-35.7	-21.4		27.6	19.2	-28.5
23.6	-26.1	-32.6	-19.6		27.8	19.4	-26.1
23.8	-25.3	-31.6	-19.0		28.1	19.5	-25.3
24	-25.2	-31.5	-18.9		28.3	19.7	-25.2
24.2	-24.2	-30.2	-18.1		28.6	19.8	-24.2
24.4	-22.4	-28.0	-16.8		28.8	20.0	-22.4
24.6	-20.8	-26.0	-15.6		29.0	20.2	-20.8
24.8	-19.5	-24.3	-14.6		29.3	20.3	-19.5
25	-18.4	-23.0	-13.8		29.5	20.5	-18.4

Table C.2: Model outputs from six geometries under five loading conditions. Tables 4.6 and 4.7 and Figure 4.14 use these data.

Geometry	Load	Peak IOP (Pa)	AVG IOP (Pa)	Peak Cornea Strain	Peak Cornea Stress (Pa)	Peak Cornea Disp (mm)	Peak Lens Strain	Peak Lens Disp (mm)
Rat	Base Load	2.42E+5	1.00E+5	6.53E-3	1.12E+6	4.18E-5	2.97E-4	1.41E-5
	-2SD Pressure	1.81E+5	7.53E+4	4.66E-3	8.04E+5	3.02E-5	2.22E-4	1.07E-5
	+2SD Pressure	3.05E+5	1.26E+5	8.56E-3	1.45E+6	5.38E-5	3.71E-4	1.75E-5
	-2SD Time	1.69E+5	1.01E+5	6.12E-3	1.05E+6	2.91E-5	4.28E-4	1.04E-5
	+2SD Time	1.90E+5	9.76E+4	5.20E-3	8.94E+5	2.75E-5	2.06E-4	1.00E-5
Large Rat	Base Load	2.14E+5	1.00E+5	8.84E-3	1.51E+6	1.72E-4	7.40E-4	4.49E-5
	-2SD Pressure	1.62E+5	7.51E+4	6.51E-3	1.13E+6	1.28E-4	5.06E-4	3.38E-5
	+2SD Pressure	2.75E+5	1.25E+5	1.15E-2	1.65E+6	2.16E-4	9.31E-4	5.58E-5
	-2SD Time	2.01E+5	9.75E+4	7.87E-3	1.34E+6	1.21E-4	6.66E-4	4.41E-5
	+2SD Time	2.16E+5	1.00E+5	1.00E-2	1.67E+6	1.73E-4	8.31E-4	5.84E-5
Human	Base Load	1.93E+5	8.99E+4	7.66E-3	1.28E+6	1.04E-4	2.32E-4	7.45E-5
	-2SD Pressure	1.45E+5	6.74E+4	5.71E-3	9.65E+5	7.80E-5	2.00E-4	5.58E-5
	+2SD Pressure	2.40E+5	1.13E+5	9.61E-3	1.59E+6	1.30E-4	2.86E-4	9.31E-5
	-2SD Time	1.86E+5	8.72E+4	8.24E-3	1.37E+6	1.32E-4	2.76E-4	7.26E-5
	+2SD Time	1.90E+5	9.05E+4	7.65E-3	1.28E+6	1.18E-4	2.94E-4	7.52E-5
Small Cornea	Base Load	1.93E+5	1.03E+5	7.72E-3	1.30E+6	3.11E-5	2.44E-4	1.08E-5
	-2SD Pressure	1.45E+5	7.74E+4	5.60E-3	9.51E+5	2.31E-5	1.83E-4	8.11E-6
	+2SD Pressure	2.40E+5	1.29E+5	9.90E-3	1.64E+6	3.88E-5	3.05E-4	1.35E-5
	-2SD Time	1.91E+5	9.99E+4	7.56E-3	1.27E+6	2.81E-5	3.53E-4	1.45E-5
	+2SD Time	1.86E+5	1.04E+5	6.60E-3	1.11E+6	3.20E-5	1.65E-4	1.33E+5
Small Cornea & Lens	Base Load	1.77E+5	9.05E+4	8.62E-3	1.43E+6	3.21E-5	6.60E-5	1.85E-5
	-2SD Pressure	1.34E+5	6.78E+4	6.49E-3	1.09E+6	2.40E-5	4.97E-5	1.40E-5
	+2SD Pressure	2.19E+5	1.13E+5	1.07E-2	1.77E+6	4.01E-5	8.24E-5	2.28E-5
	-2SD Time	2.04E+5	8.76E+4	8.48E-3	1.41E+6	4.03E-5	1.18E-4	2.69E-5
	+2SD Time	1.71E+5	9.08E+4	9.30E-3	1.54E+6	4.26E-5	5.82E-5	2.52E-5
Small Lens	Base Load	2.04E+5	9.89E+4	5.85E-3	1.01E+6	4.01E-5	6.46E-5	2.94E-5
	-2SD Pressure	1.53E+5	7.42E+4	4.27E-3	7.40E+5	2.98E-5	4.86E-5	2.23E-5
	+2SD Pressure	2.54E+5	1.24E+5	7.49E-3	1.28E+6	5.07E-5	8.12E-5	3.64E-5
	-2SD Time	2.18E+5	9.60E+4	4.81E-3	8.34E+5	2.91E-5	1.10E-4	2.25E-5
	+2SD Time	2.07E+5	9.95E+4	4.21E-3	7.33E+5	2.93E-5	5.54E-5	2.22E-5

Table C.3: Simulation IOP results compared to scaling equation predictions. These data were presented in Figure 4.15

	Model Inputs		Model Output	IOP Predictions: IOP=a*P*dˆ(-0.0779)			
Simulation	**Globe Diameter (mm), d**	**Blast Pressure (kPa), P**	**Peak IOP (kPa)**	**a1**	**IOP(a1) (kPa)**	**a2**	**IOP(a2) (kPa)**
Rat	6.3	245	242	1.02	216	1.14	242
Rat +2SD Press	6.3	306	305	1.02	270	1.14	302
Rat -2SD Press	6.3	183	181	1.02	162	1.14	181
Large Rat	24.2	245	214	1.02	195	1.14	217
Large Rat +2SD Press	24.2	306	275	1.02	243	1.14	272
Large Rat -2SD Rat	24.2	183	162	1.02	146	1.14	163
Small Corn Lens	6.3	245	177	1.02	216	0.92	196
Small Corn Lens +2SD Press	6.3	306	219	1.02	270	0.92	245
Small Corn Lens -2SD Press	6.3	183	134	1.02	162	0.92	147
Human	24.2	245	193	1.02	195	0.92	176
Human +2SD Press	24.2	306	240	1.02	243	0.92	220
Human -2SD Press	24.2	183	145	1.02	146	0.92	132
Rabbit	16.0	245	190	1.02	201	0.92	182
Rabbit +2SD Press	16.0	306	237	1.02	251	0.92	227
Rabbit -2SD Press	16.0	183	143	1.02	151	0.92	136
Rabbit w Rabbit Lens	16.0	245	233	1.02	201	1.06	209
Rabbit w Rabbit Lens +2SD Press	16.0	306	291	1.02	251	1.06	261
Rabbit w Rabbit Lens -SD Press	16.0	183	174	1.02	151	1.06	157

REFERENCES

[1] A. J. Baker *et al.*, "Controlled blast exposure during forced explosive entry training and mild traumatic brain injury," *J. Trauma Acute Care Surg.*, vol. 71, no. 5, pp. S472–S477, 2011.

[2] G. C. Cockerham *et al.*, "Closed-globe injuries of the ocular surface associated with combat blast exposure," *Ophthalmology*, vol. 121, no. 11, pp. 2165–72, 2014.

[3] S. Zuckerman, "Experimental study of blast injuries to the lungs," *The Lancet*, vol. 236, no. 6104, pp. 219–224, 1940.

[4] M. Fallon, "Lung injury in the intact thorax with report of a case," *Br. J. of Surg.*, vol. 28, no. 109, pp. 39–49, 1940.

[5] G. Osborn, "Pulmonary concussion (blast)," *Br. Med J.*, vol. 1, no. 4187, p. 506, 1941.

[6] L. G. Bowen, E. R. Fletcher, and D. R. Richmond, "Estimate of man's tolerance to the direct effects of air blast," vol. 2113, 1968.

[7] W. A. Hadden, W. H. Rutherford, and J. D. Merrett, "The injuries of terrorist bombing: a study of 1532 consecutive patients," *Br. J. Surg.*, vol. 65, no. 8, pp. 525–31, 1978.

[8] E. Katz, B. Ofek, J. Adler, H. B. Abramowitz, and M. M. Krausz, "Primary blast injury after a bomb explosion in a civilian bus." *Ann. Surg.*, vol. 209, no. 4, p. 484, 1989.

[9] D. L. Coppel, "Blast injuries of the lungs," *Br. J. Surg.*, vol. 63, no. 10, pp. 735–737, 1976.

[10] T. C. Holdeman, "Invisible wounds of war: Psychological and cognitive injuries, their consequences, and services to assist recovery," *Psychiatr. Serv.*, vol. 60, no. 2, pp. 273–273, 2009.

[11] N. H. Guley *et al.*, "A novel closed-head model of mild traumatic brain injury using focal primary overpressure blast to the cranium in mice," *J. Neurotrauma*, vol. 33, no. 4, pp. 403–22, 2016.

[12] L. Zhang, R. Makwana, and S. Sharma, "Brain response to primary blast wave using validated finite element models of human head and advanced combat helmet," *Front. Neurol.*, vol. 4, p. 88, 2013.

[13] M. Liu *et al.*, "A novel rat model of blast-induced traumatic brain injury simulating different damage degree: implications for morphological, neurological, and biomarker changes," *Front. Cell. Neurosci.*, vol. 9, p. 168, 2015.

[14] S. Yeoh, E. D. Bell, and K. L. Monson, "Distribution of bloodbrain barrier disruption in primary blast injury," *Ann. Biomed. Eng.*, vol. 41, no. 10, pp. 2206–2214, 2013.

[15] V. D. Alphonse, "Injury biomechanics of the human eye during blunt and blast loading," M.S. thesis, Biomed. Eng., Virginia Polytech. Inst., Blacksburg, VA, 2012.

[16] R. Bhardwaj, K. Ziegler, J. Seo, K. T. Ramesh, and T. Nguyen, "A computational model of blast loading on the human eye," *Biomech. Model. Mechanobiol.*, vol. 13, no. 1, pp. 123–140, 2014.

[17] S. Bailoor, R. Bhardwaj, and T. D. Nguyen, "Effectiveness of eye armor during blast loading," *Biomech. Model. Mechanobiol.*, vol. 14, no. 6, pp. 1227–37, 2015.

[18] L. Esposito, C. Clemente, N. Bonora, and T. Rossi, "Modelling human eye under blast loading," *Comput. Methods Biomech. Biomed. Engin.*, vol. 18, no. 2, pp. 107–115, 2013.

[19] C. Bricker-Anthony, J. Hines-Beard, and T. S. Rex, "Eye-directed overpressure airwave-induced trauma causes lasting damage to the anterior and posterior globe: A model for testing cell-based therapies," *J. Ocul. Pharmacol. Ther.*, vol. 32, no. 5, pp. 286–95, 2016.

[20] J. Hines-Beard, J. Marchetta, S. Gordon, E. Chaum, E. E. Geisert, and T. S. Rex, "A mouse model of ocular blast injury that induces closed globe anterior and posterior pole damage," *Exp. Eye Res.*, vol. 99, pp. 63–70, 2012.

[21] T. Rossi *et al.*, "Primary blast injury to the eye and orbit: finite element modeling," *Invest. Ophthalmol. Vis. Sci.*, vol. 53, no. 13, pp. 8057–66, 2012.

[22] D. Ryan *et al.*, "The cornea after primary blast trauma," *Int. J. Ophthalmol. Clin. Res.*, vol. 2, no. 4, 2015.

[23] A. Sundaramurthy *et al.*, "Blast-induced biomechanical loading of the rat: An experimental and anatomically accurate computational blast injury model," *J. Neurotrauma*, vol. 29, no. 13, pp. 2352–2364, 2012.

[24] E. D. Weichel, M. H. Colyer, S. E. Ludlow, K. S. Bower, and A. S. Eiseman, "Combat ocular trauma visual outcomes during operations iraqi and enduring freedom," *Ophthalmol.*, vol. 115, no. 12, pp. 2235–45, 2008.

[25] J. S. Heier, R. W. Enzenauer, S. F. Wintermeyer, M. Delaney, and F. P. LaPiana, "Ocular injuries and diseases at a combat support hospital in support of operations desert shield and desert storm," *Arch. Ophthalmol.*, vol. 111, no. 6, pp. 795–8, 1993.

[26] A. Barak, A. Elhalel, J. Pikkel, E. Krauss, and B. Miller, "Incidence and severity of ocular and adnexal injuries during the second Lebanon war among Israeli soldiers and civilians," *Graefes Arch. Clin. Exp. Ophthalmol.*, vol. 249, no. 12, pp. 1771–4, 2011.

[27] J. J. Wang, P. Mitchell, and W. Smith, "Vision and low self-rated health: the blue mountains eye study," *Invest. Ophthalmol. Vis. Sci.*, vol. 41, no. 1, pp. 49–54, 2000.

[28] M. Langelaan *et al.*, "Impact of visual impairment on quality of life: a comparison with quality of life in the general population and with other chronic conditions," *Ophthalmic Epidemiol.*, vol. 14, no. 3, pp. 119–26, 2007.

[29] A. Hornblass, "Eye injuries in the military," *Int. Ophthalmol. Clin.*, no. 0020-8167, 1981.

[30] G. Treister, "Ocular casualties in the six-day war," *Am. J. Ophthalmol.*, vol. 68, no. 4, pp. 669–675, 1969.

[31] T. Y. Wong, M. B. Seet, and C. L. Ang, "Eye injuries in twentieth century warfare: a historical perspective," *Surv. Ophthalmol.*, vol. 41, no. 6, pp. 433–59, 1997.

[32] N. Shimkin, "Ophthalmic injuries in war," *Br. J. Ophthalmol.*, vol. 24, no. 6, p. 265, 1940.

[33] W. Stone, "Ocular injuries in the armed forces," *J. Am. Med. Assoc.*, vol. 142, no. 3, pp. 151–152, 1950.

[34] M. Belkin, G. Treister, and S. Dotan, "Eye injuries and ocular protection in the Lebanon war, 1982." *Isr. J. Med. Sci.*, vol. 20, no. 4, pp. 333–338, 1984.

[35] M. Belkin, "Ocular war injuries in the yom kippur war," *J. Ocul. Ther. Surg.*, vol. 2, pp. 40–9, 1983.

[36] S. Zukerman, "Ocular injuries resulting from the war," *Trans. Ophthalmol. Soc. UK*, vol. 61, pp. 45–50, 1941.

[37] S. Duke-Elder and P. MacFaul, *System of Ophthalmology*, vol. 14, pp. 49–56, 1972.

[38] J. Lada and F. A. Reister, *Medical Statistics in World War II.* Office of the Surgeon General, Dept. of the Army: for sale by the Supt. of Docs., US Govt. Print. Off., 1975.

[39] F. A. Reister, *Battle casualties and medical statistics: US Army experience in the Korean War.* Surgeon General, Dept. of the Army, 1973.

[40] G. M. Gombos, "Ocular war injuries in Jerusalem: During the 1967 Arab-Israeli conflict," *Am. J. Ophthalmol.*, vol. 68, no. 3, pp. 474–478, 1969.

[41] F. B. Hoefle, "Initial treatment of eye injuries: first corps area of Vietnam, 1966," *Arch. Ophthalmol.*, vol. 79, no. 1, pp. 33–35, 1968.

[42] A. B. Thach *et al.*, "Severe eye injuries in the war in iraq, 2003-2005," *Ophthalmol.*, vol. 115, no. 2, pp. 377–82, 2008.

[43] M. (Firm), "Idd-9-cm: International classification of diseases, 9th revision, clinical modification," *Washington, DC: U.S. Dept. of Health and Human Services, Public Health Service, Health Care Financing Administration*, 1996.

[44] R. Thomas, J. G. McManus, A. Johnson, P. Mayer, C. Wade, and J. B. Holcomb, "Ocular injury reduction from ocular protection use in current combat operations," *J. Trauma Acute Care Surg.*, vol. 66, no. 4, pp. S99–S103, 2009.

[45] M. Mines, A. Thach, S. Mallonee, L. Hildebrand, and S. Shariat, "Ocular injuries sustained by survivors of the Oklahoma city bombing," *Ophthalmol.*, vol. 107, no. 5, pp. 837–43, 2000.

[46] T. H. Mader *et al.*, "Ocular war injuries of the Iraqi insurgency, January-September 2004," *Ophthalmol.*, vol. 113, no. 1, pp. 97–104, 2006.

[47] N. Kapoor and K. J. Ciuffreda, "Vision disturbances following traumatic brain injury," *Curr. Treat. Options Neurol.*, vol. 4, no. 4, pp. 271–280, 2002.

[48] K. D. Brahm *et al.*, "Visual impairment and dysfunction in combat-injured servicemembers with traumatic brain injury," *Optom. Vis. Sci.*, vol. 86, no. 7, pp. 817–25, 2009.

[49] J. A. Stelmack, T. Frith, D. Van Koevering, S. Rinne, and T. R. Stelmack, "Visual function in patients followed at a veterans affairs polytrauma network site: an electronic medical record review," *Optometry*, vol. 80, no. 8, pp. 419–24, 2009.

[50] D. M. Lemonick, "Bombings and blast injuries: a primer for physicians," *Am. J. Clin. Med.*, vol. 8, no. 3, pp. 134–140, 2011.

[51] J. C. Morrison, "Elevated intraocular pressure and optic nerve injury models in the rat," *J. Glaucoma*, vol. 14, no. 4, pp. 315–7, 2005.

[52] S. Veleri *et al.*, "Biology and therapy of inherited retinal degenerative disease: insights from mouse models," *Dis. Model Mech.*, vol. 8, no. 2, pp. 109–29, 2015.

[53] A. I. Schneiderman, E. R. Braver, and H. K. Kang, "Understanding sequelae of injury mechanisms and mild traumatic brain injury incurred during the conflicts in Iraq and Afghanistan: Persistent postconcussive symptoms and posttraumatic stress disorder," *Am. J. Epidemiol.*, vol. 167, no. 12, pp. 1446–1452, 2008.

[54] H. Ayvazyan, "Structures to resist the effects of accidental explosions volume ii, blast, fragment, and shock loads," *U.S. Army Armament Res. Dev. Eng. Cent.*, vol. 2, p. 505, 1986.

[55] J. H. Choi *et al.*, "Pathophysiology of blast-induced ocular trauma in rats after repeated exposure to low-level blast overpressure," *Clin. Exp. Ophthalmol.*, pp. 52–73, 2014.

[56] K. Jones *et al.*, "Low-level primary blast causes acute ocular trauma in rabbits," *J. Neurotrauma*, 2015.

[57] N. Abdul-Karim *et al.*, "Post-blast explosive residue - a review of formation and dispersion theories and experimental research," *RSC Adv.*, vol. 4, pp. 54 354–54 371, 2014.

[58] F. Diaz Alonso *et al.*, "Characteristic overpressure-impulse-distance curves for vapour cloud explosions using the TNO multi-energy model," *J. Hazard. Mater.*, vol. 137, no. 2, pp. 734–41, 2006.

[59] J. Dewey, "The shape of the blast wave: Studies of the friedlander equation," in *21st Int. Symp. Mil. Aspects of Blast and Shock*, Conference Proceedings.

[60] J. M. Dewey, "Measurement of the physical properties of blast waves," in *Experimental Methods of Shock Wave Research*, O. Igra and F. Seiler, Eds. Cham: Springer International Publishing, 2016.

[61] R. Brun, "Shock tubes and shock tunnels: Design and experiments," *RTO-EN-AVT-162*, 2009.

[62] A. Holmberg, "Development and characterization of shock tubes for laboratory scale blast wave simulation," M.S. thesis, Univ. Nebraska, Eng. Mech., Lincoln, NE, 2010.

[63] A. Sundaramurthy and N. Chandra, "A parametric approach to shape field-relevant blast wave profiles in compressed-gas-driven shock tube," *Front. Neurol.*, vol. 5, p. 253, 2014.

[64] M. W. Courtney and A. C. Courtney, "A table-top blast driven shock tube." *Rev. Sci. Instrum.*, 2010.

[65] C. Bricker-Anthony, J. Hines-Beard, L. D'Surney, and T. S. Rex, "Exacerbation of blast-induced ocular trauma by an immune response," *J. Neuroinflammation*, vol. 11, p. 192, 2014.

[66] K. Mohan, "Retinal ganglion cell damage in an experimental rodent model of blast-mediated traumatic brain injury," *Invest. Ophthalmol. Vis. Sci.*, vol. 54, no. 5, pp. 3440–50, 2013.

[67] Y. Y. Zou *et al.*, "Primary blast injury-induced lesions in the retina of adult rats," *J. Neuroinflammation*, vol. 10, p. 79, 2013.

[68] N. N. Kleinschmit, "A shock tube technique for blast wave simulation and studies of flow structure interactions in shock tube blast experiments," M.S. thesis, Eng. Mech., Univ. Nebraska, Lincoln, NE, 2011.

[69] P. Carlucci, M. C., and J. Huidi, "Validation of abaqus explicit-cel for classes of problems of interest to the us army," *Simulia Customer Conference*, 2010.

[70] A. R. Amadio, M. W. Crofton, and E. L. Petersen, "Test-time extension behind reflected shock waves using CO2–He and C3H8–He driver mixtures," *Shock Waves*, vol. 16, no. 2, pp. 157–165, Dec 2006.

[71] J. D. Ritzel, "Shock tube solver," *Excel*, 2012.

[72] T. Kimura, H. Itoh, and K. Ogawa, "A study on shock tube flow with energy loss at the diaphragm section," *J.Jpn. Soc. Aeronaut. Space Sci.*, vol. 44, no. 512, pp. 550–555, 1996.

[73] R. A. Bauman and others., "An introductory characterization of a combat-casualty-care relevant swine model of closed head injury resulting from exposure to explosive blast," *J. Neurotrauma*, vol. 26, no. 6, pp. 841–60, 2009.

[74] G. A. Elder *et al.*, "Blast exposure induces post-traumatic stress disorder-related traits in a rat model of mild traumatic brain injury," *J. Neurotrauma*, vol. 29, no. 16, pp. 2564–2575, 2012.

[75] L. M. Dutca *et al.*, "Early detection of subclinical visual damage after blast-mediated TBI enables prevention of chronic visual deficit by treatment with P7C3-S243," *Invest. Ophthalmol. Vis. Sci.*, vol. 55, no. 12, pp. 8330–41, 2014.

[76] J. DeMar, K. Sharrow, M. Hill, J. Berman, T. Oliver, and J. Long, "Effects of primary blast overpressure on retina and optic tract in rats," *Front. Neurol.*, vol. 7, p. 59, 2016.

[77] F. G. Friedlander, "The diffraction of sound pulses. i. diffraction by a semi-infinite plane," *Proc. Roy. Soc. London. Series A. Math. Phys. Sci.*, vol. 186, no. 1006, pp. 322–344, 1946.

[78] G. C. Cockerham *et al.*, "Closed-eye ocular injuries in the Iraq and Afghanistan wars," *N. Engl. J. Med.*, vol. 364, no. 22, pp. 2172–2173, 2011.

[79] H. Cahill and J. Nathans, "The optokinetic reflex as a tool for quantitative analyses of nervous system function in mice: Application to genetic and drug-induced variation," *PLoS ONE*, vol. 3, no. 4, p. e2055, 2008.

[80] Y. Umino, E. Solessio, and R. B. Barlow, "Speed, spatial, and temporal tuning of rod and cone vision in mouse," *J. Neurosci.*, vol. 28, no. 1, pp. 189–98, 2008.

[81] D. Pelli, "The videotoolbox software for visual psychophysics: Transforming numbers into movies," *Spat. Vis.*, vol. 10, pp. 437–442, 1997.

[82] D. Brainiard, "The psychophysics toolbox," *Spat. Vis.*, vol. 10, pp. 433–436, 1997.

[83] W. J. Dixon and A. M. Mood, "A method for obtaining and analyzing sensitivity data," *J. Am. Stat. Assoc.*, vol. 43, no. 241, pp. 109–126, 1948.

[84] H. Levitt, "Transformed up-down methods in psychoacoustics," *J. Acoust. Soc. Am.*, vol. 49, no. 2, pp. Suppl 2:467+, 1971.

[85] J. Orlowski, W. Harmening, and H. Wagner, "Night vision in barn owls: Visual acuity and contrast sensitivity under dark adaptation," *J. Vis.*, vol. 12, no. 13, pp. 4–4, 2012.

[86] A. Petzold *et al.*, "A novel biomarker for retinal degeneration: vitreous body neurofilament proteins," *J. Neural Transm. (Vienna)*, vol. 116, no. 12, pp. 1601–6, 2009.

[87] C. Balaratnasingam, W. H. Morgan, L. Bass, S. J. Cringle, and D.-Y. Yu, "Time-dependent effects of elevated intraocular pressure on optic nerve head axonal transport and cytoskeleton proteins," *Invest. Ophthalmol. Vis. Sci.*, vol. 49, no. 3, pp. 986–999, 2008.

[88] M. Lin, E. Carlson, E. Diaconu, and E. Pearlman, "CXCL1/KC and CXCL5/LIX are selectively produced by corneal fibroblasts and mediate neutrophil infiltration to the corneal stroma in LPS keratitis," *J. Leukoc. Biol.*, vol. 81, no. 3, pp. 786–92, 2007.

[89] N. G. I. Center, "U.S. army improvised explosive device (IED) safe standoff distance cheat sheet,," *U.S. Army*, pp. 1–1, 2005.

[90] R. S. Heffner and H. E. Heffner, "Visual factors in sound localization in mammals," *J. Comp. Neurol.*, vol. 317, pp. 219–232, 1992.

[91] R. W. Massof and F. W. Chang, "A revision of the rat schematic eye," *Vis. Res.*, vol. 12, no. 5, pp. 793–796, 1972.

[92] D. C. Lozano and M. D. Twa, "Development of a rat schematic eye from in vivo biometry and the correction of lateral magnification in sd-oct imaging," *Invest. Ophthalmol. Vis. Sci.*, vol. 54, no. 9, pp. 6446–6455, 2013.

[93] W. M. S. Russell and R. L. Burch, *The principles of humane experimental technique.*, W. M. S. Russell and R. L. Burch, Eds., 1959.

[94] B. Coats and D. F. Shedd, *Biomechanics of Eye Injury in the Military.* Cham: Springer International Publishing, 2016, pp. 235–262.

[95] X. Liu *et al.*, "Prediction of globe rupture caused by primary blast: a finite element analysis," *Comput. Methods Biomech. Biomed. Engin.*, vol. 18, no. 9, pp. 1024–1029, 2015.

[96] E. Kennedy and S. Duma, "The effects of the extraocular muscles on eye impact force, deflection, and globe rupture response," *J. of Biomech.*, vol. 41, no. 16, pp. 3297–3302, 2008.

[97] E. D. Power, "A nonlinear finite element model of the human eye to investigate ocular injuries from night vision goggles," M.S. thesis, Mech. Eng., Virginia Polytech. Inst., Blacksburg, VA, 2001.

[98] E. Uchio, S. Ohno, J. Kudoh, K. Aoki, and L. T. Kisielewicz, "Simulation model of an eyeball based on finite element analysis on a supercomputer," *Br. J. Ophthalmol.*, vol. 83, no. 10, pp. 1106–11, 1999.

[99] W. Gray *et al.*, "Numerical modeling of paintball impact ocular trauma: identification of progressive injury mechanisms," *Invest. Ophthalmol. Vis. Sci.*, vol. 52, no. 10, pp. 7506–13, 2011.

[100] J. D. Stitzel, S. M. Duma, J. M. Cormier, and I. P. Herring, "A nonlinear finite element model of the eye with experimental validation for the prediction of globe rupture," *Stapp Car Crash J.*, vol. 46, pp. 81–102, 2002.

[101] V. E. Koliatsos *et al.*, "A mouse model of blast injury to brain: initial pathological, neuropathological, and behavioral characterization," *J. Neuropathol. Exp. Neurol.*, vol. 70, no. 5, pp. 399–416, 2011.

[102] H. C. Wang *et al.*, "Pathophysiology of blast-induced ocular trauma with apoptosis in the retina and optic nerve," *Mil. Med.*, vol. 179, no. 8 Suppl, pp. 34–40, 2014.

[103] A. Jean *et al.*, "An animal-to-human scaling law for blast-induced traumatic brain injury risk assessment," *Proc. Nat. Acad. Sci.*, vol. 111, no. 43, pp. 15 310–15 315, 2014.